Carnegie Mellon University

STRUCTURE AND INTERACTIONS OF FLUID PHOSPHOLIPID BILAYERS MEASURED BY HIGH RESOLUTION X-RAY SCATTERING

A Dissertation
submitted to the Graduate School
and Department of Physics
in partial fulfillment of the requirements
for the degree of
Doctor of Philosophy
in
Physics

by

Horia I. Petrache

Prof. John F. Nagle, *Advisor*
Pittsburgh, Pennsylvania, USA.
August 24, 1998

Abstract

The topic of this work is the biologically relevant fluid phase of phosphatidylcholine lipid bilayers. A first goal is the determination of the average bilayer structure using low-angle X-ray scattering from multilamellar lipid vesicles (MLVs). The MLVs are smectic liquid crystals, for which interbilayer correlations decay algebraically. Consequently, the smectic Bragg peaks have power low tails, with the exponent related to the bilayer fluctuations. The analysis of such peaks requires good instrumental resolution and a sophisticated (and equally good) scattering theory. The high resolution is achieved at the F3 station at CHESS. The scattering theory is an improved version of the modified Caillé theory being developed in our laboratory. Data fitting gives the three pieces of information carried by the scattering peaks: position, amplitude, and power-law exponent. The position and the amplitude (form factor) are used to determine the bilayer structure. The power-law exponent is converted into mean square fluctuations in the interbilayer water spacing. This opens a new window on interbilayer interactions which is the second goal of this work. The fundamental issue of interbilayer interactions is addressed both experimentally and theoretically. We obtain the interbilayer water spacing fluctuation σ, as well as the traditional osmotic pressure P, both as functions of the lamellar repeat spacing D and the aqueous separation a. We show theoretically how to obtain the functional form of the fluctuational free energy from the σ data, which is then determined to within a factor that depends upon the bending modulus, K_c. The resulting functional form determined from experimental data has an exponential decay rather than the power law decay that applies for hard confinement in the large a regime, thereby showing that a theory of soft confinement is necessary. The existing theory of soft confinement predicts an exponential decay, but with a smaller decay length λ_{fl} than we obtain. We then use these results to analyze the osmotic pressure data in terms of the bending modulus K_c and the interbilayer interactions consisting of van der Waals and hydration interactions.

Acknowledgments

I would like to thank my advisor Prof. John F. Nagle for giving me the opportunity to work in the field of biological physics and for guiding my research.

I thank Dr. Stephanie Tristram-Nagle for introducing me to the experimental methods including sample preparation, calorimetry, and X-ray scattering.

I thank Prof. Robert M. Suter for guidance and help with the X-ray experiments.

I am grateful to Prof. Antonino Zichichi and to all my teachers who contributed to my education along the many school years.

Thanks to Ruitian Zhang, Wenjun Sun, Scott Feller, and Kechuan Tu for their contribution to our common projects.

Many thanks to my fellow students Shubho Banerjee, Phillip Koran, Chi-Sheng Niu, Anil Prabhakar, and Prem Sivaramakrishnan for all the useful and useless discussions we had.

Thanks to all my Pittsburgh friends for the fun we had together.

Thanks to my family for patience and support.

Glossary

A	area per lipid molecule
a_o	interbilayer water spacing at full hydration
a_o^*	interbilayer water spacing at zero bare pressure
B	compression parameter [erg/cm^4]
D	lamellar spacing
D_o	lamellar spacing at full hydration
D_{HH}	head-head distance across the lipid bilayer
D_B	bilayer thickness (volumetric definition)
D_W	water thickness (volumetric definition)
D'_B	bilayer thickness (steric definition)
D'_W	water spacing (steric definition)
D_C	hydrocarbon thickness (one chain)
D_H	headgroup thickness
D_{H1}	$D_{HH}/2 - D_C$
DPPC	1,2-dipalmitoyl-*sn*-glycero-3-phosphatidylcholine
DMPC	1,2-dimyristoyl-*sn*-glycero-3-phosphatidylcholine
DOPC	1,2-dioleoyl-*sn*-glycero-3-phosphatidylcholine
EPC	egg phosphatidylcholine
F	free energy
F_h	form factor for peak h
$F(q)$	continuous form factor
$G_h(k)$	scattering correlation functions
H	Hamaker parameter
$H(z)$	finite size factor
$H_C(z)$	classical finite size factor
$H_{eff}(z)$	effective finite size factor
$h_{\vec{Q}}$	energy per thermal mode

$\mathcal{H}_d$	discrete Hamiltonian
$\mathcal{H}_c$	continuum Hamiltonian
$I_h(q)$	scattering intensity for peak h
K_A	membrane area compressibility [dyn/cm]
K_c	bending modulus [erg]
L, L_z	scattering domain size along the bilayer normal
L_E	average scattering domain size
L_α	fluid phase
$L_{\beta'}$	gel phase
MCT	modified Caillé theory
N	number of bilayers in a scattering domain
n_W	number of waters per lipid
n'_W	number of waters mixed with the lipid headgroup
n^*_H	number of electrons per headgroup
n^*_L	number of electrons per lipid molecule
$P(D)$	osmotic pressure [dyn/cm^2]
P_h	hydration parameter [dyn/cm^2]
PBC	periodic boundary conditions
PVP	polyvinylpyrrolidone
$\vec{Q}$	thermal mode
q	scattering vector
q_h	scattering peak position
$S_h(q, L)$	scattering factor for peak h from domain L
T	temperature
$U_{\vec{Q}}$	Fourier component of membrane displacement field
$u_n(x, z)$	membrane displacement field
V_H	headgroup volume
V_L	lipid molecular volume
v_L	lipid specific volume [ml/g]
$V(D_W)$, V_{bare}	interaction between non-fluctuating membranes
Z	partition function

$\Delta(k)$	pair correlation function between bilayers n and $n+k$
η_1	Caillé parameter
λ	decay length of the hydration force
$\rho^*(z)$	bilayer electron density profile
ρ^*_W	water electron density level
σ	root mean square fluctuation in the water spacing

Contents

List of tables

List of figures

Chapter 1

Introduction

1.1 Biomembranes

The molecular system studied in this work, namely the lipid bilayer, forms the fundamental structure of biomembranes (Voet and Voet, 1990). Life, as we know it, started with the capacity of organic materials to self-aggregate and self-replicate. One key element is the aqueous property of repelling oily (hydrophobic) materials and attracting polar (hydrophilic) groups. The appearance of molecules with both hydrophobic and hydrophilic parts (amphiphiles), like the lipids, generated instabilities in the "primordial soup". The interaction energy between water and the amphiphiles is minimized when the hydrophobic parts are not directly exposed to water as in Fig. 1.1. As a consequence, the homogeneity of the primordial soup becomes disrupted by the "special zones" created inside the molecular walls.

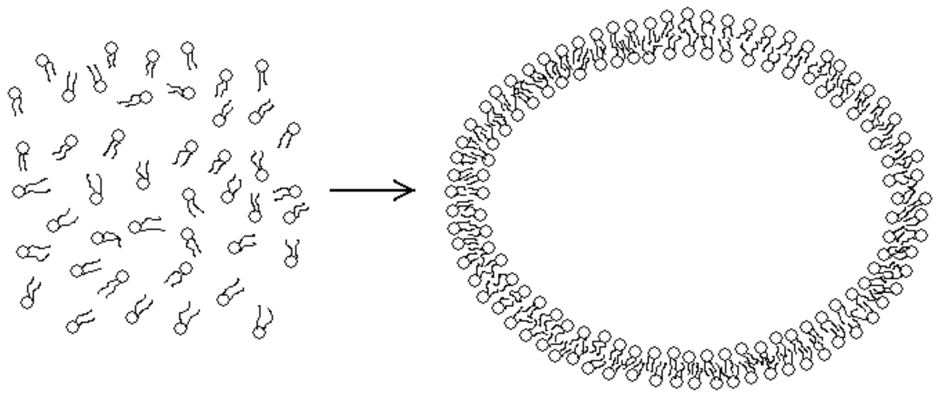

Figure 1.1: Lipid aggregation due to the hydrophobicity of the hydrocarbon chains.

Understanding biomembranes requires the joint effort of researchers form many scientific fields including biology, chemistry and physics. Biomembranes are complex macromolecular systems that provide the interface between the biological cell interior and the surrounding environment and basically consist of a lipid matrix with protein inclusions. The proteins are big molecular aggregates with specific functions in cellular processes. The lipid matrix provides the support and assists the proteins in performing their functions. The functions of molecular aggregates are related to their structure; it is the structure-function relation that is the object of modern molecular biology. For the biological physicist the corresponding relation is the one between the structure and the interaction of macromolecular systems. The predictive power of physics formalisms, once interactions are determined, can be put to work in designing efficient biomaterials.

1.2 Lipid bilayers

A lipid membrane, stripped of protein insertions, is a challenging system for a physical description based on first principles. A single lipid molecule consists of more than 100 atoms (see Fig. 1.2) and there are many thermally accessible degrees of freedom for the whole membrane system. Evidently, and fortunately, only a reduced number of degrees of freedom are relevant for a particular aspect of the lipid membrane. An example is the mathematical description presented in Chapter 2 of this work.

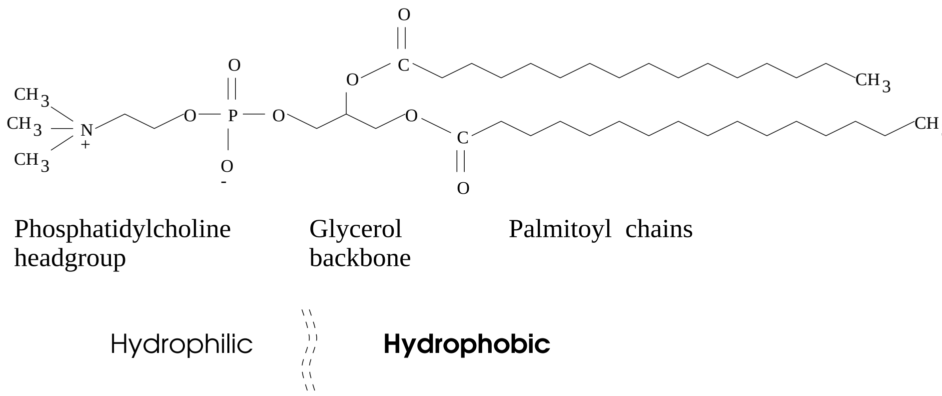

Figure 1.2: A DPPC molecule: $C_{40}H_{80}O_8PN$, molecular weight = 734 g/mole. The lines with no symbols represent $(CH_2)_n$ chains.

Lipid bilayers exhibit a number of thermal phases characterized by the molecular packing in the bilayer plane (Small, 1986). As expected, lower temperature phases are more ordered. For example, below T=41.4^{o}C, the benchmark lipid, DPPC (1,2-dipalmitoyl-*sn*-glycero-3-phosphatidylcholine), is arranged in an hexagonal lattice, with the chains in all-*trans* conformations. At T=41.4^{o}C the chains melt: a significant number of C-C bonds become *gauche*. Because isolated single *trans*-*gauche* transitions are prevented by steric interactions between chains (Nagle, 1973) this melting is a cooperative process. As a result of melting, the order in the bilayer plane is lost, therefore the high temperature phase is called the fluid phase. With the order being lost, the determination of fluid phase properties becomes a challenge.

1.3 Goals

Chain ordered phases have been long studied owing to the well defined wide angle scattering patterns. The most recent analysis performed in our laboratory is presented in Tristram-Nagle et al. (1993), Sun et al. (1994), Sun et al. (1996). Also in our laboratory, a method to determine the fluid phase structure has been developed and applied to DPPC bilayers (Nagle et al., 1996). In the present work, we will first use similar methods to determine the fluid phase structure of three more lipids: DMPC (1,2-dimyristoyl-*sn*-glycero-3-phosphatidylcholine), EPC (egg phosphatidylcholine) and DOPC (1,2-dioleoyl-*sn*-glycero-3-phosphatidylcholine) and second, we will develop a method to determine the interbilayer interaction parameters, once the structural parameters are known.

1.3.1 Structure

Before we proceed, let us first clarify the meaning of "structure determination". Lipid vesicles composed of single bilayers, such as the one shown in Fig. 1.1 are called unilamellar vesicles (UV). More often, though, lipid bilayers aggregate into multilamellar vesicles (MLV) which are more suitable for X-ray studies due to stronger scattering. Consider the sketch of two neighboring bilayers depicted in Fig.1.3. The first obvious structural parameter is the lattice spacing D. Because of the many fluctuations in the systems, we will always refer to average quantities; they are directly obtained from scattering experiments. More relevant than the D spacing itself is the partition into a bilayer thickness D_B and a water thickness D_W. Figure 1.3 shows two different partitions such that

$$D_B + D_W = D = D'_B + D'_W. \tag{1.1}$$

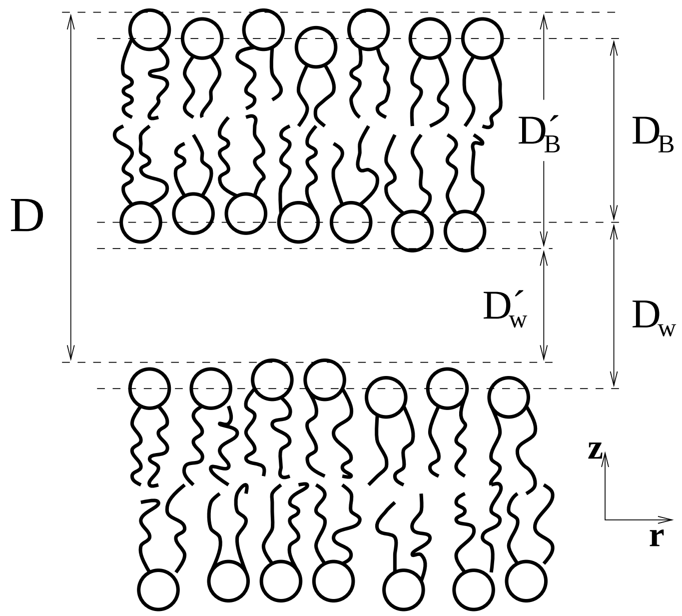

Figure 1.3: Sketch of two neighboring bilayers

The bilayer thickness includes contributions from both hydrophobic and hydrophilic parts and so, the next refinement level is to partition the bilayer into a hydrocarbon thickness D_C and a headgroup thickness D_H. The most convenient quantity to consider is the average area per lipid A at the liquid interface from which the various thicknesses can be obtained (Nagle and Wiener, 1988).

Determination of the area per lipid A has been a challenge. For example, for DPPC, one of the most studied lipids, literature uncertainties in the fluid phase (F) area A^F_{DPPC} range from 56 to 73Å^2 (Nagle, 1993). This range is enormous, especially when one considers that the DPPC gel G (*i.e.* $L_{\beta'}$) phase has $A^G_{DPPC} = 47.9$Å^2 (Sun et al., 1994); therefore, the effect of fluidization, namely, $A^F - A^G$, has an uncertainty over 100% ! Such uncertainties are unacceptable when trying to set up simulations at fixed area (Feller et al., 1997; Perera et al., 1997) or when trying to evaluate the results of simulations in constant pressure ensembles (Tobias et al., 1997; Tieleman et al., 1997).

1.3.2 Fluctuations and interactions

For lipid membranes, as for biological systems in general, the average structure is only part of the description. One also needs information about the fluctuations about this average. This is especially true for bilayers because fluctuations play an important role in the effective interactions that govern the system's behavior.

In practice, interactions are determined by measuring the response of a system to exterior stress. For example, one measures the elongation of a spring as a function of the external pulling force in order to determine the spring constant. For the bilayer stack one can vary the interbilayer water spacing D_W by applying an external osmotic pressure P. The traditional method, introduced by Rand, Parsegian and co-workers (Parsegian et al., 1979; Rand and Parsegian, 1989) uses water soluble polymers that, while not mixing within the lipid bilayers, compete with them for the available water. By integrating the curve $P(D_W)$ one obtains the effective interbilayer interaction,

$$V_{eff}(D_W) = -\int_0^{D_W} P(a)\, da. \tag{1.2}$$

However, as Helfrich (1978) showed, this effective interaction also includes the contribution from thermal fluctuations (undulations) of the bilayer,

$$V_{eff} \equiv F = V_{bare} + F_{fl} = V_{bare} - TS^u, \tag{1.3}$$

where T is the absolute temperature, S^u is the entropy associated with the bilayer fluctuations, and V_{bare} denotes the interaction between non-fluctuating flat membranes. F_{fl} is the contribution of fluctuations to the total free energy F.

In the fluid phase, fluctuations are a significant part of the interbilayer interactions (McIntosh and Simon, 1993) and therefore V_{bare} is not directly measurable. In this work we show how the partitioning into V_{bare} and F_{fl} can be obtained if the traditional osmotic pressure $P(D_W)$ data are supplemented with a measurement of interbilayer mean square fluctuations $\sigma^2(D_W)$.

Chapter 2

Liquid Crystal Description

2.1 Introduction

Ensembles of elongated molecules often exhibit anisotropic properties. In particular, a stack of lipid membranes in the fluid phase can be described as a one-dimensional array of two-dimensional fluids, as sketched in Fig. 2.1.

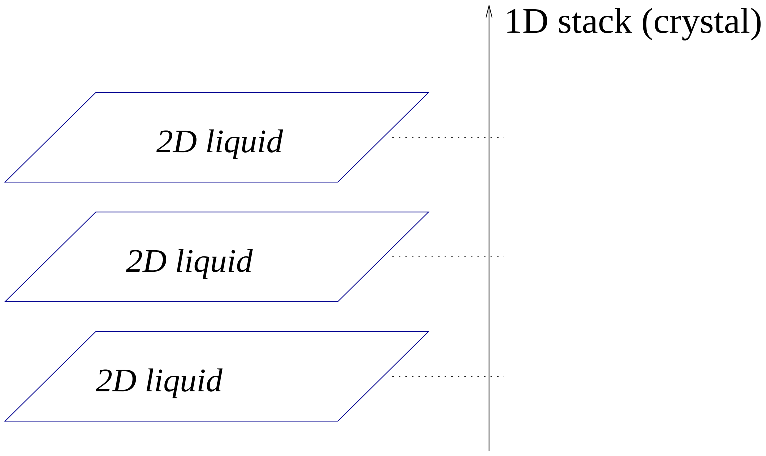

Figure 2.1: Smectic liquid crystal

It is well known (de Gennes, 1974) that dimensionality is crucial in the study of order/disorder of a system. The order/disorder properties of a system are described by the correlations between the system's building blocks. In particular, crystalline structures are described by positional correlation functions. In a true crystal, these correlations are long range and permit the observation of well defined scattering patterns. In fluids, the correlations are short range and most of the scattering is diffuse. A typical X-ray pattern of a membrane stack in the fluid phase is diffuse at wide scattering angles, indicating short intermolecular (*intra*bilayer) correlations, but still exhibits well defined periodic scattering peaks at low angles, corresponding to longer *inter*bilayer correlations. However, in smectic systems there is no true long range order as in a crystal, but, as has been extensively shown, smectic systems have quasi-long range correlations along the layer normal. As a consequence, the scattering peaks have long power law tails (Caillé, 1972; Als-Nielsen et al., 1980; Safinya et al., 1989; Roux and Safinya, 1988; Wack and Webb, 1989; Zhang et al., 1994). The minimal description that accounts for this feature of the membrane stack is presented in Fig. 2.2.

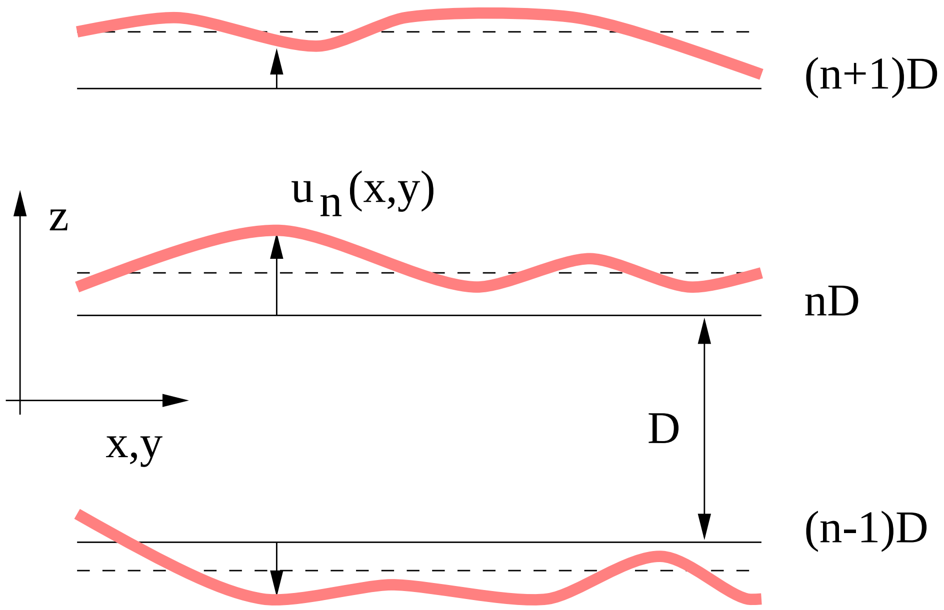

Figure 2.2: de Gennes - Caillé model of a stack of fluctuating membranes. The bilayer thickness D_B is set to zero, therefore the repeat spacing D and the water spacing D_W are equivalent.

In this model each membrane n is considered as a mathematical 2D surface (internal structure is ignored; $D_B = 0$) whose points are represented by a displacement field $u_n(x,y)$ relative to the lattice points $z_n = nD$. The set of variables $u_n(x,y)$ represent the system fluctuations about the equilibrium position. The energetics are described by the following effective Hamiltonian,

$$\mathcal{H} = \frac{1}{NL^2}\int dx \int dy \sum_{n=0}^{N-1}\left[\frac{1}{2}K_c\left(\frac{\partial^2 u_n}{\partial x^2}+\frac{\partial^2 u_n}{\partial y^2}\right)^2 + \frac{1}{2}B(u_{n+1}-u_n)^2\right] + V(D_W). \quad (2.1)$$

The first term accounts for the bending energy due to the membrane curvature. For a flat membrane, $u_n(x, y)$ is a constant and the bending energy is zero. The bending modulus K_c is assumed to be independent of the osmotic pressure, but it may depend on temperature. The second term accounts for the fluctuational part of the interbilayer interactions. The relative displacement $u_{n+1} - u_n$ measures the change in the nearest neighbor distance from its average value. The phenomenological parameter B is a function of the inter-membrane spacing D_W, or equivalently, it is a function of the osmotic pressure. The last term in the Hamiltonian is independent of the fluctuation variables $u_n(x, y)$ and gives the interaction energy between rigid membranes as a function of the inter-membrane separation. Relative to this Hamiltonian, the interactions are completely described if the constant K_c and the two functions $B(D_W)$ and $V(D_W)$ are specified. None of these phenomenological quantities can be entirely determined theoretically from first principles due to the internal complexity of the membrane system.

For complex systems it is customary to employ "effective" theories (in which the system is described at a satisfactory level) with a number of phenomenological parameters to be determined experimentally. The description used in this work differs in two aspects from the original de Gennes - Caillé theory, in which the focus was mainly on the fluctuational properties. These are best seen by comparing our expression in Eq. 2.1 with the de Gennes Hamiltonian,

$$\mathcal{H}_c = \int dx \int dy \int dz \left[\frac{1}{2} K \left(\frac{\partial^2 u}{\partial x^2} + \frac{\partial^2 u}{\partial y^2} \right)^2 + \frac{1}{2} B_3 \left(\frac{\partial u}{\partial z} \right)^2 \right], \tag{2.2}$$

with $K = K_c/D$ and $B_3 = BD$. First, the de Gennes model represents the membrane stack as a continuum in all three spatial directions. Second, the bare interaction term $V(D_W)$ is ignored because, originally, the main focus was on fluctuational part only. In the present work we are concerned with interbilayer interactions for which Eq. 2.1 is a more appropriate model. The effective Hamiltonian introduced in Eq. 2.2 has been shown to describe well the lamellar scattering from smectic systems, i.e. it captures the behavior of the inter-lamellar correlation function (Caillé, 1972; Zhang et al., 1994). Because the scattering peak shape is determined by the large scale behavior of the lamellar system, the discrete (Eq. 2.1) and the continuum (Eq. 2.2) descriptions are equivalent in the limit of large N (i.e. $L \gg D$), as shown in Appendix A. Therefore, the Modified Caillé Theory (MCT) developed by Zhang et al. (1994)

starting from the Hamiltonian in Eq. 2.2 can be easily adapted to Eq. 2.1, as described in Chapter 3.

2.2 Review of interaction studies

The bending constant K_c is traditionally measured on unilamellar vesicles for which interbilayer interactions are not present. Typical values for neutral lipids range between $0.5 - 2.0 \cdot 10^{-12}$ ergs (Faucon et al., 1989; Evans and Rawicz, 1990; Kummov and Helfrich, 1991; Meleard et al., 1997).

The bare interaction $V(D_W)$ is directly measurable from the osmotic pressure curves if fluctuations are small, as for example in the gel phase. This kind of experiment (Rand and Parsegian, 1991; McIntosh and Simon, 1993), together with theoretical calculations of van der Waals interactions (Parsegian and Ninham, 1971; Rand and Parsegian, 1989) suggest that the bare interaction is a sum of at least two terms of the form

$$V_{\text{attraction}} = -\frac{H}{12\pi}\left[\frac{1}{D_W^2} - \frac{2}{(D_W+D_B)^2} + \frac{1}{(D_W+2D_B)^2}\right] \tag{2.3}$$

$$V_{\text{repulsion}} = P_h\lambda\, e^{-D_W/\lambda}. \tag{2.4}$$

The attractive term is the van der Waals interaction between two plates of thickness D_B separated by distance D_W. The interaction strength is measured by the Hamaker parameter H, estimated to lie in the range $10^{-14} - 10^{-13}$ erg (Rand and Parsegian, 1989; McIntosh and Simon, 1993; Parsegian, 1993). The origin of the repulsive term is not yet completely understood. Different theories have been proposed (Marcelja and Radic, 1976; Israelachvili and Wennerstrom, 1990) but it remains an outstanding topic of fundamental interest and much uncertainty (Parsegian and Rand, 1991). In this work we will accept the working hypothesis that there is a separable hydration interaction with an exponential decay. From osmotic pressure measurements (for the L_α phase) λ has been estimated to be in the range $1.4 - 2.4$Å (McIntosh and Simon, 1986; McIntosh and Simon, 1993; Rand and Parsegian, 1989). We note that McIntosh and Simon tend to get the smaller values ($1.4 - 1.7$Å) while Rand and Parsegian the larger ones ($2.0 - 2.4$Å). The numerical value of P_h is tightly coupled to whether one chooses the water spacing to be D_W or D'_W in Fig. 1.3. Using the D'_W convention yields $P_h = 5 \cdot 10^8$ erg/cm^3 (McIntosh et al., 1987) and using the D_W convention just rescales P_h by $\exp[(D_W - D'_W)/\lambda]$; this is clearly not an essential difference. In this work we will use the D'_W convention in the interaction analysis.

The compression modulus $B(D_W)$ is a very complex quantity. It accounts for everything that is not contained in the bare interaction term. Theoretical attempts try to relate $B(D_W)$ to $V(D_W)$ but this is not an easy task. Helfrich (1978) analyzed the case when there are no van der Waals or hydration interactions, only the steric interactions caused by collision of bilayers. In this case, which will be called hard confinement, Helfrich showed that there is another important repulsive force when the bilayers are flexible. This force is due to the increased free energy from the decrease in entropy that accompanies the reduction of out-of-plane fluctuations; such reduction is required when the water spacing is reduced. Helfrich treated the steric interactions by using an effective compression parameter B, as in Eq. 2.2 and found that the steric free energy per unit area has the form

$$f_U = 0.42 \, \frac{(k_B T)^2}{K_c D_W^2}. \tag{2.5}$$

When a repulsive hydration force is present, the confinement of each membrane is softer than for purely steric interactions because there are very few membrane collisions. In this case, called soft confinement, it has been proposed (Sornette and Ostrowsky, 1986) that the fluctuation free energy in Eq. 2.5 should be modified and a formula involving an exponential with decay length 2λ,

$$f_{U2} = \frac{\pi}{2} \frac{k_B T}{8} \sqrt{\frac{P_h/\lambda}{K_c}} \, e^{-D_W/2\lambda}, \tag{2.6}$$

has been offered (Evans and Needham, 1987). In a more recent theory (Podgornik and Parsegian, 1992) Eq. 2.6 again appears. However, the theory was then extended to include van der Waals interactions and it is not clear if Eq. 2.6 remains valid. Derivations of fluctuation free energies, in both hard and soft confinement theories, need various assumptions about the compression parameter B. One achievement of the present paper is to employ experimental data to determine the functional form for this interaction in the soft confinement case.

It has also been shown on the basis of $P(D)$ data (McIntosh et al., 1987) that there is an additional repulsive interaction at small distances that was described as the beginning of a steric interaction between head groups and an extra exponential has been used to fit the $P(D)$ data (McIntosh and Simon, 1993) for large P and water spacing smaller than 4Å. Our data do not go to such small water spacings or such high pressures, so this additional force will not be considered further in this work.

The following sections will show how $B(D_W)$ can be measured experimentally and then how this result is used in order to determine the other interaction parameters.

2.3 Derivation of the free energy

Interpretation of osmotic pressure data requires the calculation of the free energy $F = E - TS$, since the entropy S plays a major role. In general, for biophysical systems the interactions are better described in terms of effective entropic forces rather than conventional physics forces. Derivations of properties of smectic theories have been performed before, but we present it again here with special care for the numerical factors that are essential for detailed analysis of data. As usual, consider the Fourier representation of the displacement variables,

$$u_n(x,y) \;=\; \sum_{Q_x,Q_y,Q_z} U(Q_x,Q_y,Q_z)e^{i\vec{Q}\cdot\vec{R}} \tag{2.7}$$

with $\vec{R} = \vec{r} + nD\hat{z}$ and the vectors $\vec{Q}$ taking values in the first Brillouin zone defined by the in-plane molecular size for Q_x, Q_y and by the membrane spacing D for Q_z. In terms of independent variables, the fluctuation part of $\mathcal{H}$ from Eq. 2.1 is written as

$$\mathcal{H}_{fl} = \sum_{\vec{Q}} \frac{1}{2} h_{\vec{Q}}\ |U_{\vec{Q}}|^2 = \sum_{\vec{Q},Q_z>0} h_{\vec{Q}}\ |U_{\vec{Q}}|^2, \tag{2.8}$$

where

$$h_{\vec{Q}} = NL^2(K_c Q_r^4 + 4B\sin^2(Q_z D/2)). \tag{2.9}$$

From the equipartition theorem, the mode amplitude is

$$\langle |U_{\vec{Q}}|^2 \rangle = k_B T / h_{\vec{Q}}. \tag{2.10}$$

The partition function is given by

$$Z = \prod_{\vec{Q},\ Q_z>0} \int C\ d(ReU_{\vec{Q}})\ d(ImU_{\vec{Q}})\ e^{-\beta H}, \tag{2.11}$$

where the constant C has the role of making Z dimensionless by compensating for a unit of $(length)^{-2}$ for each mode $\vec{Q}$. The integration yields

$$\begin{aligned} Z &= \prod_{\vec{Q},Q_z>0} C \int_{-\infty}^{\infty} d(ReU_{\vec{Q}})\ e^{-\beta h_{\vec{Q}}(ReU_{\vec{Q}})^2} \int_{-\infty}^{\infty} d(ImU_{\vec{Q}})\ e^{-\beta h_{\vec{Q}}(ImU_{\vec{Q}})^2} \\ &= \prod_{\vec{Q},Q_z>0} C \frac{\pi}{\beta h_{\vec{Q}}}. \end{aligned} \tag{2.12}$$

Then, the free energy is

$$F_{fl} = -\frac{1}{\beta} \ln Z = \frac{k_B T}{2} \sum_{all\vec{Q}} \ln\left(\frac{\beta h_{\vec{Q}}}{C\pi}\right) = \sum_{allQ_z} F(Q_z), \tag{2.13}$$

where $F(Q_z)$ stands for the free energy per compression mode. We will consider for the energy reference the state with $B = 0$ and calculate

$$\Delta F = F(B \neq 0) - F(B = 0). \tag{2.14}$$

For each compression mode we have,

$$\begin{aligned} \Delta F(Q_z) &= \frac{k_B T}{2} \frac{L^2}{4\pi^2} \int_{\vec{Q}_r} d^2 Q_r\ \ln\left(\frac{K_c Q_r^4 + 4B\ \sin^2(Q_z D/2)}{K_c Q_r^4}\right) \\ &= \frac{k_B T}{2} \frac{L^2}{4\pi^2}\ \pi \int_{Q_{rmin}}^{Q_{rmax}} d(Q_r^2)\ \ln\left(1 + \frac{4B\ \sin^2(Q_z D/2)}{K_c Q_r^4}\right) \\ &= L^2\ \frac{k_B T}{2} \sqrt{\frac{B}{K_c}}\ |\sin(Q_z D/2)|. \end{aligned} \tag{2.15}$$

Summing over all compression modes (Eq. 2.13), the free energy per unit area is:

$$\begin{aligned} \frac{\Delta F_{fl}}{L^2} &= \sum_{allQ_z} \frac{\Delta F(Q_z)}{L^2} = \frac{k_B T}{4} \sqrt{\frac{B}{K_c}} \sum_{allQ_z} \left|\sin \frac{Q_z D}{2}\right| \\ &= \frac{k_B T}{4} \sqrt{\frac{B}{K_c}}\ \frac{2N}{\pi} \int_0^{\pi/2} \sin(x) dx = N \frac{k_B T}{2\pi} \sqrt{\frac{B}{K_c}}. \end{aligned} \tag{2.16}$$

The fluctuation free energy per unit area of one bilayer is

$$\frac{\Delta F_{fl}}{N\ L^2} = \frac{k_B T}{2\pi} \sqrt{\frac{B}{K_c}} \tag{2.17}$$

and the total free energy is

$$\frac{\Delta F}{N\ L^2} = V(D_W) + \frac{k_B T}{2\pi} \sqrt{\frac{B}{K_c}}. \tag{2.18}$$

ΔF represents the free energy change when free fluctuating membranes are brought together at separation D_W characterized by a compression modulus $B(D_W)$.

2.4 Derivation of the mean square fluctuations

The degree of order in the lamellar system is characterized by the mean square fluctuation function,

$$\Delta^2(k) \quad = \quad \langle [u_n(x,y) - u_{n+k}(x,y)]^2 \rangle, \tag{2.19}$$

which is calculated as follows.

$$\begin{aligned}
\Delta^2(k) &= \langle [u_0(x,y) - u_k(x,y)]^2 \rangle = \\
&= \langle \left[\sum_{\vec{Q}} U(\vec{Q}) \left(e^{i(Q_x x + Q_x y)} - e^{i(Q_x x + Q_x y + Q_z k D)} \right) \right]^2 \rangle = \\
&= \langle \left[\sum_{\vec{Q}} U(\vec{Q}) e^{i\vec{Q}\cdot\vec{r}} \left(1 - e^{iQ_z k D} \right) \right]^2 \rangle = \\
&= \sum_{\vec{Q}} \sum_{\vec{Q}'} \langle U(\vec{Q}) U(\vec{Q}') \rangle \ e^{i(\vec{Q}+\vec{Q}')\cdot\vec{r}} \left(1 - e^{iQ_z k D} \right) \left(1 - e^{iQ'_z k D} \right) = \\
&= \sum_{\vec{Q}} \langle |U(\vec{Q})| \rangle \ \left(1 - e^{iQ_z k D} \right) \left(1 - e^{-iQ_z k D} \right) = \\
&= k_B T \sum_{Q_z} \sum_{\vec{Q}_r} \frac{4 \sin^2 \left(\frac{Q_z k D}{2} \right)}{N L^2 (K_c Q_r^4 + 4B \ \sin^2 \left(\frac{Q_z D}{2} \right))},
\end{aligned} \tag{2.20}$$

using Eq. 2.10. With the integration limits $Q_{rmin} = 0$ and $Q_{rmax} = \infty$ (see Appendix B for the actual limits), we get:

$$\Delta^2(k) = \frac{k_B T}{8N} \sum_{Q_z} \frac{4 \sin^2 \left(\frac{Q_z k D}{2} \right)}{\sqrt{K_c B \ 4 \sin^2 \left(\frac{Q_z D}{2} \right)}} = \frac{k_B T}{4} \frac{1}{\sqrt{K_c B}} \frac{1}{N} \sum_{Q_z} \frac{\sin^2 \left(\frac{Q_z k D}{2} \right)}{\left| \sin \left(\frac{Q_z D}{2} \right) \right|}. \tag{2.21}$$

As in the free energy calculation (Eq. 2.16) we are left with a summation over the compression modes. The integrand is an increasing function of Q_z and the largest contribution is given by the higher modes. With $Q_z = 2\pi j / L$ we write $\Delta^2(k)$ as

$$\begin{aligned}
\Delta^2(k) &= \frac{k_B T}{4\pi} \frac{1}{\sqrt{K_c B}} \sum_{j=1}^{N/2} \frac{1 - \cos \frac{2\pi j k}{N}}{\frac{N}{\pi} \sin \frac{\pi j}{N}} \\
&= \frac{k_B T}{4\pi} \frac{1}{\sqrt{K_c B}} \ \Sigma(N,k).
\end{aligned} \tag{2.22}$$

We have introduced the notation $\Sigma(N,k)$ for the summation over the bilayer index j because it is convenient to refer to $\Sigma(N,k)$ in discussing the variation of $\Delta^2(k)$ with k. Due to periodic boundary conditions (PBC) the function $\Delta^2(k)$ is symmetric about $k = N/2$ as shown in Fig. 2.3. The behavior of $\Delta^2(k)$ for $k > N/2$ is an artifact of PBC and is unusable in describing the real system. In order to minimize the PBC effect we consider the asymptotic limit $N \to \infty$.

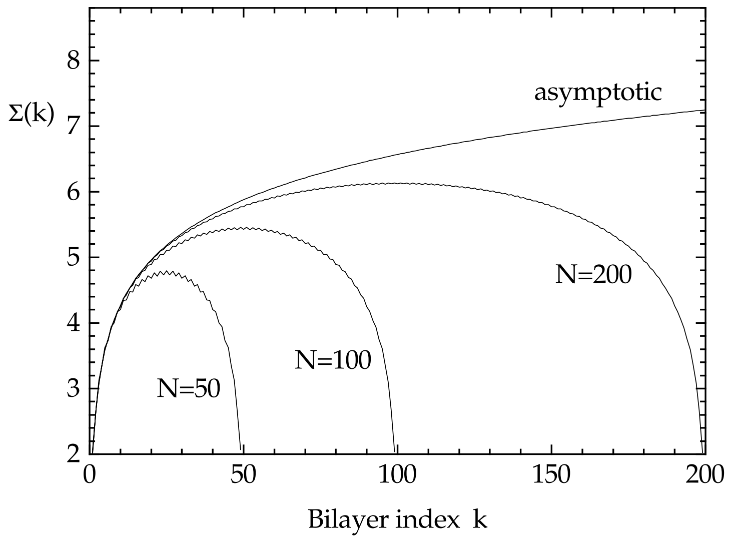

Figure 2.3: Effect of PBC on the correlation function: $\Sigma(k)$ is symmetric about $k = N/2$. The wiggling of the curves, especially at small N, is due to the oscillating functions in Eq. 2.22.

Fig. 2.3 shows the calculation of $\Sigma(N,k)$ for $N = 50$, 100 and 200 together with the asymptotic form corresponding to $N = \infty$. For $k < N/3$ the finite size $\Delta^2(k)$ is practically indistinguishable from the asymptotic form.

For $k = 1$, Eq. 2.22 gives the mean square fluctuation in the distance between two neighboring bilayers,

$$\sigma^2 \equiv \Delta^2(1) = \frac{k_B T}{2\pi} \frac{1}{\sqrt{K_c B}}. \tag{2.23}$$

If σ^2 is measured experimentally then one obtains the compression parameter from Eq. 2.23,

$$B = \left(\frac{k_B T}{2\pi}\right)^2 \frac{1}{K_c \sigma^4} \tag{2.24}$$

and the fluctuation free energy from Eq. 2.17,

$$F_{fl} = \left(\frac{k_B T}{2\pi}\right)^2 \frac{1}{K_c \sigma^2}. \tag{2.25}$$

The total free energy is then

$$F = V(D_W) + \left(\frac{k_B T}{2\pi}\right)^2 \frac{1}{K_c \sigma^2}. \tag{2.26}$$

The results given in Eqs. 2.24 and 2.25 should be used with caution; they are not generally applicable. As explained in Appendix B the summations over undulation modes have been done for the case

$$4B \sin^2(Q_z D/2) \gg K_c Q_{rmin}, \tag{2.27}$$

which holds for the lamellar systems considered in this work. The condition given in Eq. 2.27 can be easily violated for other systems, for example if the membranes are very stiff (large K_c). In this case one should evaluate the summations using appropriate prescriptions. Additional conditions have been imposed on the integration limits. In terms of the persistence length $\lambda \equiv \sqrt{K_c/BD^2}$ (de Gennes, 1974), these conditions are

$$\lambda L_z \gg L_x L_y \tag{2.28}$$

$$\lambda D \gg a^2, \tag{2.29}$$

where $a \approx 7$Å represents the intermolecular distance in the membrane plane. Both conditions are satisfied for our lipid samples.

We have used high resolution X-ray diffraction in order to measure the interbilayer spacing fluctuation σ^2 needed in Eqs. 2.24 and 2.25. The scattering theory, adapted to the discrete Hamiltonian (Eq. 2.1), is presented in the next chapter.

Chapter 3

Scattering Theory

3.1 Introduction

The lamellar X-ray scattering pattern consists of equally spaced diffraction peaks situated at scattering vectors $q_h = \frac{2\pi h}{D}$, where the integer h denotes the peak order. The intensity for the h-th order is given by

$$I_h(q) = |F(h)|^2 S_h(q), \tag{3.1}$$

where $F(h)$ and $S_h(q)$ are the form factor and the structure factor respectively. The structure factor $S_h(q)$ is averaged over the fluctuations described in the previous chapter. In the Caillé theory the fluctuations in the form factor and the fluctuations in the structure factor are considered decoupled and the averaging of the two is done independently (Zhang et al., 1994; see also the comment on Lemmich et al., 1996). The scattering peaks from our samples are very narrow (as will be shown in Fig. 4.1) and we perform the analysis of the peak tail close to the central peak, within $\pm .15$ deg in 2θ, vs. ~ 1 deg between peaks. In this small interval there is no significant variation of the form factor and we treat it as a constant.

The form factor is the Fourier transform of the electron density profile of a single bilayer,

$$F(h) = \int_{-D/2}^{D/2} \rho^*(z)\, e^{iq_h z} dz. \tag{3.2}$$

When all $F(h)$ are measured, the bilayer electron density profile $\rho^*(z)$ can be Fourier reconstructed (see Chapter 5). Because of the quasi-long range correlations, the diffracted peak is broadened by the long power law tails of the structure factor $S_h(q)$. As a consequence, the simple integration of the peak intensity is inaccurate due to the uncertainty from regions with low signal to noise ratios (Nagle et al., 1996).

Therefore, a careful analysis of the peak shape is required for an accurate measurement of $F(h)$. This was accomplished qualitatively by Caillé, (1972) and quantitatively by Zhang et al., (1994). The basic ingredient is the scattering correlation function introduced by Caillé as

$$G_h(k) = \langle e^{iq(u_{n+k} - u_n)} \rangle \overset{h.a.}{\approx} e^{-\frac{1}{2}q_h^2 \Delta^2(k)}, \tag{3.3}$$

where $\Delta^2(k)$ is the interbilayer correlation function calculated in Section 2.4 from the previous chapter (see Eq. 2.22). Using Caillé's notation,

$$\eta_1 = \frac{\pi}{2} \frac{k_B T}{D^2} \frac{1}{\sqrt{K_c B}} \tag{3.4}$$

we can rewrite Eq. 2.22 as

$$\Delta^2(k) = \frac{2\eta_1}{q_1^2}\, \Sigma(k), \tag{3.5}$$

and then combine Eq. 3.3 and Eq. 3.5 to write the correlation function in the simplified form,

$$G_h(k) = e^{-\eta_1 \, h^2 \, \Sigma(k)}. \tag{3.6}$$

This form explicitly shows that $G_h(k)$ depends on η_1 and on the bilayer index k only. The Caillé parameter η_1 is related to $\sigma^2 \equiv \Delta(k = 1)$ through the simple expression (see Eq. 2.23 and Eq. 3.4),

$$\eta_1 = \sigma^2 \, \frac{\pi^2}{D^2}. \tag{3.7}$$

We have measured η_1 by fitting to the X-ray data. The fitting program basically uses the Modified Caillé Theory (Zhang et al., 1994) adapted to the discrete Hamiltonian introduced in Eq. 2.1. The next section presents the fitting function with references to the original expressions of the MCT theory (Zhang et al., 1994) given as "MCT.#".

3.2 MCT fitting function

Using a continuum description of the membrane stack (Eq. 2.2), Zhang et al. (1994) calculated the structure factor for a single domain of size $L = ND$ as (see MCT.77)

$$S_h(q, L) = \frac{4\pi L_r^2}{q^2} \int_0^L dz\, G_h(z)\,(L - z)\, \cos[(q - q_h)z]. \tag{3.8}$$

For a distribution of domain sizes $P(L)$, the observed structure factor is the average

$$\langle S_h(q) \rangle_L = \int_0^\infty \, dL\; P(L)\; S_h(q, L). \tag{3.9}$$

The averaging over domain sizes is usually interpreted in terms of an effective finite-size factor $H_{eff}(z)$ which is defined by the following relation (see MCT.15)

$$\langle S_h(q)\rangle_L = \frac{4\pi L_r^2}{q^2}\int_0^\infty dz\; H_{eff}(z)\, G_h(z)\, \cos[(q-q_h)z]. \tag{3.10}$$

H_{eff} is obtained by performing the integral over L in the expression for the average structure factor (see Eq. 3.9 and Eq. 3.8),

$$\begin{aligned}\langle S_h(q)\rangle_L &= \frac{4\pi L_r^2}{q^2}\int_0^\infty dL\, P(L)\int_0^L dz\, G_h(z)\,(L-z)\,\cos[(q-q_h)z] & (3.11)\\ &= \frac{4\pi L_r^2}{q^2}\int_0^\infty dz\left[\int_z^\infty dL\, P(L)\,(L-z)\right] G_h(z)\,\cos[(q-q_h)z]. & (3.12)\end{aligned}$$

By comparing the last result with Eq. 3.10 we identify

$$H_{eff}(z) = \int_z^\infty dL\, P(L)\,(L-z). \tag{3.13}$$

Note that the expression for H_{eff} (Eq. 3.13) is very simple if the correlation function $G_h(z)$ is independent of the domain size L.

The discrete version of Eq. 3.8 is (see Eq.MCT.78)

$$S_h(q,L) = \frac{2\pi L_r^2 D}{q^2}\left[N + 2\sum_{k=1}^{N} G_h(k)\,(N-k)\,\cos[(q-q_h)kD]\right]. \tag{3.14}$$

Our preference for the discrete Hamiltonian comes from the fact that it allows for an easier interpretation of the interaction parameters. Also, the use of the correlation function in the form of Eq. 3.6 significantly increases the efficiency of data fitting because the universal function $\Sigma(k)$ is calculated only once and stored in a database. A description of the fitting routine is given in Appendix C.

Initially (Zhang et al., 1994, 1996), fits to the X-ray data were done using a Gaussian distribution for the scattering domain sizes,

$$P(L) \sim e^{-\frac{(L-L_G)^2}{2\sigma_G^2}}. \tag{3.15}$$

This $P(L)$ distribution is shown by the solid line in Fig. 3.1.

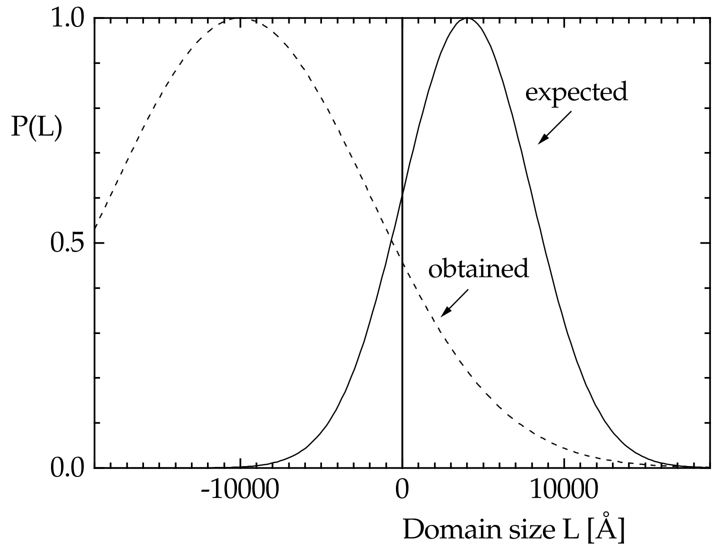

Figure 3.1: Solid line: Gaussian $P(L)$ for $L_G = 4000\text{Å}$ and $\sigma_G = 4000\text{Å}$. Dashed line: Gaussian $P(L)$ for $L_G = -10000\text{Å}$ and $\sigma_G = 8000\text{Å}$. MCT uses the physical region $L > 0$ only.

However, for about 1/3 of the samples the fits gave broad $P(L)$ distributions centered at negative values of L_G, as shown by the dashed line in Fig. 3.1, when MCT was used for the data reported in (Zhang, 1995; Zhang et al., 1996). In that work, L_G was constrained to positive values and the fits resulted in values of L_G close to zero. For the data fit in the present work about 2/3 of the samples have this same anomalous behavior and so it was decided to consider alternative $P(L)$ distributions.

The solid line in Fig. 3.2 shows $P(L)$ from Eq. 3.15 for an example where the fit gave a negative L_G. The magnitude of the error bars on L_G and σ_G (as shown in the third column of Table 3.1) indicate over-parameterization.

The domain size distribution in Fig. 3.2 has no obvious physical interpretation. However, the meaningful quantity is the effective finite-size factor H_{eff}, which we now discuss. We first address the question whether, in the limit of our experimental errors, there is more than one function $P(L)$ that gives the same H_{eff}. We considered a reasonable Gaussian $P(L)$ function centered at $L_1 = 4000\text{Å}$ with width $\sigma_1 = 4000\text{Å}$. The corresponding H_{eff} is presented in Fig. 3.3 with the solid line. Two different Gaussian $P(L)$ functions ($L_2 = 0\text{Å}$, $\sigma_2 = 5500\text{Å}$ and $L_3 = -10000\text{Å}$, $\sigma_3 = 8000\text{Å}$) were found to give quite similar H_{eff} as shown in Fig. 3.3 with dashed and dotted

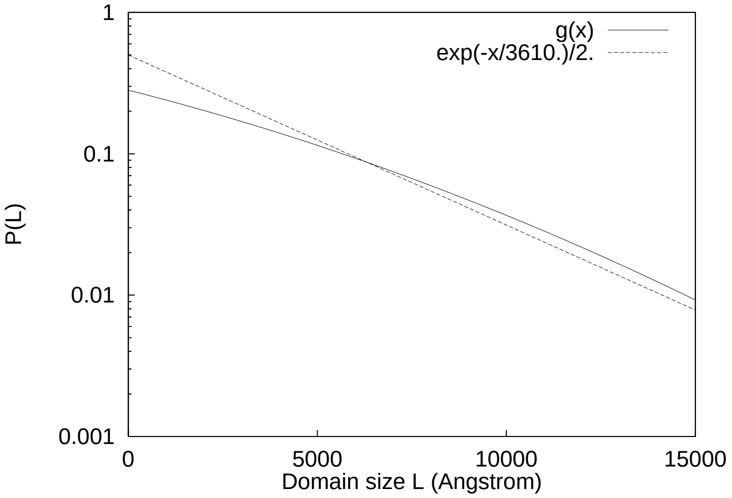

Figure 3.2: Solid line: Gaussian $P(L)$ for $L_G = -16250$Å (N = 266) and $\sigma_G = 10210$Å (N = 167). Dashed line: Exponential $P(L)$ with $L_E = 3600$Å (N = 59).

line respectively.

This suggests that one might consider $P(L)$ distributions with only one free parameter. A simple exponential,

$$P(L) \sim e^{-L/L_E} \tag{3.16}$$

was considered. Fitting to the same data set, the dashed line in Fig. 3.2 shows that $P(L)$ from Eq. 3.16 is not much different from Eq. 3.15 over the most important range of L. The corresponding effective fine-size factors are plotted in Fig. 3.4.

Because the two distributions are similar (as seen in Fig. 3.2) they both give

Table 3.1: Comparison between fitting results; Gaussian vs. exponential $P(L)$.

	Exp	Gauss	Gauss*
χ^2	3.4	3.7	4.0
I_2/I_1	2.24±0.08	2.32±0.09	2.39±0.08
η_1	0.073±0.003	0.076±0.003	0.078±0.003
L_E	3600 ± 150	–	–
L_G	–	-16250±52110	3000
σ_G	–	10210±11400	4150 ± 190
$\langle L \rangle$	3600± 150	4000± ??	3800± 200

* Constrained fit with $L_G = 3000$Å.

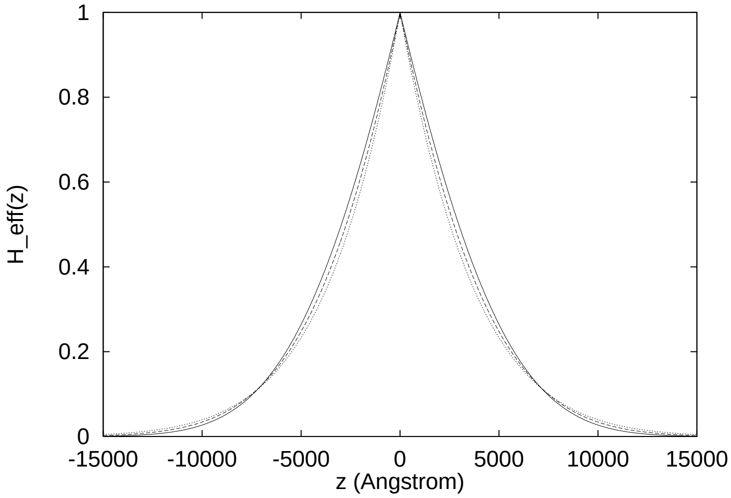

Figure 3.3: Finite-size factors for Gaussian $P(L)$ with $L_G = 4000$Å and $\sigma_G = 4000$Å (solid), $L_G = 0$Å and $\sigma_G = 5500$Å (dashed), $L_G = -10000$Å and $\sigma_G = 8000$Å (dotted)

practically the same H_{eff} and the same average domain size $\langle L \rangle$. Also, the other fitting parameters are almost the same (see Table 3.1).

In general, the exponential $P(L)$ has given smaller χ^2. Therefore, it was used in the final version of the fitting program for all the data. The benefit is that the exponential has only one parameter to be determined, L_E, which is roughly the average domain size. For H_{eff}, Eq. 3.13 gives

$$H_{eff}(z) \approx L_E \, e^{-z/L_E}. \tag{3.17}$$

Dutta and Sinha (1981) also proposed a one-parameter model (which we call the classical theory) but with much different functional form,

$$H_C(z) = L_C \, e^{-\pi z^2/L_C^2}. \tag{3.18}$$

The parameter L_C is similar to L_E; it plays the role of the average domain size. The analytical behavior of Eq. 3.18 is considerably different near $L = 0$ from the behavior of either of the distributions, that we have employed, as can be seen in Fig. 3.4. This different behavior of H_C with z has been shown to worsen the quality of the fits (Zhang et al., 1996), especially near the maximum in the peak intensity.

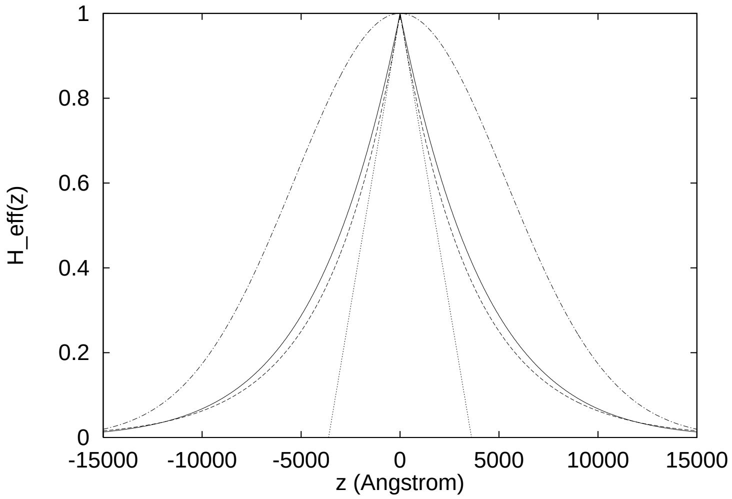

Figure 3.4: Finite-size factors corresponding to the domain distributions shown in Fig. 3.2 (Gaussian: solid line, and exponential: dashed line). The dotted line represents the finite-size factor for a single domain with $L = 3600\text{Å}$ and the dash-dotted line shows the classical finite-size factor. All functions are scaled to 1 at $z = 0$ to emphasize the functional forms; proper normalization requires constant area under each curve.

Chapter 4

X-ray Data

4.1 Introduction

The experimental technique employed in this work has been developed in our laboratory starting in 1993. Lipid multilamellar vesicles under various osmotic pressures have been investigated using the high resolution X-ray configuration at the F3 station at Cornell High Energy Synchrotron Source (CHESS). In average we made one CHESS trip a year with runs of 7 to 14 days. Because of the location and the time frame, the CHESS trips required very careful preparation. Samples had to be prepared in advance and the objectives and protocols clearly stated and assumed by all team members. This effort was rewarded by high quality data.

Fig. 4.1a shows a usual linear plot of the scattering data from a fully hydrated DMPC sample. The same data are plotted on a logarithmic scale in Fig. 4.1b to show the quality of the data and of the MCT fit. The signal to noise ratio is about 4 in the peak tails and the background is practically negligible for most of the data range. The peaks are very narrow, indicating a well defined lamellar spacing throughout the lipid sample. The expanded scale in Fig 4.2 gives a better view of the peak shape as a function of peak index h. In order to extract the fluctuation parameter η_1, with our instrumental resolution of 0.002 deg in 2θ, it is sufficient to take data within ± 0.1 deg from the peak center.

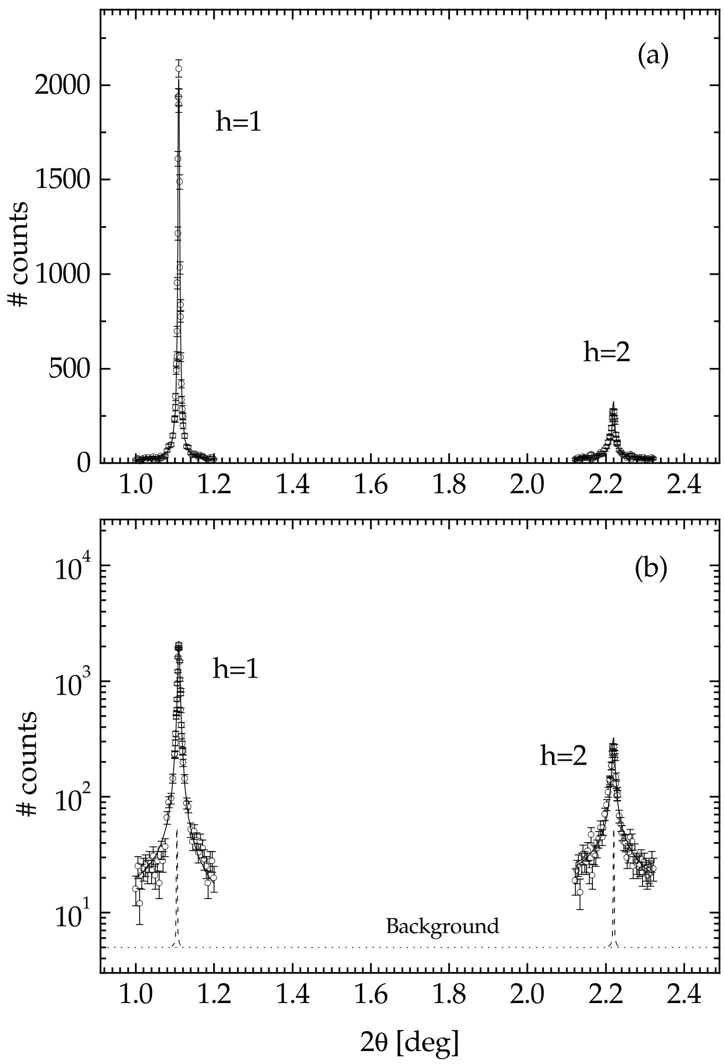

Figure 4.1: (a) Low angle scattering data from fluid phase DMPC at T=30^{o}C. The intensity is normalized to 10^5 monitor counts (typical counting time). (b) Same data as in (a) on log scale. The dotted line shows the background level and the dashed lines the resolution function. The solid line represents the MCT fit.

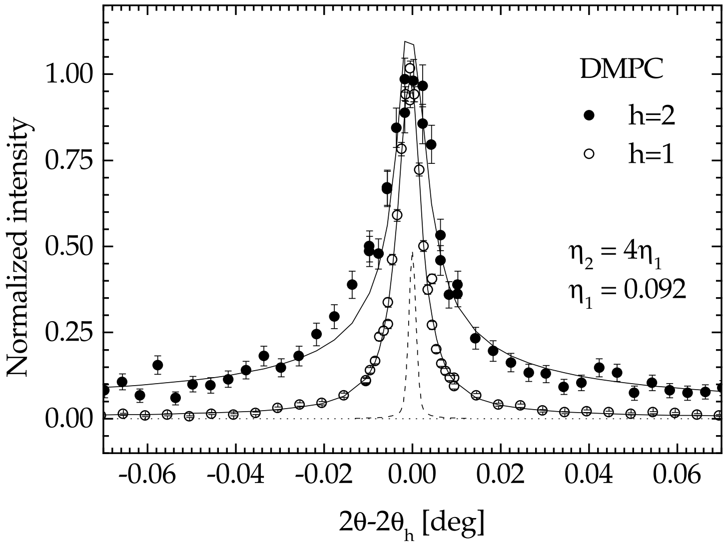

Figure 4.2: MCT fits to DMPC data. The amplitudes are normalized to 1 and the peaks are superimposed in order to emphasize the peak tails. The intrumental resolution is shown by the dashed line.

With few exceptions, the fit quality was good (χ^2s are given in the summary tables in Section 4.4). The goodness of fit is remarkable since the scattering peaks are very sharp, as shown in Fig 4.2. Usually χ^2 is larger for higher PVP concentrations for which the peak width approaches the resolution function. Also, because of the small mechanical hysteresis in the 2θ arm (see Section 4.2), the coarse and the fine scan taken on the same peak are in some cases slightly shifted, giving a larger χ^2. Figure 4.3 shows deviation plots for various DMPC fits. The largest deviations occur in the region close to the top of the peak. However the Caillé parameter η_1 is obtained from the peak tails (see Fig. A.2 in Appendix A) where the fit deviations are much smaller.

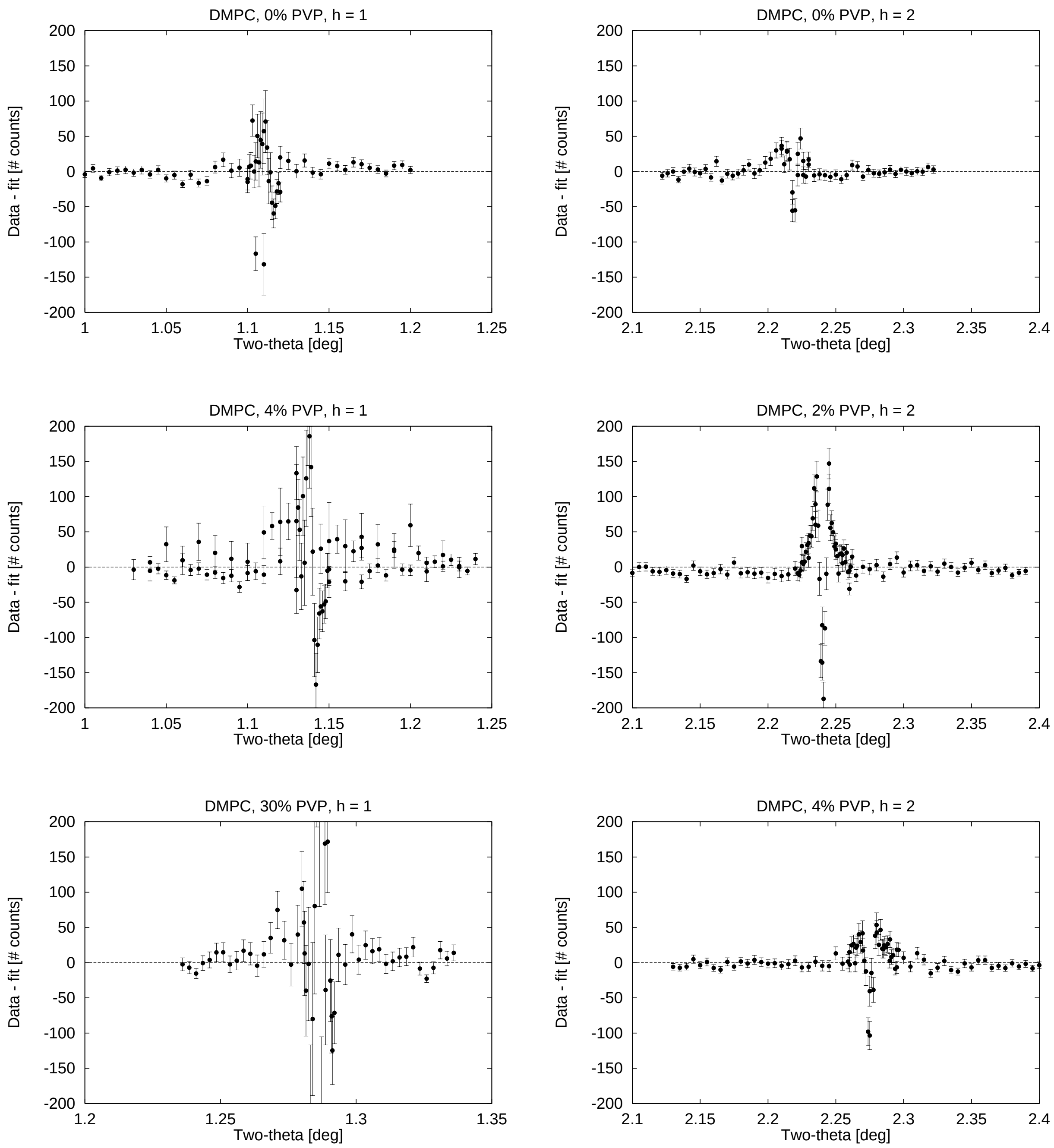

Figure 4.3: Deviation plots for various DMPC fits.

4.2 High resolution X-ray scattering

A schematic diagram of the X-ray configuration is shown in Fig. 4.4.

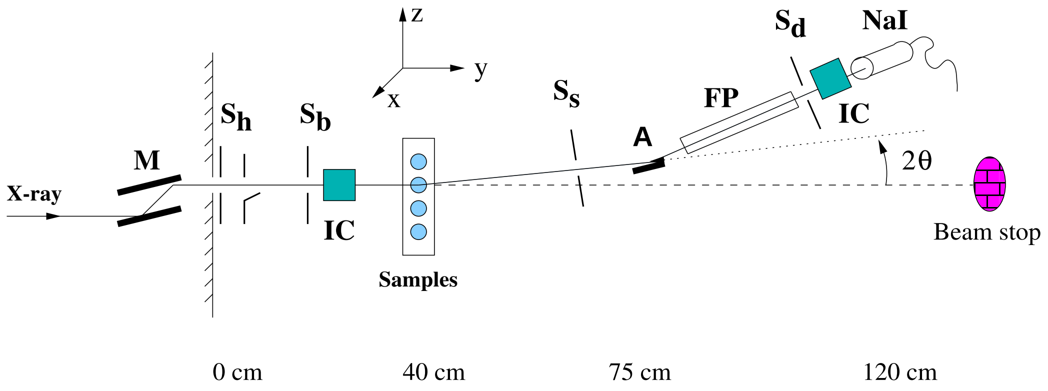

Figure 4.4: X-ray configuration at the F3 station at CHESS. S_h = hutch slits, S_b = sample slits, S_s = scatter slits, S_d = detector slits, A = analyser crystal, IC = ion chambers (monitor and detector), NaI = scintillator detector, FP = flight path.

The beamline monochromator (M) was used to select X-rays with $\lambda = 1.2147$Å. For this we set to the W_L absorption edge which is known precisely (10.207 keV). An in-plane resolution of 0.002 deg (FWHM) in 2θ was achieved using a silicon analyzer crystal (A) for selecting the scattered radiation (Zhang, 1995; Als-Nielsen et al., 1980). As shown in Fig. 4.4, the detector arm is rotated according to the scattering angle of the analyzer crystal (22.3 deg for Si(111) for $\lambda = 1.2147$Å). The beam dimensions were defined by the sample slits (S_b). The flux at the sample was $4{\cdot}10^9$ photons/sec in an area of 0.75 mm (vertical) x 1.0 mm (horizontal). The ion chamber detector (IC) in front of the samples was used to monitor the incoming X-ray flux. Normal X-ray exposures were 15-30 minutes and negligible damage occurred for periods of up to an hour as assayed by observing negligible changes in the width and position of the first order peak. The scattered intensity was measured using a NaI scintillation detector. The ion chamber in front of the NaI detector was used to locate the main beam ($2\theta = 0$) and to measure the resolution function (Zhang, 1995).

The low background (Fig. 4.1b) was achieved by carefully shielding the detector from stray radiation. This was done using Pb tape to enclose the region of the scatter slits (S_s), analyser (A), detector slits (S_d), and detectors. Also, the acceptance of the hutch entrance slits (S_h) was minimized in order to prevent stray radiation from entering the hutch.

For each peak a coarse step scan in 2θ was taken to obtain data well into the tails of the peak, *e.g.,* for the second order reflection centered at $2\theta_2$ the range for 2θ was $2\theta_2 \pm 0.1$ deg. At the end of the range for each order h, the signal to background ratio was between 3 and 7 depending on the PVP concentration. A fine step scan (*e.g.*, of total width 0.02 deg for $h = 2$) was then taken to obtain more data in the central peak. The backgrounds were nearly constant, with values of 5 and 7 counts for water and 40% PVP solutions, respectively, compared to roughly $10^3 - 10^4$ counts at the top of the first order peak. Lamellar D-spacing was determined from the second order peak; no slit smear correction was necessary due to the small beam size in the out-of-scattering-plane direction.

4.3 Sample preparation

The sample preparations for the CHESS studies were carried out by Dr. Stephanie Tristram-Nagle. DMPC (1,2-dimyristoyl-*sn*-glycero-3-phosphatidylcholine), EPC (egg phosphatidylcholine) and DOPC (1,2-dioleoyl-*sn*-glycero-3-phosphatidylcholine) were purchased from Avanti Polar Lipids (Alabaster, AL) in the lyophilized form and were used without further purification. Thin layer chromatography using chloroform:methanol:7 N NH_4OH (46:18:3, v/v) revealed only a single spot when stained with a molybdenum blue reagent (Dittmer and Lester, 1964). Polyvinylpyrrolidone (PVP) with a molecular weight of 40,000 was purchased from Aldrich Chemical Co. and dried in a vacuum oven at 70^oC overnight. PVP/water solutions from 0 to 60% PVP (w:w) were prepared by mixing PVP with Barnstead deionized nanopure water in 3 ml nalgene vials and allowed to equilibrate overnight at room temperature. PVP solutions were added to lipid at nominal 3:1 (when 40% PVP in water and below) or 5:1 (when 45% PVP in water and above) weight ratio in 0.1 ml nalgene vials. The samples were kept at room temperature for 24 hours with occasional vortexing. Thin walled 1.0 mm glass X-ray capillaries (Charles Supper Co.) were cleaned by sequentially washing with a chromic acid bath, deionized water, acetone and finally copious amounts of deionized water. After drying with nitrogen, the capillaries were flame-sealed at one end. About 10 mg lipid dispersion was then loaded into each capillary and these samples were centrifuged for 10 min at 1100g in a small, nalgene holder using a glycerol cushion. The capillaries were then flame sealed and loaded into cassettes with 12 slots/cassette with the ends of the capillaries embedded in a slab of silicone sealer to insure further against evaporation.

The cassette was mounted so that the capillaries were positioned horizontally inside a cylindrical aluminum sample chamber with mylar windows for entry and exit of X-rays. The cassettes fit directly into a custom holder which was attached to X-Y-Z motorized translations to move the samples relative to the X-ray beam. Temperature was controlled to within 0.02^oC. Thin layer chromatography performed a month after the experiments generally gave lysolecithin contamination less than 2% which is comparable with the fraction found in unexposed samples.

4.4 Fitting results

The backgrounds were subtracted from scattering data before fitting all orders simultaneously using the modified Caillé theory (see Chapter 3 and Appendix C). The parameters determined by the fitting program are the Caillé η_1 fluctuation parameter, the average domain size L_E, and the fluctuation corrected (and Lorentz-corrected) ratios of form factors $r_h \equiv |F_h/F_1|$.

The main fitting results are summarized in tables with the following legend:

PVP	Nominal PVP concentration
log P_{osm}	$\log_{10}$ (P_{osm}[dyn/cm^2])
D	D-spacing in Å
I_h	Number of counts on the h-th peak per 10^5 monitor counts
η_1	Caillé order parameter
F_h/F_1	Form factor ratios given by MCT
L_E	Average domain size in Å
χ^2	Reduced χ^2

4.4.1 EPC

Table 4.1: EPC, T=30^{o}C.

PVP	0%	2%	2%	4%
log P_{osm}	-	4.62	4.62	5.03
D	66.32	64.58	64.43	63.50
I_1	887	1492	1490	2836
I_2	127	140	126	262
η_1	0.137 ± 0.009	0.103 ± 0.004	0.101 ± 0.004	0.088 ± 0.003
F_2/F_1	1.477 ± 0.040	1.300 ± 0.027	1.290 ± 0.023	1.270 ± 0.021
L_E	1150 ± 70	2820 ± 125	2680 ± 100	3420 ± 115
χ^2	2.39	2.87	1.86	2.75

PVP	5%	10%	15%
log P_{osm}	5.21	5.77	6.2
D	62.08	60.20	58.11
I_1	1560	4715	4325
I_2	260	526	393
I_3	-	25	32
η_1	0.068 ± 0.005	0.044 ± 0.003	0.032 ± 0.004
F_2/F_1	1.474 ± 0.036	1.006 ± 0.018	0.857 ± 0.022
F_3/F_1	-	0.458 ± 0.031	0.531 ± 0.048
L_E	2420 ± 130	3600 ± 140	2990 ± 120
χ^2	1.54	1.47	1.88

Table 4.2: EPC, T=30^{o}C, *cont.*

PVP	25%	35%	45%	55%
log P_{osm}	6.80	7.20	7.47	7.73
D	56.54	54.70	53.48	51.24
I_1	13495	13135	7080	8565
I_2	1165	860	348	121
I_3	50	177	84	61
I_4	12	17	16	32
η_1	0.031 ± 0.003	0.028 ± 0.003	0.025 ± 0.003	0.018 ± 0.004
F_2/F_1	0.788 ± 0.016	0.642 ± 0.016	0.508 ± 0.018	0.288 ± 0.015
F_3/F_1	0.547 ± 0.041	0.621 ± 0.029	0.558 ± 0.035	0.418 ± 0.039
F_4/F_1	0.455 ± 0.087	0.282 ± 0.142	0.414 ± 0.092	0.424 ± 0.065
L_E	8290 ± 500	7560 ± 320	6170 ± 500	4950 ± 300
χ^2	2.84	3.47	2.07	2.57

4.4.2 DMPC

Table 4.3: DMPC 1997, T=30^{o}C.

PVP	0%	2%	4%	6%
log P_{osm}	-	4.57	5.03	5.27
D	62.71	62.12	61.19	60.82
I_1	2088	5040	2716	3064
I_2	271	668	452	459
η_1	0.092 $\pm$ 0.004	0.082$\pm$0.003	0.073$\pm$0.003	0.070$\pm$0.003
F_2/F_1	1.577 $\pm$ 0.031	1.505$\pm$0.024	1.495$\pm$0.025	1.370$\pm$0.023
L_E	4680 $\pm$ 160	5990 $\pm$ 240	3620 $\pm$ 140	5370 $\pm$ 190
χ^2	2.86	4.81	3.31	2.46

PVP	8%	10%	10%
log P_{osm}	5.60	5.76	5.76
D	59.62	58.89	58.79
I_1	1892	3722	2826
I_2	331	545	469
η_1	0.056 $\pm$ 0.003	0.048 $\pm$ 0.003	0.043 $\pm$ 0.002
F_2/F_1	1.345 $\pm$ 0.022	1.235 $\pm$ 0.022	1.173 $\pm$ 0.015
L_E	4420 $\pm$ 150	4020 $\pm$ 150	3730 $\pm$ 80
χ^2	1.52	4.45	1.60

Table 4.4: DMPC 1997, T=30^{o}C, *cont.*

PVP	20%	30%	30%
log P_{osm}	6.49	6.95	6.96
D	56.30	54.08	53.35
I_1	4627	5873	5794
I_2	748	737	667
I_3	30	53	58
η_1	0.036 ± 0.002	0.022 ± 0.002	0.020 ± 0.002
F_2/F_1	1.111 ± 0.020	0.872 ± 0.015	0.806 ± 0.013
F_3/F_1	0.420 ± 0.054	0.457 ± 0.022	0.482 ± 0.032
L_E	6180 ± 210	6410 ± 160	6460 ± 150
χ^2	2.15	1.59	1.37

PVP	45%	50%	60%
log P_{osm}	7.45	7.58	7.83
D	51.50	51.14	50.81
I_1	4892	4962	12957
I_2	287	244	377
I_3	49	58	81
I_4	14	17	40
η_1	0.033 ± 0.003	0.021 ± 0.002	0.020 ± 0.002
F_2/F_1	0.648 ± 0.015	0.540 ± 0.009	0.389 ± 0.008
F_3/F_1	0.490 ± 0.030	0.472 ± 0.021	0.347 ± 0.014
F_4/F_1	0.480 ± 0.093	0.417 ± 0.042	0.407 ± 0.032
L_E	6480 ± 100	7920 ± 130	14200 ± 370
χ^2	1.07	1.14	1.41

Table 4.5: DMPC 1996, T=30^{o}C.

PVP	0%	0%	5%	5%
log P_{osm}	-	-	5.20	5.19
D	63.36	63.23	62.84	61.63
I_1	1310	1050	1820	3090
I_2	245	175	410	473
η_1	0.104±0.006	0.114±0.007	0.058±0.006	0.057±0.004
F_2/F_1	1.795±0.059	1.794±0.057	1.428±0.047	1.344±0.030
L_E	3080 ± 320	2440 ± 220	1730 ±120	2350 ± 110
χ^2	1.58	1.27	1.94	1.24

PVP	10%	15%	20%
log P_{osm}	5.78	6.19	6.51
D	59.89	58.10	57.28
I_1	4040	5150	4775
I_2	928	830	812
η_1	0.032±0.003	0.030±0.003	0.025±0.003
F_2/F_1	1.197±0.023	1.106±0.024	1.055±0.019
L_E	2920 ± 120	3380 ±170	3560 ± 150
χ^2	2.25	1.57	1.84

PVP	25%	35%	45%
log P_{osm}	6.78	7.19	7.49
D	56.22	54.32	52.30
I_1	5530	7500	7930
I_2	757	912	460
I_3	44	62	59
I_4	-	-	16
η_1	0.025±0.002	0.024±0.003	0.026±0.003
F_2/F_1	0.972±0.017	0.850±0.023	0.610±0.014
F_3/F_1	0.419±0.030	0.484±0.041	0.450±0.026
F_4/F_1	-	-	0.357±0.058
L_E	6870 ± 570	14200 ± 4400	4170 ±180
χ^2	1.00	1.67	1.39

4.4.3 DOPC

Table 4.6: DOPC, T=30^{o}C.

PVP	0%	5%	10%	15%
log P_{osm}	-	5.24	5.74	6.21
D	62.9	61.4	58.5	57.0
I_1	1665	1320	6580	8645
I_2	143	134	610	770
I_3	-	-	-	72
η_1	0.110 ± 0.007	0.077 ± 0.006	0.059 ± 0.005	0.040 ± 0.002
F_2/F_1	1.264 ± 0.033	1.141 ± 0.038	1.038 ± 0.034	0.842 ± 0.014
F_3/F_1	-	-	-	0.640 ± 0.029
L_E	2900 ± 150	3100 ± 180	6600 ± 370	5750 ± 160
χ^2	2.71	2.00	9.57	1.98

PVP	20%	25%	30%	35%
log P_{osm}	6.55	6.85	6.95	7.15
D	55.1	54.3	53.9	53.7
I_1	6545	14600	5840	21075
I_2	478	1038	338	1790
I_3	80	205	64	456
I_4	-	-	-	38
η_1	0.037 ± 0.003	0.021 ± 0.002	0.033 ± 0.003	0.016 ± 0.002
F_2/F_1	0.761 ± 0.015	0.651 ± 0.012	0.670 ± 0.016	0.697 ± 0.016
F_3/F_1	0.690 ± 0.032	0.582 ± 0.026	0.677 ± 0.038	0.701 ± 0.030
F_5/F_1	-	-	-	0.363 ± 0.044
L_E	6500 ± 220	9300 ± 300	6320 ± 230	> 10000
χ^2	1.64	2.59	2.69	7.37

Table 4.7: DOPC, T=30^{o}C, *cont.*

PVP	40%	45%	50%	60%
log P$_{osm}$	7.36	7.47	7.62	7.84
D	54.0	51.6	50.8	49.8
I_1	6363	2843	13125	28838
I_2	392	105	290	270
I_3	83	37	155	272
I_4	12	14	28	122
η_1	0.032 ± 0.002	0.033 ± 0.005	0.018 ± 0.003	0.013 ± 0.002
F_2/F_1	0.635 ± 0.013	0.461 ± 0.017	0.329 ± 0.015	0.211 ± 0.013
F_3/F_1	0.663 ± 0.028	0.601 ± 0.048	0.493 ± 0.037	0.405 ± 0.028
F_4/F_1	0.365 ± 0.083	0.601 ± 0.123	0.346 ± 0.050	0.481 ± 0.083
L_E	4600 ± 100	3400 ± 80	9860 ± 420	> 10000
χ^2	1.82	1.23	2.42	6.92

Chapter 5

Structure Determination

5.1 Introduction

A major goal has been to obtain reliable structure determinations of lipid bilayers. The central quantity A (area/lipid) in the L_α phase (50^{o}C), was first obtained in this laboratory for DPPC. In this chapter we use similar methods to obtain A and the structure of three more lipids, DMPC, EPC and DOPC. By using high instrumental resolution synchrotron X-rays, we were able to correct for the effect of fluctuations on the scattering peak (Zhang et al., 1996) as described in Chapter 3. Another key element in our analysis (Nagle et al., 1996) was to determine the difficult fluid (F) phase structure by making use of measured differences with the structure of the gel (G) phase; G phase structure is determined independently because of the extra data from wide angle scattering (Sun et al., 1994). At first, it would seem to be difficult to employ this method for samples with no G phase (EPC) or with poorly characterized G phase (DOPC). However, the method assumes only that the headgroups are the same in both lipids being compared. Therefore, we propose to use measured differences between the F phase to be determined and the G phase DPPC. A check of our method is provided by results for DMPC, in an independent structure determination that uses quite different procedures (Koenig et al., 1997).

With our investigation method, namely X-ray diffraction, we can obtain the electron density profile $\rho^*(z)$ along the bilayer normal z, from which we can then identify the location of different lipid components. The scattered intensity is a function of the electron contrast between the lipids and the water molecules and it is instructive to estimate this contrast. Let us consider the benchmark lipid DPPC at 50^{o}C. The total number of electrons in a DPPC molecule is $n_L^* = 406e$ and the lipid volume is

$V_L = 1232\text{Å}^3$ (Nagle and Wiener, 1988). This gives an average lipid electron density $\rho_L^* \approx 0.33e/\text{Å}^3$ that matches the water electron density (at 50^o) $\rho_W^* = 0.330e/\text{Å}^3$. There is however an electron density gradient across the lipid bilayer that produces observable scattering peaks. The highest electron density is in the headgroup region, due to the phosphorus atom. The total number of electrons in the headgroup, including the carbonyls, is $n_H^* = 164e$. With a headgroup volume $V_H = 319\text{Å}^3$ (Sun et al., 1994) this gives $\rho_H^* \approx 0.51e/\text{Å}^3$. The lowest electron density is at the bilayer center where the terminal methyls are located. Using $V_{CH_3} = 54.6\text{Å}^3$ (Petrache et al., 1997) we obtain $\rho_{CH_3}^* \approx 0.16e/\text{Å}^3$. These extremes are to be compared with the water electron density $\rho_W^* = 0.33e/\text{Å}^3$. This rough calculation gives just an estimate of the density gradient across the lipid bilayer because the density profile is smeared out by thermal fluctuations of the lipid molecules.

Next we proceed with the calculation of the actual density profiles and of the basic structural parameters. With the form factors F_h, obtained from the MCT fits, absolute electron density profiles can be calculated as

$$\rho^*(z) - \rho_W^* = \frac{1}{D}F(0) + \frac{2}{D}\,F_1 \sum_{h=1}^{h_{max}} \alpha_h\, r_h\, \cos\left(\frac{2\pi h z}{D}\right), \tag{5.1}$$

where $h_{max} = 4$ for our data. The phase factors $\alpha_h = (-,-,+,-)$ are well established for these lipids (McIntosh and Simon, 1986a).

The quantity $\rho_W^* = 0.333e/\text{Å}^3$ is the water electron density at 30^oC. The "zero-order" form factor $F(0)$, which represents the total electron contrast between the bilayer and the water solution, is given by Nagle and Wiener (1989),

$$AF(0) = 2(n_L^* - \rho_W^* V_L) = 2(\rho_L^* - \rho_W^*)V_L, \tag{5.2}$$

where A is the area per lipid, n_L^* is the number of electrons in the lipid molecule, V_L is the lipid volume and $\rho_L^* \equiv n_L^*/V_L$ is the average electron density of the lipid molecule. The first order diffraction form factor F_1 is initially undetermined, so only the ratio $r_h = |F_h/F_1|$ of form factors can be measured directly. This means that only relative electron density profiles can be routinely obtained. Determining F_1 and the absolute electron density profiles will be accomplished in Section 5.2.4.

5.2 Results

5.2.1 Headgroup spacing D_{HH}

The headgroup spacing D_{HH} is defined to be the distance between the two peaks in the electron density profile and is usually supposed to be a good approximation to the phosphate-phosphate thickness of the bilayer (Pearson and Pascher, 1979). D_{HH} is the same, of course, for the relative and the absolute electron density profiles. In practice, at least four orders ($h_{max} = 4$) are needed to obtain a reasonably accurate estimate of D_{HH}. Furthermore, even with four orders, the measured D_{HH} needs to be corrected due to the limited number of Fourier terms. For this correction we follow the procedure introduced by Sun et al. (1996). Four orders of diffraction allow a quite good estimate of D_{HH}, but this estimate is systematically biased as D_{HH}/D varies with dehydration. Electron density models have been used to estimate the correction (Sun et al., 1996). We have used models where the headgroup electron density profile is represented by one Gaussian peak because this is close to the resolution of our data. More refined electron density models, such as two Gaussians in the headgroup region (Wiener et al., 1989) should be used to estimate the correction if more orders of diffraction are obtained. It may be noted that the corrections to D_{HH} range from 1.9$\mathring{A}$ at $P = 10$ atm to 0.2$\mathring{A}$ at $P = 56$ atm.

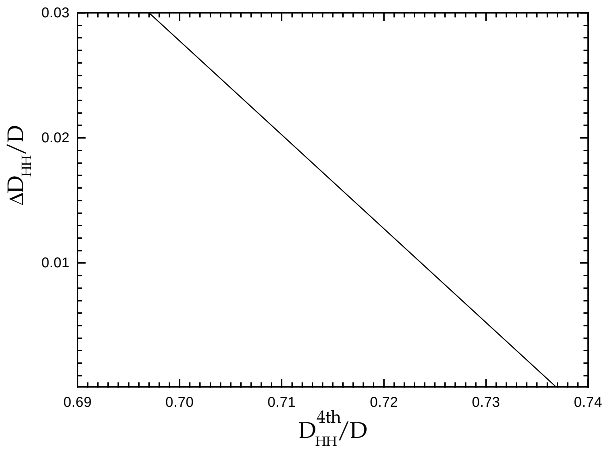

Figure 5.1: Corrections $\Delta D_{HH} = D^{4th}_{HH} - D^{true}_{HH}$ obtained by Sun et al. (1996)

The information on D_{HH} must be supplemented with volumetric measurements in order to obtain the area per molecule. The basic information needed are shown in Table 5.1 at the end of this chapter. Relative electron density profiles were first obtained for samples under osmotic pressure that have four orders of diffraction. Fig. 5.2 shows typical absolute electron density profiles; the conversion to absolute electron density, performed in Section 5.2.4, is not necessary to obtain D_{HH}. The corrected head group spacing D_{HH} was then obtained from the electron density profiles, and the value of D_{HH} is given in Table 5.2 for EPC at $P = 29$ atm, for DMPC at $P = 27$ atm, and for DOPC at $P = 56$ atm.

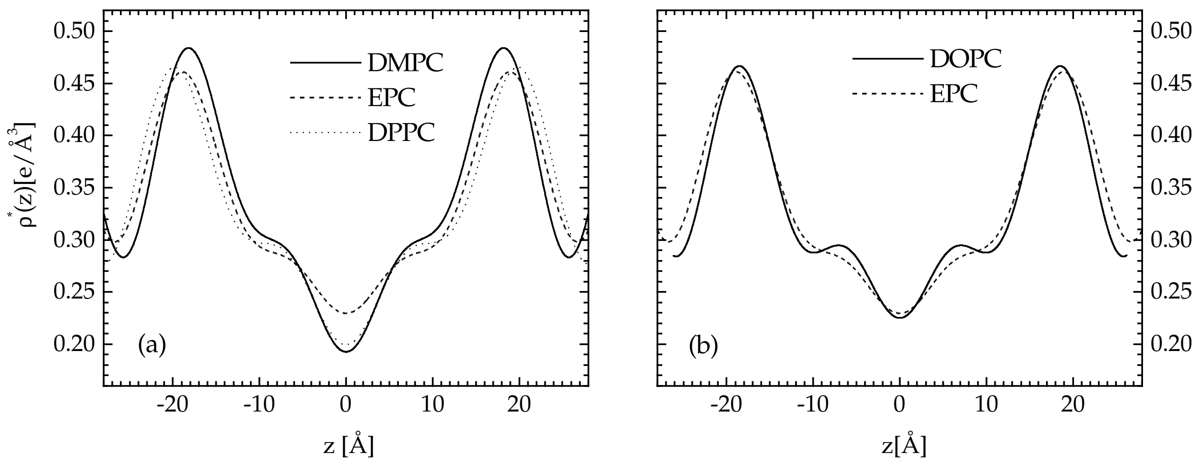

Figure 5.2: Absolute electron density profiles $\rho^*(z)$. Panel (a): DMPC (solid), EPC (dashed) and DPPC (dotted); Panel (b): DOPC (solid) and EPC (dashed).

5.2.2 Area per lipid molecule

The area per molecule is obtained following a procedure initiated by McIntosh and Simon (1986a) and employed by Nagle et al. (1996). These studies compared a lipid bilayer in the F phase with the same lipid in the G phase. Here we extend this method to compare a lipid bilayer in the F phase with a different lipid in the gel phase, provided only that the headgroup is the same for both lipids. Since this is not an obvious extension, a derivation is now given.

The first basic assumption is that headgroups are fully solvated for both the reference R lipid bilayer and the F phase lipid bilayer under study. (Note that the reference lipid bilayer R could be either G phase or F phase.) Under the condition that the headgroups are chemically identical, the headgroup volume is therefore the same in R as in F. This means that the difference in lipid volumes is given by the difference in the volumes of the remainder of the molecule

$$V_L^F - V_L^R = A^F D_C^F - A^R D_C^R, \tag{5.3}$$

where D_C is half the thickness of the hydrocarbon region, corresponding to one monolayer. The condition that the headgroups are chemically identical also plays a role in the second basic relation

$$D_C^F - D_C^R = (D_{HH}^F - D_{HH}^R)/2. \tag{5.4}$$

This assumes that the major determinant of differences in D_{HH} is differences in the hydrocarbon region, which is a reasonable approximation even if the headgroup tilt is different because the lever arm for the distance between the phosphate group and the carbonyls is short. Solving Eqs. 5.3 and 5.4 for A^F yields

$$A^F = \frac{V_L^F - V_H^R}{D_C^R + \Delta D_{HH}/2}. \tag{5.5}$$

In our study we take DPPC in the gel phase to be our reference lipid with headgroup volume $V_H^R = 319\text{Å}^3$ determined by Sun et al. (1994). Values of A^F were obtained from Eq. 5.5 for samples with four orders of diffraction and one of these values is given in Table 5.2 for non-zero values of P.

The external osmotic pressure not only pushes the bilayers closer to one another by decreasing D_W, but also removes water by decreasing A (Parsegian et al., 1979).

Since the lipid volume remains constant with varying P_{osm} (White et al., 1987), the bilayer thickness increases with increasing P_{osm}. The change in area with the applied osmotic pressure is determined by the bilayer compressibility modulus K_A; the defining relation is

$$A - A_0 = -AD_W P/K_A. \tag{5.6}$$

A linear fit to A vs. $AD_W P$ gives the fully hydrated area A_0 as the intercept at $P = 0$, and the slope $-1/K_A$, from which the compressibility modulus K_A can be obtained. For DMPC and EPC the fits are shown with solid lines in Fig. 5.3a. Standard deviations are shown with dotted lines. Our best fit to DMPC data gives $A_0 = 60.2 \pm 1.0\text{Å}^2$ and $K_A = 108 \pm 35$ dyn/cm. Our result for K_A agrees with Evans and Rawicz (1990) ($K_A = 145 \pm 10$ dyn/cm) and the more recent measurement of Koenig et al. (1997) ($K_A = 136\,(123-152)$ dyn/cm), who also report a fully hydrated area $A_0 = 59.5 \pm 0.2\text{Å}^2$. Agreement for A_0 with Koenig et al. (1997) becomes even better if we constrain K_A to their value. Then, we obtain $A_0 = 59.7 \pm 0.2\text{Å}^2$. For EPC our best fit in Fig. 5.3 yields $A_0 = 69.4 \pm 1.2\text{Å}^2$ and $K_A = 116$ dyn/cm.

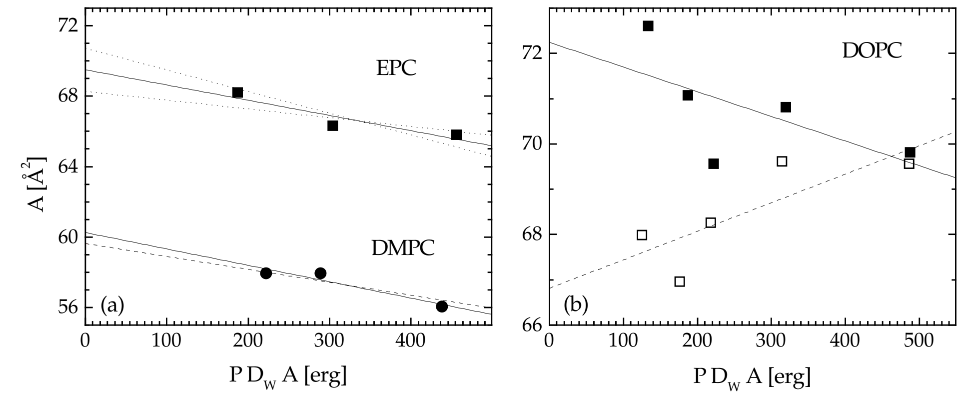

Figure 5.3: Determination of A_o and K_A. Panel (a) EPC: solid line represents the best fit giving $K_A = 116$ dyn/cm and the dotted lines show one standard deviation corresponding to $K_A = 201$ dyn/cm (smaller slope) and $K_A = 81$ dyn/cm (larger slope). DMPC: dashed line is the best unconstrained fit giving $K_A = 108$ dyn/cm and the solid line shows the fit constrained to $K_A = 136$ dyn/cm from Koenig et al. (1997). Panel (b) DOPC: solid line represents the best fit to corrected D_{HH} (solid symbols) giving $K_A = 188$ dyn/cm. Open symbols show the uncorrected D_{HH} with the unphysical negative K_A fit (dashed line).

Fig. 5.3b compares the uncorrected with the corrected D_{HH} data for DOPC. Our direct data for A are limited to samples under modest osmotic pressures P, from 10 to 56 atm, and the data points are rather scattered from the straight line that is required for an elastic compressibility modulus. Nevertheless, these data suffice to obtain a reasonably precise extrapolation to a fully hydrated area $A_o = 72.2 \pm 1.1$Å. The scatter in the data make it much more difficult to obtain a precise value for K_A, because of $\approx$ 50% error in the slope $1/K_A$. The best fit, shown with the solid line in Fig. 5.3b, gives $K_A = 188$ dyn/cm. Note that using the uncorrected D_{HH} (open symbols) may lead to the unphysical result that K_A is negative (dashed line).

5.2.3 Other structural quantities

With the area A determined, we can now calculate many structural parameters of interest. The results are summarized in Table 5.2. For each lipid we present the results for the fully hydrated sample ($P = 0$) and for one of the less hydrated samples. The hydrocarbon thickness per monolayer is $D_C = (V_L - V_H)/A$. The Luzzati bilayer thickness is defined as $D_B = 2V_L/A$ and the corresponding water thickness is $D_W = D - D_B$ with the number of waters per lipid $n_W = AD_W/(2V_W)$. The steric definition of the bilayer thickness (McIntosh et al., 1987, Nagle and Wiener, 1988) is $D'_B \equiv 2(D_C + D_H)$, where we choose $D_H = 9$Å, consistent with neutron diffraction results (Buldt et al., 1979), to estimate the PC headgroup thickness. Fig. 5.5 shows where these various thicknesses fall on the electron density profile. Using D'_B we then calculate the interbilayer spacing $D'_W \equiv D - D'_B$ and the number of water molecules in the headgroup region $n'_W \equiv A(D'_B - D_B)/(2V_W)$.

5.2.4 Absolute electron density profiles

Once the area per molecule is known, the electron density in Eq. 5.1 can be set on an absolute scale. Starting with Eq. 5.2, F(0) is determined. In order to calculate F_1 we consider the headgroup peak integral H, above the water level, which is defined as

$$H = \int_{D_C}^{D/2} (\rho^*(z) - \rho^*_W) dz. \tag{5.7}$$

Then, we have

$$AH = n_H^* - \rho_W^* V_H = (\rho_H^* - \rho_W^*) V_H. \tag{5.8}$$

For a PC headgroup, $n_H^* = 164e$ and at $T = 30^o$C Eq. 5.8 yields $AH = 57.7e$. This value of AH should be a constant for all lipids with PC headgroups. This derivation assumes that there is only water, and no hydrocarbon, mixed with the headgroups; although this is undoubtedly not true, the electron density of the methylene region is quite close to ρ_W^*, so this is still a good approximation. (A further refinement could be constructed along the lines of the development given by Nagle and Wiener (1989), but this is unwarranted for only four orders of diffraction.) Then, F_1 in Eq. 5.1 is varied until the headgroup peak in the electron density profile gives a value of H, which together with the already determined A, satisfies Eq. 5.8. Fig. 5.2 shows absolute electron density profiles.

5.2.5 Continuous transforms

In the previous section we focused on partially dehydrated samples which, having a lower level of fluctuations, have more diffraction peaks. We now test whether there is any major structural change upon mild dehydration that could invalidate the extrapolation of A in Fig. 5.3. If there is no structural change at all, then the form factors must all lie on the same continuous transform (Torbet and Wilkins, 1976; McIntosh and Simon, 1987), defined as

$$F(q) = \int_{-D/2}^{D/2} [\rho^*(z) - \rho_W^*] \; e^{-iqz} dz. \tag{5.9}$$

Fig. 5.4 shows the continuous transforms for each lipid, obtained using the sampling theorem,

$$F(q) = \sum_{h=-h_{max}}^{h_{max}} F_h \frac{\sin[(q - q_h)D/2]}{(q - q_h)D/2} \, , \tag{5.10}$$

where $q_h = 2\pi h/D$ and F_h was obtained for each lipid under one particular osmotic pressure P'. Then, the first order form factors F_1 for all other samples were obtained by placement on the $F(q)$ curve. There are then no additional free parameters for the absolute values of the other F_h, which are shown in Fig. 5.4. Small systematic deviations of F_2 from the $F(q)$ curve, especially for DMPC, at values of P higher and lower than P' are consistent with the effect of area compressibility shown in Fig. 5.3, as we checked by varying the bilayer thickness in model electron density profiles of the 1-Gaussian hybrid type (Wiener et al., 1989). However, the small deviations of the measured F_h from the continuous transform indicates that there are no major structural changes with the range of osmotic pressures P employed.

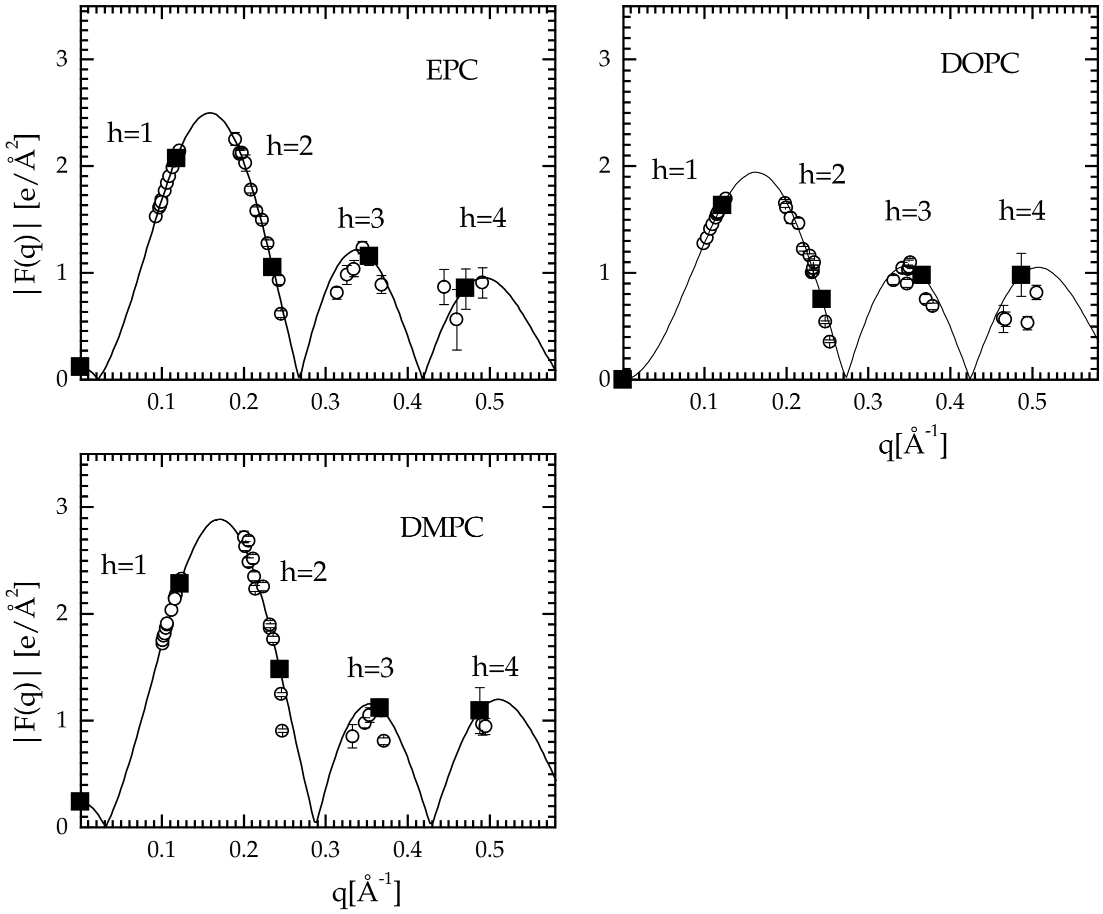

Figure 5.4: Absolute continuous transforms $|F(q)|$ obtained for EPC at $P' = 29$ atm, for DMPC at $P' = 27$ atm and for DOPC at $P' = 29$ atm. The solid symbols represent the form factors used in the reconstruction.

5.3 Discussion

The main structural results are the areas A^F for the fully hydrated biologically relevant L_α phase of EPC, DMPC and DOPC bilayers. Our result $A^F_{EPC} = 69.4\text{Å}^2$ at $T = 30^o$C is smaller than 74Å^2 obtained at $T = 25^o$C using the Luzzati gravimetric method (Lis et al., 1982) [1]. The gravimetric method typically overestimates A because, contrary to the assumption in that method, not all the weighed water goes between the bilayers until the excess water phase begins to form (Klose et al., 1988; Tristram-Nagle et al., 1993; Koenig et al., 1997). The gravimetric method was later modified (Rand and Parsegian 1989) to use data taken on samples under osmotic pressure together with a compressibility modulus $K_A = 145$ dyn/cm which was not measured for EPC but estimated from DMPC (Evans and Needham, 1987); the revised value 69.5Å^2 agrees very well with our value of 69.4Å^2. The agreement would not be quite so good if we also used this same value of K_A instead of our best $K_A = 116$ dyn/cm, nor if thermal expansion from $T = 25^o$C to $T = 30^o$C were taken into account. Using an area dilation of 5x$10^{-3}/^o$C (Evans and Needham, 1987) would add about 1Å^2 to A^F_{EPC}. However, our K_A has a large uncertainty, and this propagates a range of uncertainty $68.3 - 70.5\text{Å}^2$ in our A. Since a similar range of uncertainty applies to the modified gravimetric result, we suggest that there is agreement for EPC that $A^F_{EPC} = 69.4 \pm 1.1\text{Å}^2$ in the $T = 25 - 30^o$C range.

Our result $A^F_{DMPC} = 59.7\text{Å}^2$ for DMPC at $T = 30^o$C is lower than the value 65Å^2 obtained from the unmodified Luzzati gravimetric method (Lis et al., 1982) and even somewhat lower than the 61.7Å^2 obtained from modified gravimetric method (Rand and Parsegian, 1989), both at $T = 27^o$C. Recently, the gravimetric method has been further modified by combining it with NMR deuterium order parameter (S_{CD}) data as a function of osmotic pressure (Koenig et al., 1997). There is uncertainty in converting S_{CD} data into absolute values of A (Nagle, 1993; Koenig et al., 1997), but Koenig et al. (1997) argue that changes in A are accurately obtained. By using the gravimetric method to obtain A at low hydration, where it is likely that most of the water does go between the bilayers, and by using the K_A obtained from NMR, Koenig et al. (1997) obtained $A^F_{DMPC} = 59.5 \pm 0.2\text{Å}^2$ at $T = 30^o$C. This is excellent

[1] The gravimetric method uses samples with known amount of water and lipid and assumes that all weighed water goes in between lipid bilayers, i.e. it assumes no defect regions. The area per molecule is then determined from the volume of the unit cell $AD/2 = V_L + n_W V_W$.

agreement between the results of two different methods that involve quite different assumptions. We suggest that there is agreement that $A^F_{DMPC} = 59.6 \pm 0.2 \text{Å}^2$.

The area per lipid $A_o = 72.2 Å^2$ that we obtain for fully hydrated DOPC is considerably larger than the value $59.4 Å^2$ obtained by Wiener and White (1992) on dehydrated samples. Indeed, our value of A is so much larger than we had anticipated that it is worth emphasizing why the result must be at least qualitatively correct, by comparing to DPPC in the L_α phase. The molecular weight of DOPC (786) is greater than DPPC (734). The specific volume is very similar (only 1% larger for DPPC), so the molecular volume of DOPC ($1303 Å^3$) is larger than for DPPC ($1232 Å^3$). Nevertheless, the DOPC bilayer is thinner than the DPPC bilayer in the L_α phase, as shown in Fig. 5.2. This requires that A^{DOPC} be greater than A^{DPPC}, and Eq. 5.5 calculates by how much. Rand and Parsegian (1989) reported $A_o = 72.1 Å^2$ after reworking earlier data using an estimated compressibility $K_A = 145$ dyn/cm. This is much better agreement with our A_o than for DPPC where their method gives $A_o = 68.1 Å^2$ which is larger than the value $A_o = 62.9 Å^2$ that was obtained (Nagle et al., 1996) by the same methods employed in the present work. The earlier data (Lis et al., 1982) gave $A_o = 82 Å^2$ for DOPC using the unadulterated Luzzati method, which is now recognized as giving values of A_o that are too large (Tristram-Nagle, 1993; Koenig et al., 1997). However, Gruner et al. (1988) also used the Luzzati method and obtained $A_o = 70 Å^2$, but at the much lower temperature of 2^oC. Again at low temperatures, from calorimetry of the ice transition, it has been reported (Ulrich et al., 1994) that the number of waters/lipid n_W is 20 as opposed to our value of 32.5 given in Table 5.2; using $n_W = 20$ gives $A_o = 62 Å^2$ at 30^oC, which is clearly too small. However, these two low temperature results could be consistent with each other since the Luzzati method overestimates A_o and they could be consistent with our result at 30^oC if there is a strong temperature dependence in A_o and n_W for DOPC. This suggests that future studies of DOPC as a function of temperature could be interesting.

There are no literature values for area compressibility for DOPC to compare to our best value $K_A = 188$ dyn/cm. (The value $K_A = 145$ dyn/cm suggested in Table 1 of Rand and Parsegian (1989) was inferred from DMPC.) Considering other phosphatidylcholine lipids, Koenig et al. (1997) give $K_A = 136$ (123 to 152) dyn/cm for DMPC and $K_A = 210 \pm 10$ dyn/cm for SOPC for compression. For the same lipids under tension Evans and Needham (1987) give $K_A = 144.9 \pm 10.5$ dyn/cm and

$K_A = 199.6 \pm 12.7$ dyn/cm, respectively. Although our K_A for DOPC is not so precise, our best value is consistent with the intuition that K_A should increase with chain length and decrease with number of unsaturated $C = C$ bonds.

The large differences in A^F_{DMPC} and A^F_{DOPC} imply that the hydrocarbon chains have a considerable influence on A^F. Not surprisingly, unsaturation leads to larger A^F. Clearly, there is a 'fluidity' spectrum, and not just one generic brand of fluid chains.

The basic assumption in our method of obtaining A^F is that phosphatidylcholine headgroup dimensions are the same for different PC lipids in different phases. Now that the agreement with Koenig et al. (1997) lends support for this assumption, it is worth looking at these dimensions, as visualized in Fig. 5.5.

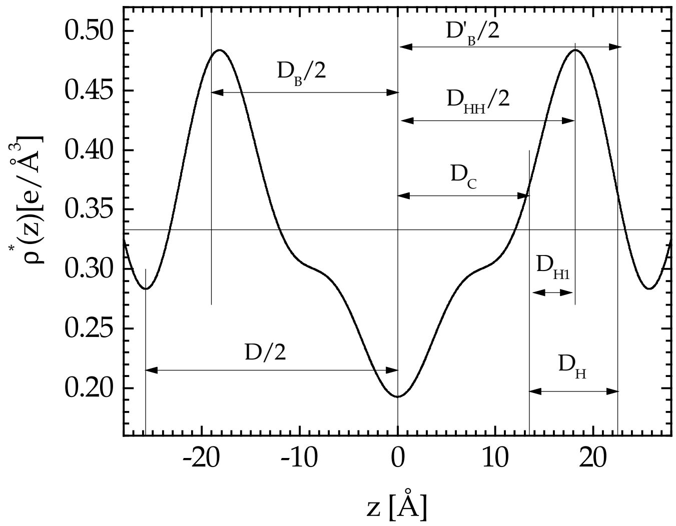

Figure 5.5: Comparison of various bilayer thicknesses with the $4th$ order Fourier electron density profile for DMPC at $P_{osm} = 27$ atm.

A newly defined thickness corresponds to that part of the headgroup that extends from the average hydrocarbon layer, defined as D_C, to the peak in the electron density profile; we define this as $D_{H1} = (D_{HH}/2) - D_C$. For PC headgroups (which in our definition include the glycerol group and the carbonyls), Table 5.2 gives $D_{H1} = 4.1$Å. (Note that D_{H1} appears a bit larger in Fig. 5.5 because of the correction to D_{HH} due to Fourier truncation.) Once D_{H1} and V_H are known for a given headgroup type, there is a simplified way to obtain A which is equivalent to the method developed in Eq. 5.5 in Section 5.2.2. First, one obtains $D_C = (D_{HH}/2) - D_{H1}$ from D_{H1} and the corrected D_{HH}. Then, one obtains $A = V_C/D_C$ where V_C is the hydrocarbon volume obtained using $V_C = V_L - V_H$, and of course, V_L is measured. It may also be noted that the basic assumption in this paragraph can be addressed with molecular dynamics simulations that would determine how much D_{H1} varies for different PC lipids in different phases.

Because we could not obtain enough orders of diffraction for fully hydrated F phase lipids, we applied osmotic pressure P which reduces the fluctuations. This meant that we had to extrapolate to $P = 0$ to obtain fully hydrated structure. This necessarily led us to obtain estimates for the area compressibility K_A (see Fig. 5.3). Although our estimates for K_A are not as accurate for DMPC as obtained by others (Koenig et al., 1997; Evans and Needham, 1987), they do agree. Furthermore, the errors for A^F remain small even though the errors for K_A are large, as can be seen in Fig. 5.3. In this context it should be mentioned that, if we had not corrected the head-head thickness D_{HH} following Sun et al. (1996), the slopes in Fig. 5.3 and the values of K_A would have been very large or even negative, which is physically unrealistic.

After the area per molecule was determined, we have set the electron density profiles (Fig. 5.2) and the continuous transforms (Fig. 5.4) on absolute scales. This was accomplished by evaluating the headgroup integral in Eq. 5.8 provided that the headgroup volume is known. One remarkable fact indicated by Fig. 5.2 is that the extreme values of the absolute electron density profiles are in agreement with our estimates at the beginning of this chapter, which were based on volumetric measurements.

From the plot of the absolute electron density profiles shown in Fig. 5.2 we observe that EPC and DOPC, which contain unsaturated fatty acid chains, have more disorder at the bilayer center compared to DMPC and DPPC, for both of which the methyl trough in the electron density profile is narrower and deeper, suggesting that the methyl groups at the chain ends are better localized. Although details of this kind may be obviated by Fourier truncation error, it nevertheless seems that the terminal methyls could be more delocalized for lipids containing unsaturated fatty acids, in agreement with the results of Holte et al. (1995).

Our analysis that determines A^F and K_A requires that there be no drastic structural changes over the range of P applied because extrapolation to $P = 0$ would then be invalidated. The fact that the data for all P fall close to the continuous transform in Fig. 5.4 confirms no large scale structural change. The small, systematic deviations of the $h = 2$ form factors for high and low P in Fig. 5.4 are consistent with small changes on the order of 1.5Å in D_B due to osmotic compression, as can be verified by varying the thickness in models of electron density profiles (Nagle and Wiener, 1989; McIntosh and Simon, 1987; Torbet and Wilkins, 1976).

Table 5.1: Volumetric results (30^{o}C).

	DMPC	EPC	DOPC
M_W [g/mol]	677.95	768.5	786.1
v_L [ml/g]	0.978	0.988	0.998
V_L [Å^3]	1101.	1260.6	1303.3
n_L^* [e]	374	424.2	434
$AF(0)$ [e]	14	8	0.001

Table 5.2: Structural results (30^{o}C).

	DMPC	DMPC	EPC	EPC	DOPC	DOPC
P [atm]	0	27	0	29	0	56
D [Å]	62.7	51.5	66.3	53.4	63.1	49.8
D_{HH} [Å]	34.4^a	35.2	35.4^a	36.6	35.3^a	36.4
A [Å^2]	59.7	57.9	69.4	66.3	72.2	69.0
D_B [Å]	36.9	38.0	36.3	38.0	36.1	37.3
D_W [Å]	25.8	13.5	30.0	15.4	27.0	12.5
n_W	25.7	13.0	34.7	17.0	32.5	14.5
D_C [Å]	13.1	13.5	13.6	14.2	13.6	14.3
D'_B [Å]	44.2	45.0	45.2	46.4	45.3	46.5
D'_W [Å]	18.5	6.5	21.1	7.0	17.9	3.6
$n_W - n'_W$	18.4	6.3	24.4	7.7	21.5	4.2
n'_W	7.3	6.7	10.3	9.3	11.0	10.3

^{a} Calculated as $2(D_C + D_{H1})$.

The followig figure compares the results for DMPC and EPC. Unsaturation (in the case of EPC) clearly leads to a larger A even if the headgroups are the same. There is also a difference in the fully hydrated water spacing which is an indication that interbilayer interactions (analyzed in Chapter 6) may differ from one lipid to another. The changes in the bilayer structure are minor for the range of dehydration that we used. The number of waters per lipid n_W is suficiently large in order to keep the headgroup hydrated.

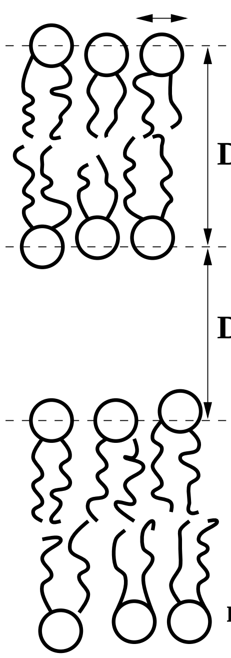

	DMPC		EPC	
	0 atm	27 atm	0 atm	29 atm
A	59.7	57.9	69.4	66.3
	K_A = 136 dyn/cm		K_A = 116 dyn/cm	
D_B	36.9	38.0	36.3	38.0
D_W	25.8	13.5	30.0	15.4
	$K_c = 0.8 \times 10^{-12}$ erg		$K_c = 0.5 \times 10^{-12}$ erg	
n'_W	7.3	6.7	10.3	9.3
$n_W - n'_W$	18.4	6.3	24.4	7.7

Figure 5.6: Comparison between DMPC and EPC structural parameters. The bending modulus K_c is obtained in Chapter 6.

Chapter 6

Determination of Interbilayer Interactions

6.1 Introduction

Having obtained the bilayer structure we now turn to the interbilayer interactions as a function of the interbilayer water spacing. In Section 2.3 we derived the free energy of interaction of bilayers in a multilamellar stack, as a function of the interbilayer water spacing, here denoted by the symbol a for simplicity (see Eq. 2.26),

$$F(a) - F(a = \infty) = V(a) + \left(\frac{k_B T}{2\pi}\right)^2 \frac{1}{K_c \sigma^2}. \tag{6.1}$$

The $V(a)$ term represents the "bare" free energy which is the interaction between non-fluctuating membranes. The second term is the fluctuation free energy F_{fl} (see Eq. 2.25). It involves the bending modulus K_c and the mean square fluctuation in water spacing σ^2. Since $P = -\partial F/\partial a$, it is then natural to use the partitioning of the free energy in Eq. 6.1 to define a bare pressure and a fluctuation pressure,

$$P(a) = P_{bare}(a) + P_{fl}(a). \tag{6.2}$$

The functional form of the fluctuation pressure,

$$P_{fl}(a) = -\left(\frac{k_B T}{2\pi}\right)^2 \frac{1}{K_c} \frac{d\sigma^{-2}}{da} \tag{6.3}$$

can be determined experimentally from the mean square fluctuation in water spacing σ^2, that is obtained from the Caillé order parameter η_1, using the relation
$\sigma^2 = \eta_1 D^2/\pi^2$ (see Eq. 3.7).

6.2 Data

Experimental data for DPPC at 50^oC in the L_α (fluid) phase have been previously reported (Nagle et al., 1996; Zhang et al., 1996) and to this we add data for EPC, DMPC and DOPC, all at 30^oC and all in the L_α phase. By varying the concentration of PVP the osmotic pressure in our samples spanned the range from $P = 0$ to $P = 58$ atmospheres.

Fig. 6.1 shows our osmotic pressure data versus D space for the four lipids. The error in measuring D was about 0.01Å. The greatest error in Fig. 6.1 is in the osmotic pressure due to the difficulty of preparing small samples with precise polymer concentrations. However, the scatter in the $\log P$ data is comparable to data reported in the literature (McIntosh and Simon, 1993; Rand and Parsegian, 1989). We also noticed systematic deviations in $\log P$ in samples prepared on two separate occasions, as indicated for DMPC in Fig. 6.1 by the solid versus open symbols. Uncertainties in $\log P$ for the earlier DMPC and the DPPC data were estimated as 0.3, and as 0.2 for the later DMPC, EPC and DOPC data. Another source of error is revealed in the spacings D_o for fully hydrated samples with no PVP ($P = 0$); the variations in D_o were substantially larger than the measuring error of 0.01Å. The values of D_o are indicated in Fig. 6.1 by arrows. The sum of the squares of the residuals used in fitting theory to the data will include the square residual of D_o weighted by $\Delta_{D_o}^{-2}$.

As discussed in Chapter 3, the Caillé X-ray lineshape parameter η_1 was converted to σ using Eq. 3.7 and the results are shown in Fig. 6.2.

To test the theories of interactions it is necessary to convert D into the interbilayer water spacing a. As explained in Section 2.2 there are different ways of defining the water spacing. The volumetric convention is denoted by D_W in Fig. 1.3 and the steric convention by D'_W. Both can be calculated, once the area per molecule A is known, as described in Section 5.2.3. For the interbilayer separation we employ the definition $a \equiv D'_W$ in Fig. 1.3 that is similar to the one used by McIntosh and Simon (1986a). This choice of convention makes no essential difference for the two interactions that turn out to be exponential. It reduces our estimate of the Hamaker parameter H, but this convention makes only a small difference for the functional form of the van der Waals interaction, since a is comfortably larger than zero.

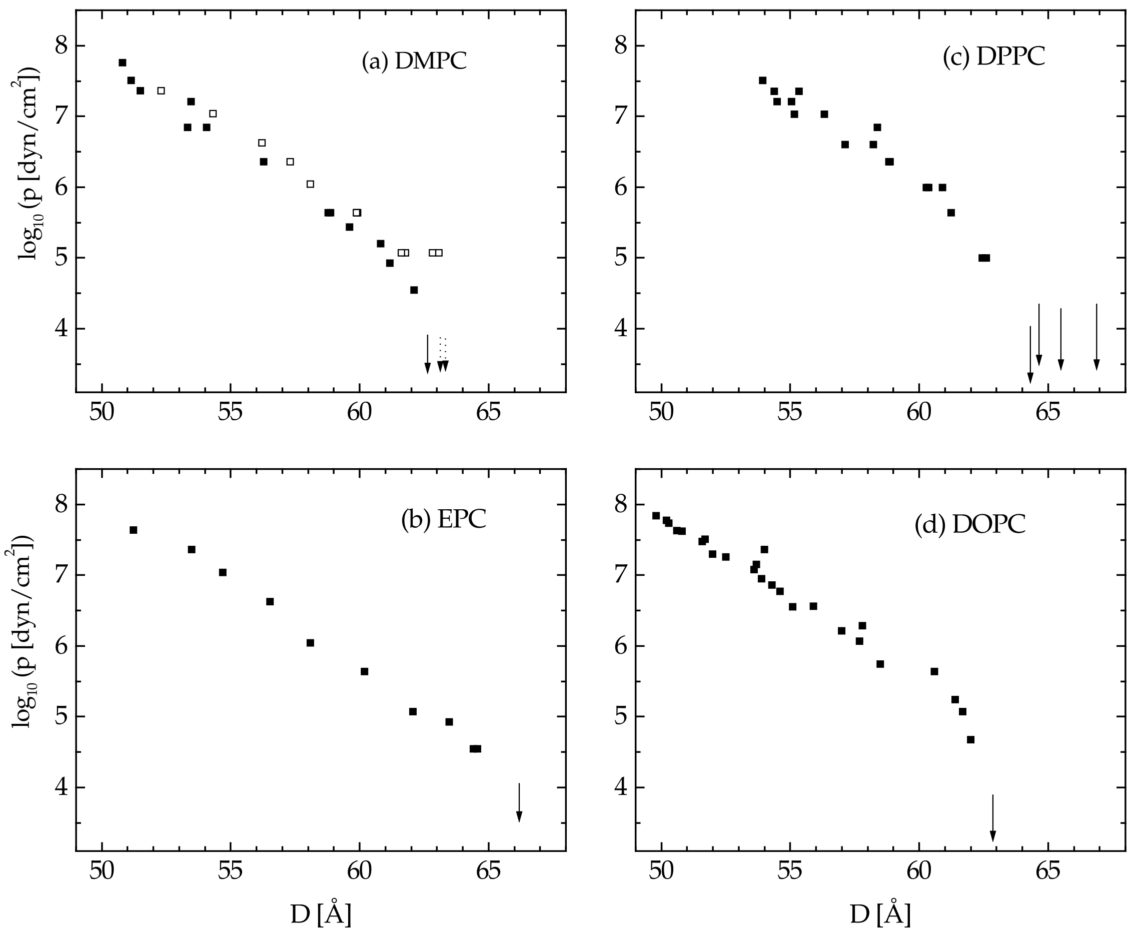

Figure 6.1: Osmotic pressure vs. lamellar D-spacing. In (a) the solid symbols show data for our most recent, most carefully prepared samples and the open symbols show earlier data. The arrows indicate D_o for $P_{osm} = 0$.

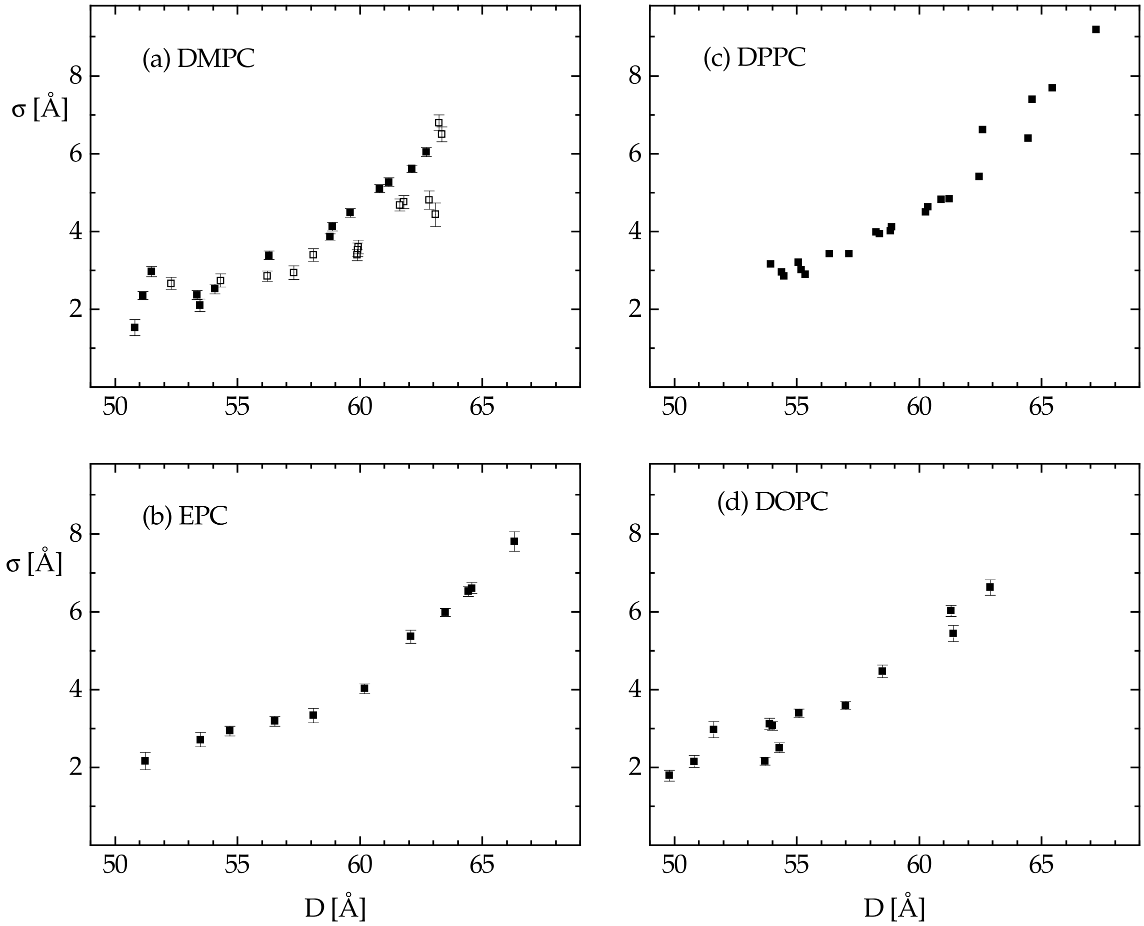

Figure 6.2: Root mean square fluctuation σ vs. D, with same symbols and lipids as in Fig. 6.1.

Table 6.1 at the end of this chapter shows the corresponding water spacing a_o for fully hydrated samples. The large range quoted for DPPC reflects the range of D_o spacings.

6.3 Functional form of F_{fl}

Inspired by Eq. 6.1 and Eq. 2.6 we plot $\log\sigma^{-2}$ versus a in Fig. 6.3. The results for all four lipids are consistent with F_{fl} following an exponential decay which can be parameterized as

$$F_{fl} = \left(\frac{k_B T}{2\pi}\right)^2 \frac{1}{K_c}\, A_{fl}\, e^{-a/\lambda_{fl}}. \tag{6.4}$$

The decay length λ_{fl} and the amplitude A_{fl} obtained from the plots of $\log\sigma^{-2}$ versus a in Fig. 6.3 are presented in Table 6.1. We note that if the compressibility correction to a had not been made (see Section 5.2.2), then the plots are also consistent with an exponential decay of F_{fl}, but with decay lengths about 0.2Å shorter. Both sets of decay lengths are systematically greater than predicted by the soft confinement theory presented in Eq. 2.6, as will become apparent when values of the hydration force decay constant λ are obtained.

The dashed curves in Fig. 6.3 show the prediction for hard confinement as embodied by Eq. 2.5; they simply use the basic hard confinement relation,

$$(\sigma/a)^2 = \mu \tag{6.5}$$

where μ is a constant. The value of μ has been given as 1/6 (Helfrich, 1978), 0.183 (Podgornik and Parsegian, 1992) and 1/5 (Janke and Kleinert, 1986); the value 1/6 is used in Fig. 6.3. Comparing to the data shows first that hard confinement predicts a significant curvature in Fig. 6.3 that is not observed; in other words, the functional form of the undulation repulsion is incorrect. Second, the dashed curve lies below the data; raising it would require smaller values of μ of order 0.05, but these values would also have to vary with a. From this comparison we conclude that a theory of soft confinement, such as the one given by Eq. 2.6, is required for the range of a in our data.

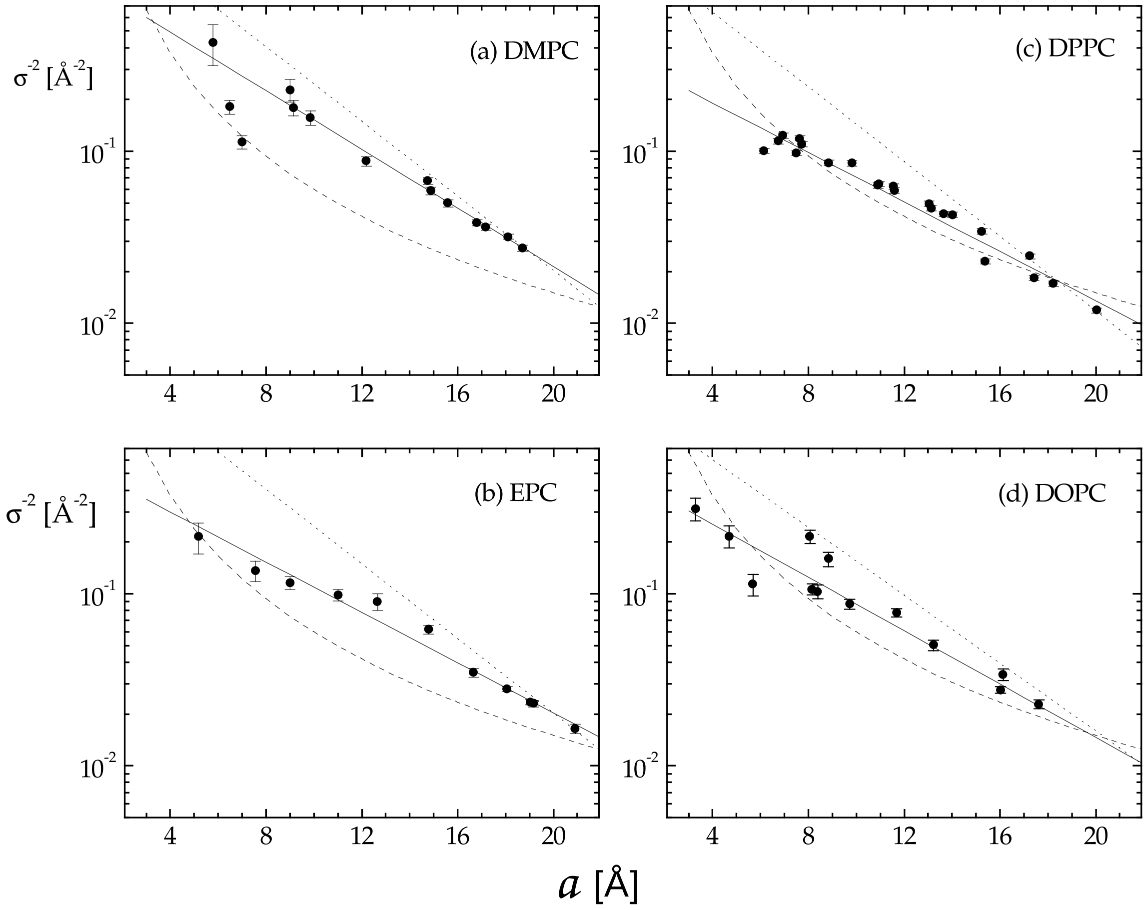

Figure 6.3: Log σ^{-2} vs. water spacing a. The solid lines show exponential fits. The dashed lines show the hard confinement prediction, Eq. 2.5, and the dotted lines show the slope for the soft-confinement prediction, Eq. 2.6.

6.4 Decomposition of P_{osm} data

The exponential decay in the fluctuation free energy implies an exponential decay of the fluctuation pressure

$$P_{fl} \sim \exp^{-a/\lambda_{fl}}, \tag{6.6}$$

with decay length λ_{fl}. If we know K_c, then Eq. 6.3 can be used to determine P_{fl}. Unfortunately, literature values of K_c are either absent for some lipids or are uncertain by factors of 4 for other lipids, so we first tried using K_c as a fitting parameter along with the other parameters λ, P_h and H in Eq. 2.3, using a routine non-linear least squares program. For EPC the resulting parameters for this unconstrained fit are shown in line 1 of Table 6.2.

Fig. 6.4a shows the fit to the $\log P$ data and also the decomposition into the three component pressures. However, by holding K_c fixed at other values, quite reasonable fits to the $\log P$ data can also be obtained as shown in Fig. 6.4b. The results for the corresponding values of the other parameters, while holding $K_c = 1 \cdot 10^{-12}$ erg and $2 \cdot 10^{-12}$erg, are shown in lines 2 and 3, respectively, in Table 6.2.

Fits for DMPC, DPPC and DOPC are shown in Figs. 6.5. Fitting results for several fixed values of K_c are shown in Table 6.2. DPPC is more complicated because there is a wider range of a_o and the earlier data have larger uncertainties in P; we therefore give results for the two extreme values of a_o.

It is clear from the previous paragraph that additional information is required to determine the fitting parameters uniquely. One possibility is to hypothesize that the values of some of the parameters might vary little from lipid to lipid. For example, if the hydration pressure depends primarily upon water, then λ should be nearly the same for the four lipids. Also, the Hamaker parameter H might reasonably be expected to be nearly the same; the thickness dependence of the different bilayers is already accounted for in first approximation by the form of Eq. 2.3 and the relative proportion of head to tail does not vary much for these four lipids. These considerations disfavor the first two fits for DPPC listed in Table 6.2 which were driven by the smallest estimate of a_o. From the last two fits we then conclude that λ is nearly 2.0Å and P_h is about $1 \cdot 10^9$ erg/cm^3. These values of λ are only about 0.1Å smaller than given by Rand and Parsegian (1989). The robustness of these values for λ and P_h follows from the fact that they are primarily determined by the high P data where the other two pressures are small as shown in Figs. 6.4-6.5. Because we make a compressibility correction, our λ are larger than those given by McIntosh and Simon (1993); if we did not make this correction our λ would be of order 1.8Å.

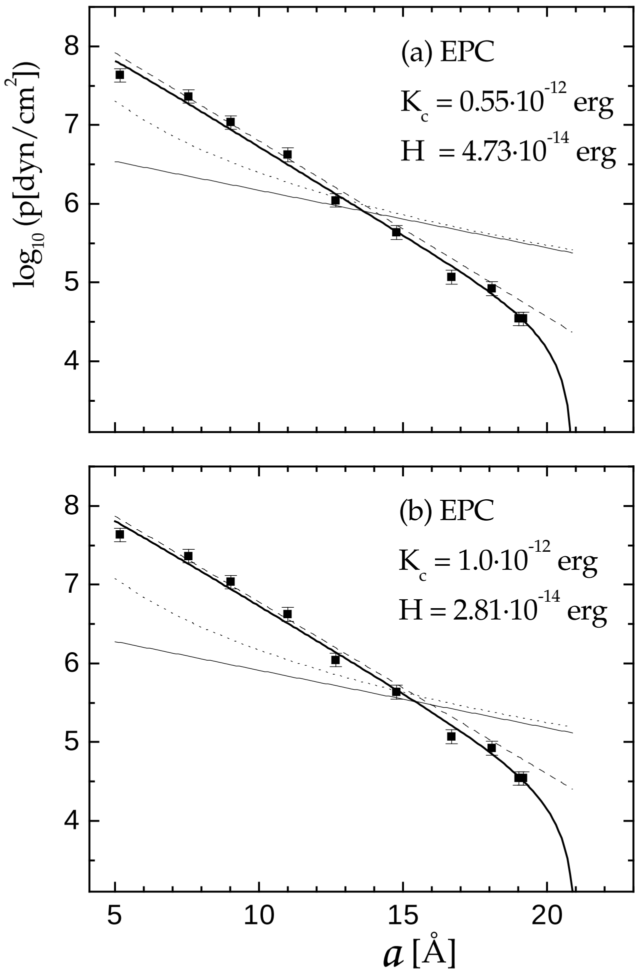

Figure 6.4: The curved solid line shows the fit to $\log(P_{osm})$ versus a for EPC for the two values of K_c shown in (a) and (b). The straight solid line in each panel shows the fluctuation pressure, the straight dashed line shows the hydration pressure and the curved dotted line shows the van der Waals pressure. Parameter values are given in Table 6.2.

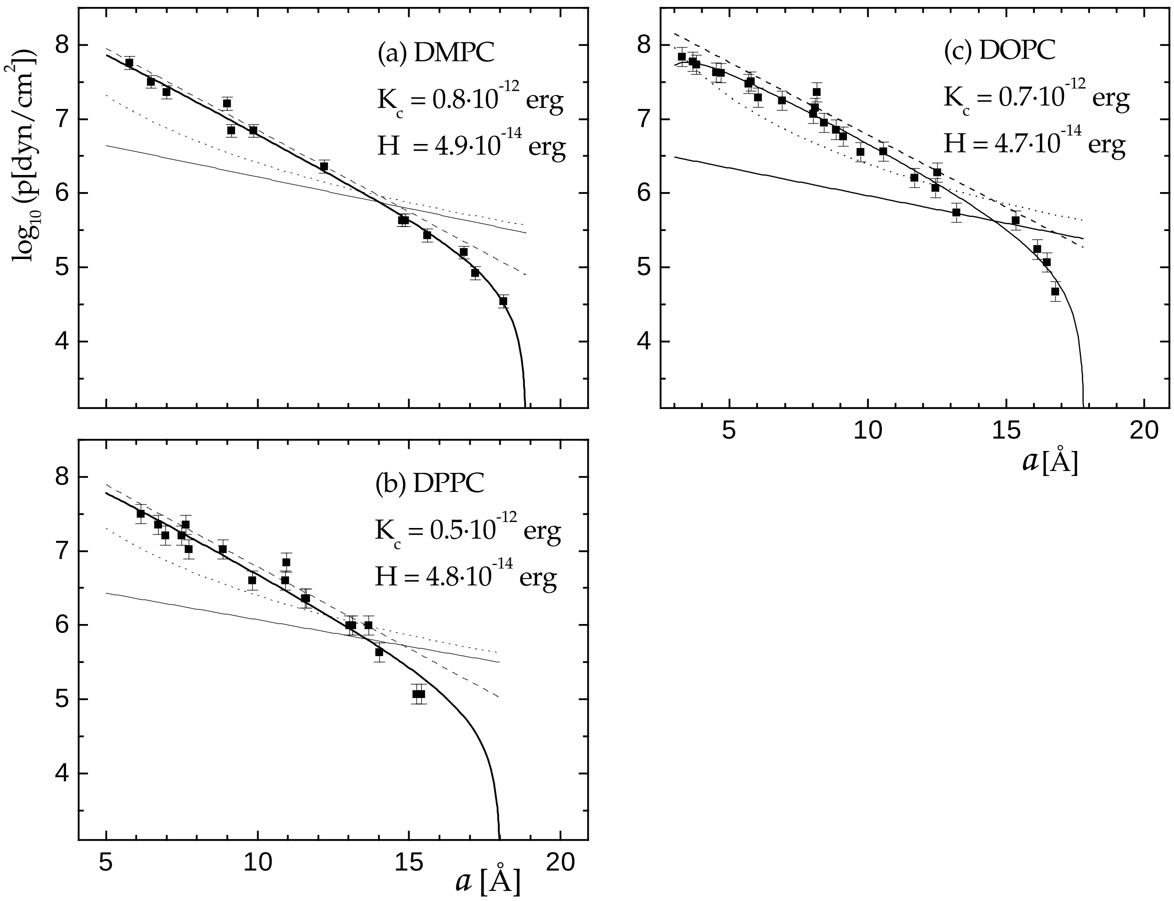

Figure 6.5: As in Fig. 6.4 except that panel (a) is for DMPC, panel (b) for DPPC and panel (c) for DOPC.

Figs. 6.4-6.5 show that the magnitude of the van der Waals pressure and the fluctuation pressure follow each other as K_c is varied, so the value H is no better determined than the value of K_c. There is, however, another criterion that can be used to establish preferences. Let us suppose that the hydration pressure and the van der Waals pressure are the same in the gel phase as in the L_α phase, and that the fluctuation pressure is negligible because gel phase bilayers should be stiffer with larger K_c. Then, a in the gel phase would be the value of a at which the hydration pressure and the magnitude of the van der Waals pressure become equal; let us call this a_o^*. The difference $\Delta a_o = a_o - a_o^*$ is given in Table 6.2 for the various fits. The experimental difference in a_o between L_α and gel phase DPPC is 9Å (Nagle et al., 1996). This favors the larger values of Δa_o in the last column of Table 6.2, i.e., smaller values of K_c and larger values of H. However, when we consider even smaller values of K_c than given in Table 6.2, the fit to the $\log P$ data deteriorates rapidly. The fact that the fitted values of Δa_o are smaller than 9Å may, of course, reflect different values of some of the parameters for the gel phase. A similar criterion comes from oriented multilayers on solid substrates. Our most fully hydrated samples of DMPC (Tristram-Nagle et al., 1998a) only have D spacings of 52Å. Current theory (Podgornik and Parsegian, 1997) for these much smaller D spacings is that the substrate suppresses the fluctuations and this eliminates the fluctuational pressure. Since this should not change the other interactions or the bilayer thickness, one would have $a_o^* = 52\text{Å} - 44\text{Å} = 8\text{Å}$, which would give $\Delta a_o = 11\text{Å}$. One concern in the precise numerical value obtained from this criterion is that it is very hard to achieve 100% relative humidity for samples oriented on solid substrates; achieving higher humidity would, of course, reduce Δa_o.

Another criterion that one might use across the four lipids is to suppose that K_c might be larger for larger bilayer thickness. However, this criterion is weakened because EPC and DOPC have unsaturated bonds that make the hydrocarbon chains more disordered than with saturated chains and the DPPC data were taken at higher temperature where the bilayer should be more flexible. Indeed, data taken at different temperatures (see Section 6.6) show that σ increases with temperature. We therefore ignore this criterion in favor of the others above.

Since our best fit to EPC gives $K_c = 0.55 \cdot 10^{-12}$erg which is similar to the value obtained by direct measurement (Faucon et al., 1989), and gives $H = 4.73 \cdot 10^{-14}$erg in agreement with the result of Parsegian (1993), we will choose line 1 in Table 6.2.

Assuming that the corresponding value of H should be nearly the same for all four lipids leads us to suggest that K_c is about $0.50 \cdot 10^{-12}$erg for DPPC at 50^{o}C, $0.70 \cdot 10^{-12}$erg for DOPC at 30^{o}C and $0.80 \cdot 10^{-12}$erg for DMPC at 30^{o}C. We note that the latter value is closer to the most recently measured value of K_c for DMPC at 25^{o}C than to the value measured at 30^{o}C (Meleard et al., 1997).

6.5 B moduli

In this section we address the rather confusing issue of various compression moduli that can be defined. The modulus B that enters in the compression term of Eq. 2.1 is related to σ by Eq. 2.24. It is important to appreciate that this B is a phenomenological input parameter; as such, it should not be expected to be equal to the thermodynamic compression modulus B_T. Indeed, imposing such an equality would ensure that the bending term in Eq. 2.1 would have no effect in determining B_T. There are several ways that one can define the thermodynamic bulk modulus. The most straightforward is as $-D(\partial P/\partial D)_T$. It is more convenient, however, to consider $-D(\partial P/\partial a)_T$. Due to the compressibility of the bilayer these two ways are not the same, but the difference is less than 6% at our highest osmotic pressure.

Using either definition, we must also divide by D as was done in converting B_3 in Eq. 2.2 to B in Eq. 2.1. We therefore define the thermodynamic modulus as

$$B_T = -\frac{dP}{da}. \tag{6.7}$$

It is also useful to define a bare modulus

$$B_b = \frac{d^2V(a)}{da^2} \tag{6.8}$$

and a fluctuation modulus

$$B_{fl} = \frac{d^2F_{fl}(a)}{da^2} \tag{6.9}$$

All derivatives are calculated at constant temperature. From Eq. 6.2 it then follows that

$$B_T = B_{fl} + B_b. \tag{6.10}$$

Fig. 6.6 shows these four moduli obtained from our best fit to EPC. The bare modulus B_b is nearly equal to B_T for high P and small a because B_{fl} is relatively small. The relations change dramatically for larger a because B_b goes negative as a exceeds 17Å; this is just a different statement of the fact that the fluctuation pressure swells a beyond a_o^*.

Most importantly, Fig. 6.6 emphasizes our assertion above that there is no general simple relation between B and any of the other three moduli.

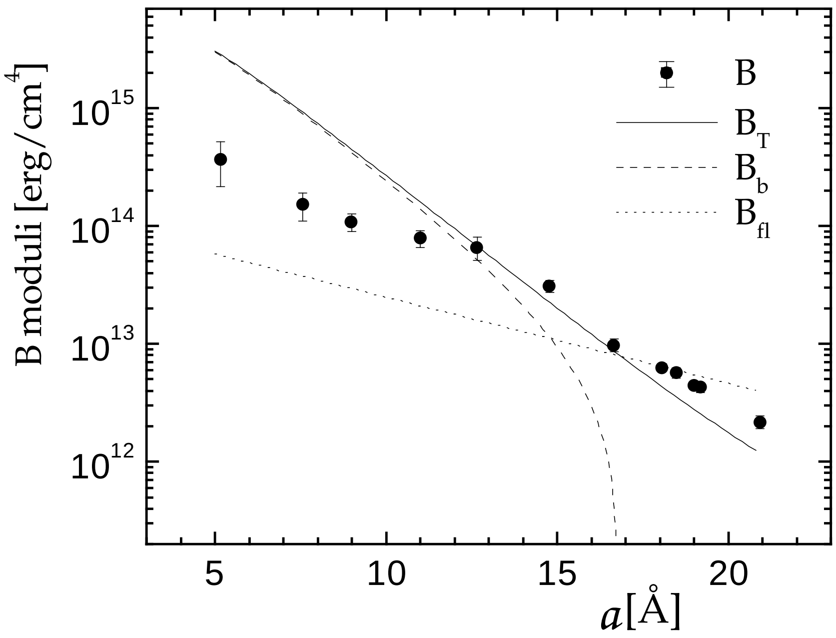

Figure 6.6: Log of various moduli as a function of a. Parametric modulus B (solid circles from σ data); thermodynamic modulus B_T (solid curve); bare modulus B_b (dashed curve - when positive) and fluctuation modulus B_{fl} (dotted line).

6.6 Temperature dependence

In a study of EPC bilayers, Simon et al. (1995) advanced the hypothesis that fluctuations increase with increasing T. With our high resolution X-ray method we can easily test this by measuring the Caillé order parameter η_1. Fig. 6.7 shows X-ray scattering data that clearly indicate an increase of the peak tail with temperature. We monitored the fully hydrated EPC samples with focus on the fluctuations rather than on electron density profiles and bilayer thickness, which were studied for EPC by Simon et al. (1995).

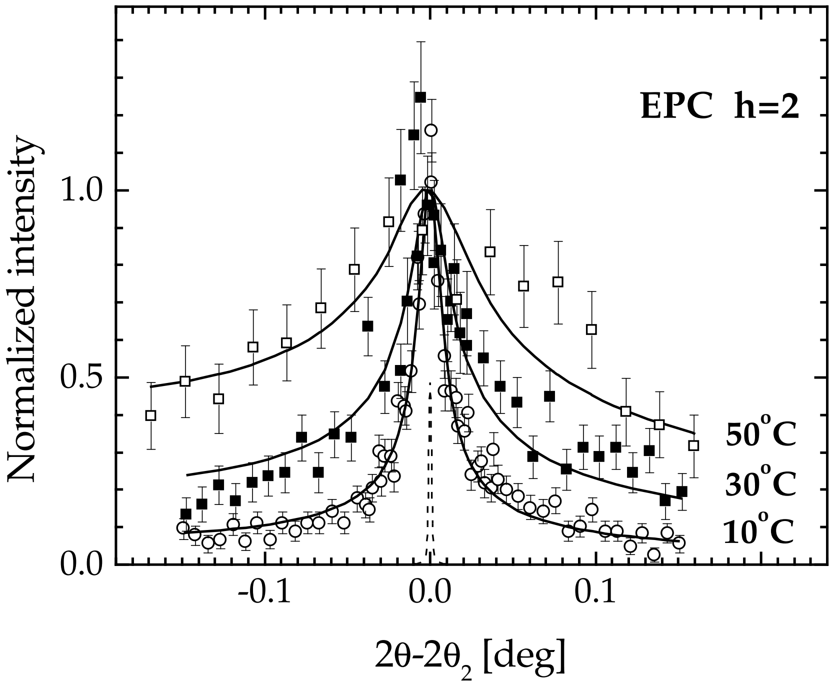

Figure 6.7: Comparison of $h = 2$ data for EPC at different temperatures. The solid lines show the fits, which also fit the first order data (not shown), with $\eta_1 = 0.088$, 0.137, 0.175 for $T = 10^o$C (open circles), $T = 30^o$C (solid squares) and $T = 50^o$C (open squares), respectively. The dashed peak shows the instrumental resolution function.

With the η_1 values obtained from the MCT fits we then calculate the mean-square fluctuation σ^2 using Eq. 3.7. In Fig. 6.8 we plot the inverse mean square water space fluctuation, σ^{-2}, on a logarithmic scale versus water spacing a for samples at $P = 0$ for $T = 10, 18, 30$ and 50^oC. For $T = 30^o$C we obtained a at $P = 0$ as explained in Sec. 5.2.3. For other temperatures we used the T dependence of the bilayer thickness of Simon et al. (1995), which was about 0.084Å/^{o}C to estimate D'_B which was then subtracted from our D to obtain a. The temperature dependence of σ^{-2} in Fig. 6.8 clearly shows that interbilayer fluctuations increase with increasing T.

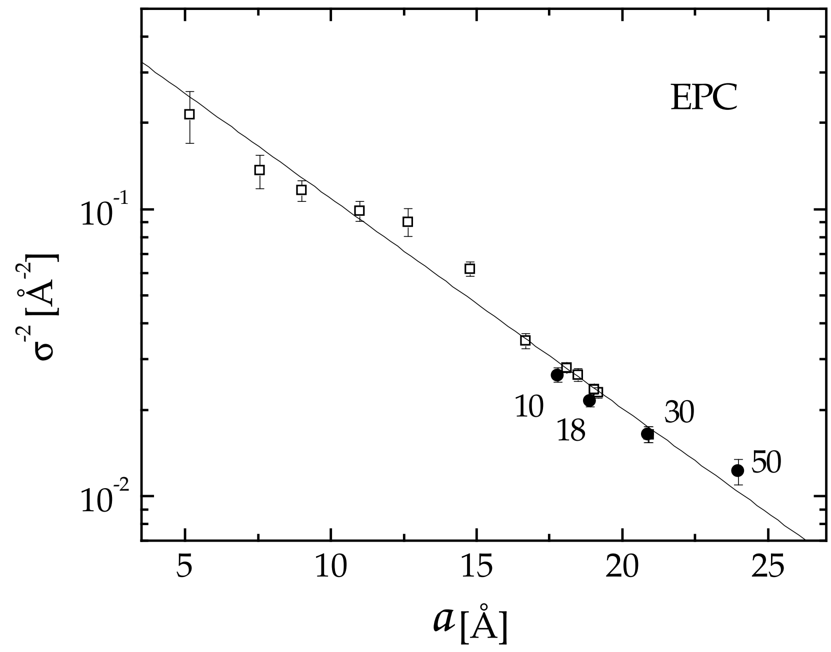

Figure 6.8: Plot of σ^{-2} vs. a for EPC samples under various osmotic pressures at $T = 30^o$C (open symbols) and for fully hydrated samples at $T = 10, 18, 30$ and 50^oC (solid symbols).

Fig. 6.8 also shows σ^{-2} for other samples at $T = 30^o$C subject to various osmotic pressures P. The motivation for plotting σ^{-2} on a logarithmic scale in Fig. 6.8 comes from our result for the fluctuational contribution to the free energy given in Eq. 6.1. Surprisingly, all σ^2 data appear to fit on the same line independently of temperature. Therefore the fluctuation free energy, can be modeled by Eq. 6.4 with temperature independent parameters A_{fl} and λ_{fl}.

Minimizing with respect to a the total free energy F, then gives the water spacing a_o when $P = 0$. Results of Simon et al. (1995) indicated only very small T dependences of the parameters P_h, λ and H that, within the quoted errors could have been constant. The estimates given for the Hamaker parameter H suggested about 10% decrease from 5^{o}C to 50^{o}C, but theory suggests that H should increase (Parsegian and Ninham, 1971). Also, the values of $\lambda \approx 1.1$Å given by Simon et al. (1995) are much smaller than other values (Rand and Parsegian, 1989), so we have used our values of $\lambda = 1.94$Å, $P_h = 1.07 \cdot 10^9$ dyn/cm^3 and $H = 4.73 \cdot 10^{-14}$ erg as constants at all T. Then, we have found the value of K_c for which the total free energy F has the minimum at values of a_o shown with solid symbols in Fig. 6.8. These results for K_c are presented in the second column of Table 6.3. The third column of Table 6.3 also shows the values of K_c (denoted by $\hat{K_c}$) that are predicted if $K_c = 0.55 \cdot 10^{12}$ ergs at $T = 30^o$C and if K_c is proportional to the square of the hydrocarbon chain thickness, which is a likely dependence for K_c (Simon et al., 1995).

6.7 Discussion

Our σ data, presented in Section 6.2 open a second window on interbilayer interactions, as we have shown theoretically in Section 2.4, expecially regarding the fluctuation pressure, for which our results are shown in Section 6.3. Our data show that a theory of soft confinement is definitely required for biological lipid bilayers, in contrast to some soft condensed matter systems (Safinya et al., 1989) that were shown to obey Helfrich's theory of hard confinement. While the data support an exponentially decaying form for the fluctuation pressure, they have a decay length λ_{fl} that is greater than twice the decay length λ of the hydration force predicted by the most recent theory of soft confinement (Podgornik and Parsegian, 1992).

Using this extended probe of the fluctuation force, we have then attempted to decompose the usual osmotic pressure data into component pressures without using additional information, such as the factor of K_c^{-1} in the fluctuation pressure. Ironically, the interaction that is the least well understood conceptually, the hydration pressure, is the one that can be best determined. In this regard, it is worth noting that other researchers have gone to much higher osmotic pressures (Rand and Parsegian, 1989; McIntosh and Simon, 1993). Because the hydration pressure is already well determined with the range of pressures we use, we have concentrated instead on obtaining more data in the lower pressure range near full hydration where the other interactions play larger roles. One conclusion of our study is that the ability to fit the data, even with the new constraint on the functional form of P_{fl}, indicates that the functional forms of the hydration pressure (Eq. 2.4) and the van der Waals interaction in Eq. 2.3 remain acceptable, though perhaps not proven.

Furthermore, as we show in Section 6.4, if either K_c or the Hamaker parameter H can be obtained from other experiments, then the remaining parameters can be extracted. It is indeed encouraging that choosing the experimental value of K_c from Faucon et al. (1989) and Meleard et al. (1997), returns a reasonable value of H (Parsegian, 1993) and *vice versa*. However, the value of $K_c = 0.56 \cdot 10^{-12}$ erg from Evans and Rawicz (1990), would favor line 1 in Table 6.2 for DMPC. Nevertheless, we regard this study as being a stepping stone to further study rather than as providing final answers to interbilayer interactions.

Our data were mostly for $T = 30^o$C, but we explored the issue of how fluctuations depend upon T for EPC by measuring the Caillé fluctuation parameter η_1. Our data directly confirm the hypothesis of Simon et al. (1995) that fluctuations increase with increasing T. Simon et al. (1995) also suggested that this is due to a decrease in bending modulus K_c. Assuming, following Simon et al. (1995), that the other interactions, van der Waals and hydration force, are independent of T, our data are consistent with a small decrease in K_c. However, we note that there is also a factor of T^2 in the fluctuation pressure that plays a non-negligible role in increasing the fluctuations. Although this factor is usually thought to be negligible, it can cause a substantial increase in water spacing a at full hydration ($P = 0$) because the minimum in the bare interbilayer potential is so shallow. As shown in Table 6.3 the T dependence of K_c is a little less than if K_c scaled as the square of the hydrocarbon chain thickness as measured by Simon et al. (1995). Therefore, our direct data for the T dependence of the fluctuations are basically consistent with the overall picture of T dependence of interbilayer interactions proposed by Simon et al. (1995).

Table 6.1: Parameters obtained from X-ray data. The units are Å for D'_B, a_o, and λ_{fl}, and $\mathring{A}^{-2}$ for A_{fl} .

Lipid	D'_B	a_o	A_{fl}	λ_{fl}
DMPC	44.0	18.7	1.08 ± 0.13	5.1 ± 0.2
EPC	45.4	20.9	0.59 ± 0.08	5.9 ± 0.3
DPPC	47.2	20.0/19.0	0.37 ± 0.03	6.0 ± 0.3
DOPC	45.3	17.9	0.47 ± 0.08	5.8 ± 0.5

Table 6.2: Parameter values for several fits to $\log P$ data. The units are $K_c\,[10^{-12}\text{erg}]$; $P_h\,[10^9\text{erg/cm}^3]$; $H\,[10^{-14}\text{erg}]$ and λ, a_o and Δa_o are in Å.

Lipid	K_c	P_h	λ	H	a_o^{fit}	Δa_o
EPC	0.55	1.07	1.94	4.73	20.9	7.4
	1.00	0.91	1.99	2.81	21.0	5.6
	2.00	0.81	2.03	1.65	21.0	3.7
DMPC	0.50	1.32	1.91	7.13	18.8	6.3
	0.80	1.13	1.97	4.91	18.8	5.0
	1.30	1.01	2.01	3.50	18.9	3.7
DPPC	0.50	0.63	2.36	9.19	16.0	2.3
	1.00	0.58	2.39	7.41	16.0	1.3
	0.50	0.99	1.97	4.78	18.0	4.5
	1.00	0.92	1.97	2.87	18.1	3.1
DOPC	0.40	0.68	2.14	6.51	17.9	4.8
	0.70	0.55	2.22	4.72	17.8	3.3
	1.00	0.50	2.26	4.02	17.8	2.5

Table 6.3: Temperature dependence of bending modulus K_c for EPC. Units of K_c are 10^{-12} erg. K_c was obtained from fitting the water spacing at $P = 0$, and $\hat{K}_c$ was obtained assuming quadratic dependence upon hydrocarbon chain thickness.

T [^{o}C]	K_c	$\hat{K}_c$
10	0.61	0.62
18	0.57	0.59
30	0.55	0.55
50	0.53	0.50

Chapter 7

Concluding Remarks

One accomplishment of this work is the elaboration of a consistent interpretation of $P(D_W)$ and $\sigma(D_W)$ data. This required a careful consideration of the de Gennes - Caillé model for smectic systems. The model involves the phenomenological fluctuation parameters K_c and $B(D_W)$. While the bending modulus K_c is well defined, the compression parameter $B(D_W)$ is a more complex quantity. It depends on the water spacing D_W and therefore its functional form needs to be specified. Evidently, there must be a connection between $B(D_W)$ and the bare interaction $V(D_W)$, which is the interaction between non-fluctuating membranes. However, due to the complexity of the membrane system, the two are connected in a non-trivial way. Direct theoretical approaches had little success. In Chapter 3 we show that by measuring the Caillé parameter η_1, we essentially measure the compression parameter $B(D_W)$. Therefore we were able to subtract the fluctuation contribution from the osmotic pressure curves and obtain the bare interaction $V(D_W)$. We have then shown (Chapter 6) that indeed, the bare interaction can be represented as a sum of a van der Waals attraction term and an exponentially decaying repulsive term. The interaction parameters that we obtain are in agreement with other measurements. These other measurements either suppress fluctuations, as in the measurement of the van der Waals interaction between bilayers on mica surfaces, or lack interbilayer interactions, as in the optical measurement of the bending modulus K_c of large unilamellar vesicles. The procedure described in this work allows for a simultaneous determination of the interbilayer interactions together with the determination of the bilayer structure.

Another accomplisment is the determination of the structural parameters, which form a basis for the understanding of complex lipid mixtures in the biomembrane systems. By varying the lipid composition, the biomembranes can adjust their physical properties, especially the fluidity, to permit the membrane proteins to function in their optimum regime. Our analysis of diffraction data revealed the dependence of the structural parameters on the chemical composition of the lipid bilayer. In particular, the central quantity A (area per lipid) is shown to be very sensitive to the acyl chain composition even for the same lipid headgroup. Unsaturation, as in the case of fluid DOPC, leads to a 20% larger A relative to fluid DMPC at the same temperature.

By using the osmotic stress technique we have probed the elasticity of lipid bilayers. The lipid bilayers respond to water loss by a slight decrease in the area per molecule, that accompanies the major effect of D_W reduction. However, the bilayer structure remains stable even for our most dehydrated samples. As summarized in Table 5.2 this level of osmotic stress does not alter the headgroup solvation (n'_W) significantly.

Accurate measurements of structural and interaction parameters provide a reliable experimental basis for computer simulations of lipid membranes. With precise values for these parameters, simulators can test their potential functions and focus their effort to obtain information that is experimentally inaccessible. Some suggestions have been indicated in this work, whenever less than obvious assumptions have been employed (e.g. page 49). Therefore, the results of this work are subject to revisions when feedback is available. We made, nevertheless, significant progress toward a more accurate description of lipid membranes.

Chapter 8

Publications

1. Fluid phase structure of EPC and DMPC bilayers.
Petrache H. I., S. Tristram-Nagle, and J. F. Nagle.
Chemistry and Physics of Lipids, in press.

2. Structure and interactions of fully hydrated dioleoylphosphatidylcholine bilayers.
Tristram-Nagle, S., H. I. Petrache, and J. F. Nagle.
Biophysical Journal 75; August 1998; pp. 917-925.

3. Interbilayer interactions from high resolution X-ray scattering.
Petrache, H. I., N. Gouliaev, S. Tristram-Nagle, R. Zhang, R. M. Suter, and J. F. Nagle.
Physical Review E 57; June 1998; pp. 7014-7024

4. DMSO produces a new subgel phase in DPPC: DSC and X-ray diffraction study.
Tristram-Nagle, S., T. Moore , H. I. Petrache, and J. F. Nagle.
Biochimica et Biophysica Acta 1369; 1998; pp. 19-33.

5. Effect of substrate roughness on D spacing supports theoretical resolution of vapor pressure paradox.
Tristram-Nagle, S., H. I. Petrache, R. M. Suter, and J. F. Nagle.
Biophysical Journal 74; March 1998; pp. 1421-1427.

6. Determination of component volumes of lipid bilayers from simulations.
Petrache, H. I., S. E. Feller, and J. F. Nagle.
Biophysical Journal 72; May 1997; pp. 2237-2242.

7. X-ray structure determination of fully hydrated L_α phase dipalmitoylphosphatidylcholine bilayers.
Nagle, J. F., R. Zhang, S. Tristram-Nagle, W.-J. Sun, H. I. Petrache, and R. M. Suter.
Biophysical Journal 70; March 1996; pp. 1419-1431.

In preparation:

1. Analysis of simulated NMR order parameters for lipid bilayers.
Petrache H. I., K. Tu, and J. F. Nagle.

2. Multiple mechanisms for critical behavior in the biologically relevant phase of lecithin bilayers.
Nagle J. F., H. I. Petrache, N. Gouliaev, S. Tristram-Nagle, R. M. Suter, and K. Gawrisch.

Appendix A

Continuum vs. discrete descriptions

A.1 The models

In this appendix we will focus on the fluctuational part of the interactions.

Discrete Hamiltonian. This is the description used in the present work.

$$\mathcal{H}_d = \int dx \int dy \sum_{n=0}^{N-1} \left[\frac{1}{2} K_c \left(\frac{\partial^2 u_n}{\partial x^2} + \frac{\partial^2 u_n}{\partial y^2} \right)^2 + \frac{1}{2} B \left(u_{n+1} - u_n \right)^2 \right] \quad \text{(A.1)}$$

B has units of erg/cm^4. The second term of the Hamiltonian assumes that there is a compression energy that is a harmonic function of the local interbilayer separation. The expectation value of the compression energy per unit area of one bilayer is

$$\langle \mathcal{H}_d^{com} \rangle = \frac{1}{2} B \sigma_d^2, \quad \text{(A.2)}$$

where

$$\sigma_d^2 \equiv \langle (u_{n+1} - u_n)^2 \rangle = \frac{4}{\pi} \frac{k_B T}{8} \frac{1}{\sqrt{K_c B}}. \quad \text{(A.3)}$$

The calculation of σ_d^2 has been done using the Fourier expansion:

$$u(x, y, n) = \sum_{Q_x, Q_y, Q_z} U(Q_x, Q_y, Q_z) e^{i\vec{Q}\cdot\vec{R}} \quad \text{(A.4)}$$

with $\vec{R} = \vec{r} + nD\hat{z}$ and the vectors $\vec{Q}$ taking values in the first Brillouin zone defined by the in-plane molecular size a for Q_x, Q_y and by the membrane spacing D for Q_z:

$$\frac{2\pi}{L} < |Q_z| < \frac{\pi}{D} \ . \quad \text{(A.5)}$$

Continuum Hamiltonian. If only long wavelength fluctuations are allowed, then the system can be treated as a continuum. In particular, the compression term can be written as a derivative:

$$\mathcal{H}_c = \int dx \int dy \int dz \left[\frac{1}{2} K \left(\frac{\partial^2 u}{\partial x^2} + \frac{\partial^2 u}{\partial y^2} \right)^2 + \frac{1}{2} B_3 \left(\frac{\partial u}{\partial z} \right)^2 \right] \tag{A.6}$$

B_3 has units of erg/cm^3. This is how the Hamiltonian is introduced by de Gennes (1974). Long wavelength fluctuation means that the fluctuations of interest occur at a scale Λ, that is much larger than the interbilayer separation D,

$$\Lambda \equiv \frac{\pi}{Q_{zmax}} \gg D, \tag{A.7}$$

This (unknown) scale introduces a cutoff for the Q_z vectors,

$$Q_z \leq \frac{\pi}{\Lambda} \ll \frac{\pi}{D}. \tag{A.8}$$

The expectation value of the compression energy per unit volume is

$$\langle \mathcal{H}_c^{com} \rangle = \frac{1}{2} B_3 \, \langle \left(\frac{\partial u}{\partial z} \right)^2 \rangle, \tag{A.9}$$

therefore the appropriate definition of the interbilayer spacing mean-square fluctuation is (Evans and Parsegian, 1986),

$$\sigma_c^2 = D^2 \langle \left(\frac{\partial u}{\partial z} \right)^2 \rangle. \tag{A.10}$$

Comparing with Eq. A.2, the correspondence between B_3 and B is simply

$$B_3 = DB. \tag{A.11}$$

The calculation of σ_c^2 depends on the cutoff Λ. If we let $\Lambda = \pi/D$ we obtain

$$\sigma_c^2 = \frac{\pi}{2} \frac{k_B T}{8} \frac{1}{\sqrt{K_c B}}. \tag{A.12}$$

This gives the right dependence of σ_c^2 on the interaction parameters K_c and B but the numerical factor is not reliable. The advantage of the continuum Hamiltonian is that it allows for much simpler calculations of quantities dominated by the *large scale* fluctuations of the system (and one should only use the continuum Hamiltonian to describe the properties of the system at large scale). Most of the calculation can be done analytically and the results can be put in a simple form without further approximations. For example, the asymptotic form ($z \to \infty$) of the interbilayer correlation function

$$\Delta_c^2(z) \equiv \langle (u(0,0,z) - u(0,0,0))^2 \rangle \tag{A.13}$$

can be easily obtained by ignoring the cutoff in Q_z (Caillé (1972) takes $Q_{zmax} \to \infty$).

MCT (Zhang et al., 1994) puts a cutoff at the edge of the first Brillouin zone (Eq.A.5),

$$Q_{zmax} = \frac{\pi}{D}. \tag{A.14}$$

in order to avoid divergencies.

However, irrespective of the value of the cutoff, a theory built on the Hamiltonian introduced by Eq. A.6 is a continuum theory. The phenomenological parameter B_3 is in principle a function of the cutoff Λ. One can integrate over high modes in order to renormalize B_3. The advantage of the discrete Hamiltonian is that the problem of the cutoff no longer exists and B is well defined.

The two Hamiltonians, discrete and continuum, describe the long wavelength properties of the system equally well. This can be easily seen by comparing the energy per mode in each case. Expressing everything in terms of K_c and B we have, for the discrete case (d),

$$h_d = K_c Q_r^4 + D^2 B \frac{4}{D^2} \sin^2\left(\frac{Q_z D}{2}\right), \tag{A.15}$$

and for the continuum (c),

$$h_c = K_c Q_r^4 + D^2 B Q_z^2. \tag{A.16}$$

Eq. A.16 is the long wavelength limit ($Q_z D/2 \ll \pi/2$) of Eq. A.15. Consequently, the correlation function at $z \gg D$ is practically the same, while at $z = D$ they differ by about 25%. This difference does not affect the X-ray line shape, as we will show next.

A.2 The X-ray correlation function

The interbilayer correlation function,

$$\Delta^2(k) = \langle (u(x,y,z) - u(x,y,0))^2 \rangle, \tag{A.17}$$

for a stack of N membranes with spacing D and size $L_z = ND$ has been calculated using periodic boundary conditions. The results for the discrete (d) and the continuum

(c) are

$$\Delta_d^2(k) = \frac{k_B T}{4\pi}\frac{1}{\sqrt{K_c B}}\Sigma_d(k) \tag{A.18}$$

$$\Delta_c^2(k) = \frac{k_B T}{4\pi}\frac{1}{\sqrt{K_c B}}\Sigma_c(k) \tag{A.19}$$

with

$$\Sigma_d(N,k) = \sum_{j=1}^{N/2} \frac{1-\cos\frac{2\pi jk}{N}}{\frac{N}{\pi}\sin\frac{\pi j}{N}} \tag{A.20}$$

$$\Sigma_c(N,k) = \sum_{j=1}^{N/2} \frac{1-\cos\frac{2\pi jk}{N}}{j}. \tag{A.21}$$

The two functions Σ_d and Σ_c, calculated in the limit $N \to \infty$ are compared in Fig. A.1. They both have the same logarithmic dependence with the distance, but they differ by a constant everywhere. The continuum gives (Caillé, 1972; Zhang et al., 1994)

$$\Sigma_c(k) \approx \gamma + \ln(\pi k), \tag{A.22}$$

where $\gamma \approx 0.577$ is the Euler constant, while the discrete model gives

$$\Sigma_c(k) \approx \frac{3}{2}\gamma + \ln(\pi k). \tag{A.23}$$

Fig. A.1 also shows the point at $k = 1$ (open diamond symbol) that corresponds to the result in Eq. A.12. The discrepancy at $k = 1$ generates an inconsistency in interpretation of the nearest neighbor root mean square fluctuation σ_c. On the other hand, in the discrete description, the assignment $\sigma = \Delta_d(1)$ is natural and satisfies Eq.A.2 by construction.

The scattering profile (Eq. 3.14), however, is predicted to be practically the same, since the two correlation functions shown in Fig. A.1 have the same functional form. This is confirmed in Fig. A.2 which shows the structure factor of a single domain of size $L = 3000$Å, with $D = 60$Å and $\eta_1 = 0.1$. The dashed lines show the expected power law decay of the peak tails.

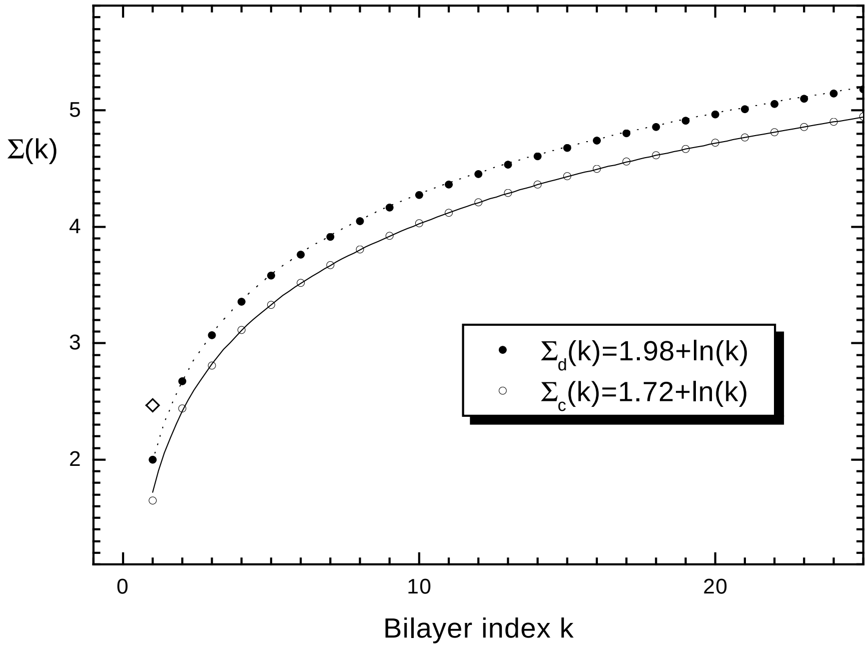

Figure A.1: Comparison of the interbilayer correlation functions Σ_d and Σ_c.

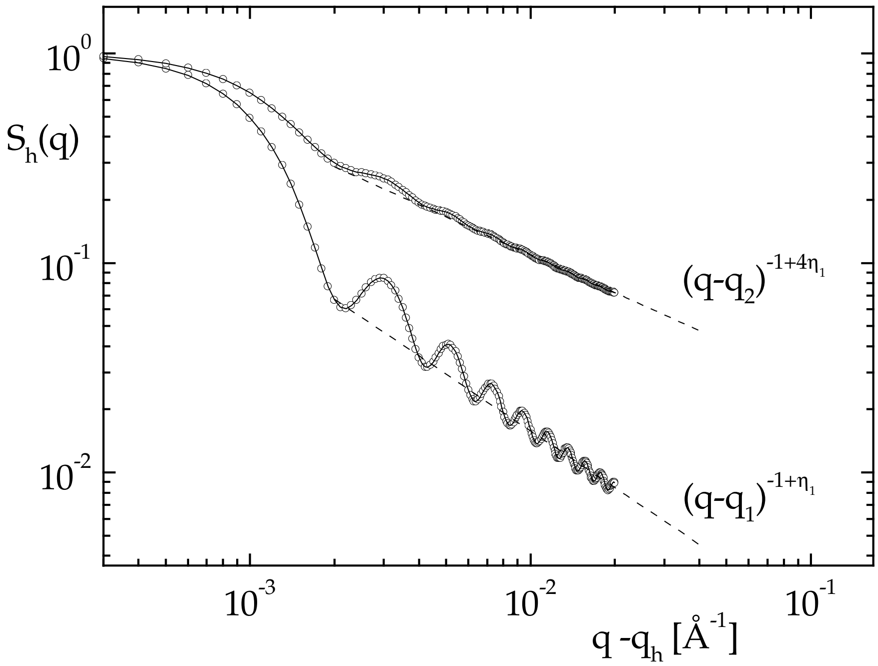

Figure A.2: Theoretical peak profile for a single scattering domain with $L = 3000$Å, $D = 60$Å, and $\eta_1 = 0.1$. Open symbols: discrete model. Solid line: continuous model. Dashed line: expected power law behavior.

Appendix B

Integration over undulation modes

For the calculation of the free energy (Eq. 2.13) and of the mean square fluctuation (Eq. 2.20), the summations over the fluctuation modes have been replaced with integrals using

$$\sum_{Q_x,Q_y} \frac{1}{L_x L_y} = \frac{1}{4\pi^2}\int dQ_x dQ_y = \frac{1}{4\pi}\int d(Q_r^2). \tag{B.1}$$

This is justified for large membranes, i.e. $L_x, L_y \gg a$, where $a \approx 7$Å is the intermolecular distance. In both cases the integrand decays as Q_r^{-4} at large Q_r and therefore polar coordinates can be used (i.e. the membrane shape is irrelevant). With the notations $t = Q_r^2$ and $c^2 = \frac{4B\sin^2 Q_z D/2}{K_c}$ the integral in Eq. 2.13 requires

$$I_1 = \int dt\ \ln\left(1+\frac{c^2}{t^2}\right) = t\ln\left(1+\frac{c^2}{t^2}\right) + 2\ c\ \mathrm{atan}(t/c), \tag{B.2}$$

and the integral in Eq. 2.20 requires

$$I_2 = \int dt\ \frac{1}{t^2+c^2} = \frac{1}{c}\ \mathrm{atan}(t/c). \tag{B.3}$$

B.1 The cutoff at low Q_r

The quantity c in Eqs. B.2 and B.3 plays the role of a cutoff for small t. The integral gives the same result as the finite summation if the following condition is satisfied

$$c \gg t_{min}. \tag{B.4}$$

For the most unfavorable case, namely for $Q_z = Q_{zmin}$, this requires

$$BD^2Q_{zmin}^2 \gg K_c Q_{rmin}^4. \tag{B.5}$$

With the notation

$$\lambda \equiv \sqrt{K_c/BD^2}, \tag{B.6}$$

we have the condition

$$L_x L_y \gg L_z \lambda. \tag{B.7}$$

For the systems considered in this work λ is of the order of $10-10^2$Å, $L_z \sim 10^3 - 10^4$Å and $L_x \sim L_y \sim 10^4$Å. Therefore condition Eq.B.7 is easily satisfied.

B.2 Integration limits

The lower limit can be set to zero when $c \gg t_{min}$. The upper limit is

$$\frac{t_{max}}{c} > \frac{t_{max}}{c_{max}} = \frac{\pi^2/a^2}{2/(\lambda D)} \sim 10^2 \tag{B.8}$$

giving $\mathrm{atan}(t_{max}/c) = \pi/2$.

B.3 Summation vs. integral

Consider the sum:

$$D(N) = \frac{1}{N}\sum_{n=1}^{N/2} \frac{1}{\sin^2\left(\frac{\pi n}{N}\right)} \tag{B.9}$$

with the approximation:

$$S(N) = \frac{1}{N}\sum_{n=1}^{N/2} \frac{1}{\left(\frac{\pi n}{N}\right)^2} \tag{B.10}$$

and the integral form:

$$I(N) = \frac{1}{\pi}\int_{\pi/N}^{\pi/2} \frac{dt}{t^2} = \frac{N-2}{\pi^2}. \tag{B.11}$$

The ratio $r(N) = I(N)/S(N)$ does not approach 1 for large N, but some value around $6/\pi^2$, that can be estimated using Euler-Maclaurin summation formulae. The exact value of $r(N)$ is not important, rather, it is the fact that the approximation with an integral gives, in this case, a 60% deviation in the final result.

Now let us introduce a cutoff c and compare:

$$D_c(N) = \frac{1}{N}\sum_{n=1}^{N/2} \frac{1}{\sin^2\left(\frac{\pi n}{N}\right) + c^2} \tag{B.12}$$

and

$$S_c(N) = \frac{1}{N} \sum_{n=1}^{N/2} \frac{1}{\left(\frac{\pi n}{N}\right)^2 + c^2} \tag{B.13}$$

with

$$I_c(N) = \frac{1}{\pi} \int_{\pi/N}^{\pi/2} \frac{dt}{t^2 + c^2} = \frac{1}{\pi c} \mathrm{atan}\left(\frac{t}{c}\right)\Big|_{\pi/N}^{\pi/2}. \tag{B.14}$$

The ratio $r_c(N) = I_c(N)/S_c(N)$ approaches 1 for

$$c \gg \frac{\pi}{N}. \tag{B.15}$$

The summation over Q_r is mathematically similar, the compression term $4B\sin^2(Q_z D/2)/K_c$ playing the role of the cutoff c. We have therefore shown that the approximation with an integral (Eq. B.1) is admissible if $c \gg \pi/N$.

Appendix C

MCT fitting program

C.1 Overview

The Modified Caillé Theory (Zhang et al., 1994) is used to fit high resolution low angle X-ray scattering data for unoriented multilamellar lipid membranes in the fluid phase. MCT fits all diffraction peaks simultaneously. Two data files may be used for each peak: we usually have a broad scan of total width ≈ 0.2 deg in 2θ, and a fine scan of total width ≈ 0.02 deg. Backgrounds can be subtracted prior to fit or modeled by analytical functions.

MCT starts by reading an initialization file, one sample per run. The output consists of three files that contain the sorted data, the fitting profile and the fit progress report. If needed, the initialization file and MCT input/output formats can be easily adjusted.

The following functions must be determined **before** using MCT :

1. Resolution function (depends on actual experimental set-up)

2. Background function (depends on actual experimental set-up)

3. Correlation function (provided in file Delta.inf)

The minimization procedure is the standard Levenberg-Marquardt algorithm executed by the subroutine LMDER of MINPAK by Garbov et. al (1980). Fitting errors are estimated from the inverse of the χ^2 curvature matrix. In the current program version the inverse matrix is calculated using the IMSL library function DLINRG. If no IMSL access, edit mct.f, search for imsl and follow the instructions.

The MCT package contains the following files:

mct.f	=	f77 source file
1922s.par	=	MCT initialization file template
cas7.19	=	sample data file (broad scan h=1)
cas7.20s	=	sample data file (fine scan h=1)
cas7.21	=	sample data file (broad scan h=2)
cas7.22s	=	sample data file (fine scan h=2)
ck1922s.dat	=	copy of output file 1922s.dat (for after run check)
ck1922s.fit	=	copy of output file 1922s.fit
ck1922s.chi	=	copy of output file 1922s.chi
Delta.inf	=	correlation function input file

C.2 MCT fitting function

C.2.1 Experimental peak profile

$$I_h(0,0,q_z) = K\ |F_h|^2 \int_0^{3s_x} dq'_x \int_{q_z-3s_G}^{q_z+3s_G} dq'_z\ R_x(q'_x) R_z(q_z - q'_z)\ \langle S_h(\sqrt{q'^2_x + q'^2_z})\rangle_L. \tag{C.1}$$

F_h is the scattering form factor and K is an overall scale (includes various normalization factors that are independent of h for a given sample).

R_z is the longitudinal resolution function and is modeled as

$$R_z(q_z) \quad = \quad e^{-q_z^2/2s_G^2} + \frac{a_L}{1 + q_z^2/s_L^2} \tag{C.2}$$

The parameters s_G, s_L and a_L are obtained by fitting to the experimental longitudinal resolution function. The out-of-plane resolution function is modeled by a Gaussian function, $R_x(q_x) = e^{-q_x^2/2s_x^2}$, with s_x determined from the out of plane angular acceptance of the sample and detector slits. The transverse in-plane resolution function $R_y(q_y)$ is treated as a delta function.

The average structure factor is obtained by integrating over the domain size distribution $P(L)$:

$$\langle S_h(q)\rangle_L = \int_{L_{min}}^{L_{max}} dL\ P(L)\ S_h(q, L) \tag{C.3}$$

with $P(L) = \exp(-L/\sigma_L)$.

Note: σ_L is only the notation used in the fitting program, the notation L_E is otherwise used.

The parameter σ_L is an MCT fitting parameter (elsewhere denoted by L_E) together with the Caillé parameter η_1, the peak positions $2\theta_h$, the overall amplitude $K|F_1^2|$ and the intensity ratios $r_h = |F_h|^2/|F_1^2|$. A Gaussian instead of an exponential was used in the original Zhang program. After much experience, it was found that the simpler exponential form worked just as well (see Chapter 3).

C.2.2 Theoretical peak profile

Structure factor for a single domain of size $L = ND$:

$$S_h(q, L) = \frac{2\pi L_r^2}{q^2}\left[N + 2\sum_{k=1}^{N} G_h(z_k)(N-k)\ \cos((q-q_h)z_k)\right] \qquad \text{with } z_k = kD. \tag{C.4}$$

Interbilayer correlation function:

$$G_h(z_k) = e^{-\frac{h^2}{2}q_1^2\Delta^2(k)} \qquad \text{with } q_1 = \frac{2\pi}{D}. \tag{C.5}$$

$\Delta^2(k)$ is the asymptotic form of the mean square fluctuations of the distance between bilayers n and $n+k$. It is obtained from the fluctuation function for a system of N bilayers with PBC in the limit $N \to \infty$.

$$\Delta^2_{PBC}(N, z_k) = \frac{2\eta_1}{q_1^2}\sum_{j=1}^{N/2}\frac{1-\cos\frac{2\pi j z_k}{ND}}{\frac{N}{\pi}\sin\frac{\pi j}{N}} \tag{C.6}$$

$$\Delta^2(z_k) = \Delta^2_{PBC}(N=\infty, z_k) = \frac{2\eta_1}{q_1^2}\Sigma(k) \tag{C.7}$$

$\Sigma(k)$ denotes the sum in Eq. C.6 in the limit $N \to \infty$. Combine Eq. C.5 and Eq. C.7 to obtain

$$G_h(z_k) = e^{-\eta_1\, h^2\, \Sigma(k)}. \tag{C.8}$$

The asymptotic form of the correlation function $G_h(z_k)$ depends on η_1 and on the bilayer index k only. The advantage of using the asymptotic form for data fitting is that the universal function $\Sigma(k)$ is calculated only once and stored in a database.

C.3 Initialization file instructions

The program will ask for the name of this file. The sample file in this package is named 1922s.par. See this sample file while studying these instructions. Also, see the more extended comments in Section C.3.2 that follow these skeletal instructions.

C.3.1 Entries

This file must have exactly the number of lines shown in the sample file.

1. Data files.

Two files per peak in increasing order of peak index. Needs exactly 8 entries.

Use dummy file if needed.

2. Output files.

Three entries in this order:

Chi-file (log file)

Data file (for compact output)

Fit file.

3. Number of data points.

Enter number of data points for each peak. Enter **0** if no peak.

Sum must not exceed M_{max} which is set to 300 in the current version of the program.

4. Resolution.

The longitudinal in-plane resolution function $R_z(2\theta)$ is interpolated using a sum of a Gaussian (G) and a Lorentzian (L) function. The transverse in-plane resolution function $R_x(q_x)$ is assumed Gaussian (see Section C.3.2).

Enter:

s_G = width of G (in degrees)

s_L = width of L (in degrees)

a_L = Amplitude of L relative to G

s_x = out of plane width (assumed Gaussian) (in degrees)

X-ray wavelength

Name of $\Sigma(k)$ database

5. Background.

Linear in this case. bgd = A_{bgd} * two-theta + B_{bgd}.

Enter A_{bgd} and B_{bgd}.

6. Starting parameters.

(free = **1**, fixed = **0**) First block of 10 lines contains **1/0** digit and parameter description. (The parameter description is not read by the program.)

P1..P4	=	peak positions $2\theta_h$
P5	=	overall amplitude (instrumental scale)
P6..P8	=	intensity ratios relative to the first peak
		See note about Lorentz correction.
P9	=	Caillé parameter η_1
P10	=	σ_L = Decay length (width) of P(L)

Second block. Enter initial (or fixed) values in corresponding order.

7. D-space from ...

Enter peak order to use to determine D.

8. P(L) mode

Enter **0** for fixed integration limits or non-zero **scale** for adjustable L_{max} =**scale***σ_L.

9. P(L) limits

Enter (integer = number of bilayers):

Smallest domain size L_{min}

Maximum domain size L_{max}

Integration step

10. Fit/Control

1 for minimization, **0** for no minimization (check initial parameters)

11. Fitting errors

Enter **0** to skip the calculation of error matrix.

C.3.2 Comments

$\boxed{1}$ and $\boxed{2}$ File name lengths are limited by the size of variables **fileh**, **filechi**, **filedat** and **filefit**.

$\boxed{3}$ The number of data points for each peak can have any value between 0 and M_{max}, but the total sum cannot exceed M_{max} which is set to 300 in current versions of the program. Also, data should be within ± 0.25 degrees in two-theta near each peak. The limit is imposed by the index **Mq** and the scale **dim** and keeps a safe margin for the convolution with the resolution function. This limit is a compromise between:
(a) MCT theory assumes a constant form factor across the peak, therefore the narrower the peak the better, and
(b) Data should not be confined around the central peak, which is defined by the resolution function, but should include "enough tail". Usually our data do not exceed ± 0.15 degrees from the peak.

$\boxed{4}$ This is crucial input for this analysis. If you don't know your instrumental resolution function or if the peaks are not fully resolved, then don't bother using this program.

The function used (t stands for **two-theta**):
$R_z(t) = A\ (G(t) + a_L\ L(t)) - d_b$,
with $G(t) = \exp(-(t - t_0)^2/(2s_G^2)$ and $L(t) = 1/[1 + (t - t_0)^2/s_L^2]$.
Three relevant parameters: s_G, s_L and a_L.
Three irrelevant parameters: A, t_0 and d_b (detector baseline).

The out-of-plane resolution function (determined by the slits acceptance) is considered Gaussian, $R_x(q_x) = \exp(-q_x^2/(2s_x^2))$. The transverse in-plane resolution $R_y(q_y)$ is considered as a delta function.

$\boxed{5}$ Our background is well modeled by a linear function. Other functions can be easily incorporated. Alternatively, the background can be subtracted from data prior to fit and then A_{bgd} and B_{bgd} can be set to zero.

$\boxed{6}$ Initialization of peak positions **P1..P4** should be made as close as possible to the actual peak. Calculation of the corresponding Jacobian part uses a shortcut (related to the convolution with the resolution function) that does not work too far from the peak. In our experiments at CHESS we found that the peak value of $2\theta_h$ did not index perfectly with h and the error was random. We documented that this was due to small mechanical hysteresis in the 2θ arm. This requires separate values of $2\theta_h$ to run this fitting program, but the corresponding error in D-spacing is negligible.

The Lorentz correction $(= h^2)$ should be included upon input, although input parameter accuracy is not so important as for $2\theta_h$. However, it is important to note that output for **P6..P8** are intensity ratios that have been Lorentz corrected and fluctuation corrected.

The $P(L)$ parameter σ_L depends on the sample preparation. It is roughly the average scattering domain size in the limit of very large L_{max}. It can be set to a couple of thousand angstroms estimated from the peak width.

$\boxed{7}$ Ideally, if there is no slit smearing, all strong peaks should give precisely the same D-spacing. The program requires one to choose which peak to use for D. This entry allows for a choice of the significant peak.

$\boxed{8}$ and $\boxed{9}$ Allow for a variation of L_{max} which is not a true fitting parameter. The relevant parameters, η_1 and the intensity ratios, should not be very sensitive to L_{max} once L_{max} is reasonable. Do a preliminary fit with large steps $(dL = 10 - 20)$ and **scale** $= 3 - 6$ to get rough estimates of the fitting parameters.

Bibliography

[1] Als-Nielsen, J., Litster, J. D., Birgeneau, R., J., Kaplan, M., Safinya, C. R., Lindegaard-Andersen, A., and Mathiesen, S., 1980. Observation of algebraic decay of positional order in a smectic liquid crystal. *Phys. Rev. B* 22, 312-320.

[2] Bechinger, B. and Seelig, J., 1991. Conformational changes of the phosphatidylcholine headgroup due to membrane dehydration. A ^{2}H-NMR study. *Chem. Phys. Lipids* 58, 1-5.

[3] Buldt, G., Gally, H. U., Seelig, J., and G. Zaccai., 1979. Neutron diffraction studies on phosphatidylcholine model membranes. I: Head group conformation. *J. Mol. Biol.* 134,673-691.

[4] Caillé, A., 1972. Physique cristalline - Remarques sur la diffusion des rayons X dans les smectiques. *A. C. R. Acad. Sc. Paris, Série B* 274, 891-893.

[5] De Gennes, P. G., 1974. The physics of liquid crystals. *Oxford Press, Clarendon.*

[6] Dittmer, J. C. and Lester, R. L., 1964. A simple, specific spray for the detection of phospholipids on thin-layer chromatograms. *J. Lipid Research* 5, 126-127.

[7] Dutta, P., Sinha, S. K., 1981. Analytic form for the static structure factor for a finite two-dimensional harmonic lattice. *Phys. Rev. Lett.* 47, 50-53.

[8] Evans, E. A. and Parsegian, V. A., 1983. Energetics of membrane deformation and adhesion in cell and vesicle aggregation. *Annals N.Y. Acad. Sci.* 416, 13-33.

[9] Evans, E. A. and Parsegian, V. A., 1986. Thermal-mechanical fluctuations enhance repulsion between biomolecular layers. *Proc. Natl. Acad. Sci.* 83, 7132-7136.

[10] Evans, E. A. and Needham, D., 1987. Physical properties of surfactant bilayer membranes: Thermal transitions, elasticity, rigidity, cohesion and colloidal interactions. *J. Phys. Chem.* 91, 4219-4228.

[11] Evans, E. A. and Rawicz, W., 1990. Entropy-driven tension and bending elasticity in condensed-fluid membranes. *Phys. Rev. Letts.* 64, 2094-2097.

[12] Faucon, J. F., Mitov, M. D., Méléard, P., Bivas, I., and Bothorel, P., 1989. Bending elasticity and thermal fluctuations of lipid membranes. Theoretical and experimental requirements. *J. Phys. France* 50, 2389

[13] Feller, S. E., Venable, R. M., and Pastor, R. W., 1997. Computer Simulation of a DPPC Phospholipid Bilayer: Structural Changes as a Function of Molecular Surface Area. *Langmuir* 13, 6555-6561.

[14] Flory, P. J., 1956. Statistical mechanics of semi-flexible chain molecules. *Proc. Roy. Soc. London* A234, 60-73.

[15] Gawrisch, K., Richter, W., Mops, A., Balgavy, P., Arnold, K. and Klose, G., 1985. The influence of water concentration on the structure of egg yolk phospholipid/water dispersions. *Studia Biophys* 108, 5-16.

[16] Gruner, S. M., Tate, M. W., Kirk, G. L., So, P. T. C., Turner, D. C., Keane, D. T., Tilcock, C. P. S., and P. R. Cullis., 1988. X-ray diffraction study of polymorphic behavior of N-methylated DOPE. *Biochemistry* 27, 2853-2866.

[17] Harbich, W. and Helfrich, W., 1990. Adhesion in egg lecithin multilayer systems produced by cooling. *J. Phys. France* 51, 1027-1048.

[18] Helfrich, W., 1978. Steric interaction of fluid membranes in multilayer systems. *Z. Naturforsch* 33a, 305-315.

[19] Holte, L. L., Peter, S. A., Sinnwell, T. M., and Gawrisch, K., 1995. ^{2}H nuclear magnetic resonance order parameter profiles suggest a change of molecular shape for phosphatidylcholines containing a polyunsaturated acyl chain. *Biophys. J.* 68, 2396-2403.

[20] Holyst, R., 1991. Landau-Peierls instability, X-ray-diffraction patterns, and surface freezing in thin smectic films. *Phys. Rev. A* 44, 3692-3709.

[21] Hristova, K. and White, S. H., 1998. Determination of the hydrocarbon core structure of fluid dioleoylphosphocholine (DOPC) bilayers by x-ray diffraction using specific bromination of the double-bonds: effect of hydration. *Biophys. J.* 74, 2419-2433.

[22] Israelachvili J. N. and Wennerstrom, H., 1990. Hydration or steric forces between amphiphilic surfaces? *Langmuir* 6, 873-876. (Commented by Parsegian, V. A. and Rand, P. 1991.)

[23] Janke, W. and Kleinert, H., 1986. Fluctuation pressure of membrane between walls. *Phys. Lett. A* 117, 353-357.

[24] Klose, G., Konig, B., Meyer, H. W., Schulze, G. and Degovics, G., 1988. Small-angle x-ray scattering and electron microscopy of crude dispersions of swelling lipids and the influence of the morphology on the repeat distance. *Chem. Phys. Lipids* 47, 225-234.

[25] Koenig, W., Strey, H. H., and Gawrisch, K., 1997. Membrane lateral compressibility determined by NMR and X-ray diffraction: effect of acyl chain polyunsaturation. *Biophys. J.* 73, 1954-1966.

[26] Kummrow, M. and Helfrich, W., 1991. Deformation of giant lipid vesicles by electric fields. *Phys. Rev. A* 44, 8356-8360.

[27] Lei, N., Safinya C. R., and Bruinsma R. F., 1995. Discrete harmonic model for stacked membranes: theory and experiment. *J. Phys. II France* 5, 1155-1163.

[28] Leibler, S. and Lipowsky, R., 1987. Complete unbiding and quasi-long-range order in lamellar phases. *Phys. Rev. B* 35, 7004-7009.

[29] Leikin, S., Parsegian V. A., and Rau D. C., 1993. Hydration forces. *Annu. Rev. Phys. Chem.* 44, 369-195.

[30] Lemmich, J., Mortensen, K., Ipsen, J. H., Honger, T., Bauer, R., and Mouritsen, O. G., 1996. Small-angle neutron scattering from multilamellar lipd bilayers: Theory, model, and experiment. *Phys. Rev. E.* 53, 5169-5180.

Comment: The decoupling between the form factor and the structure factor has been a debate issue between supporters of the Caillé theory (like ourselves) and critics, in particular Lemmich et al., who advocate a paracrystalline type model for lipid bilayers. The are against the decoupling scheme mostly because their poor resolution (they use neutron scattering) does not allow them to treat the data in this way. In this particular paper after a strong criticism of the Caillé theory, they report that, actually, their fluid phase data are equally well described by the two theories. Even so, they conclude that the paracrystalline theory is superior, based on their analysis of the lower temperature phase $P_{\beta'}$.

[31] Lewis, B. A. and Engelman, D. M., 1983. Lipid bilayer thickness varies linearly with acyl chain length in fluid phosphatidylcholine vesicles. *J. Mol. Biol.* 166, 211-217.

[32] Lipowsky, R. and Leibler, S., 1986. Unbiding transitions of interacting membranes. *Phys. Rev. Lett.* 56, 2541-2544. (Errata: Phys. Rev. Lett. 59, # 17)

[33] Lis, L. J., McAlister, M., Fuller, N. L., Rand, R. P., and V. A. Parsegian., 1982. Interactions between neutral phospholipid bilayer membranes. *Biophys. J.* 37, 657-666.

[34] Marcelja, S. and Radic, N., 1976. Repulsion of interfaces due to boundary water. *Chem. Phys. Lett.* 42, 129-130.

[35] Meleard, P., Gerbeaud, C., Pott, T., Fernandez-Puente L., Bivas I., Mitov M. D., Dufourcq J., and Bothorel, P., 1997. Bending elasticities of model membranes: in fluences od temperature and sterol content. *Biopys. J.* 72, 2616-2629.

[36] McIntosh, T. J. and Simon, S. A., 1986a. Hydration force and bilayer deformation: A reevaluation. *Biochemistry,* 25, 4058-4066.

[37] McIntosh, T. J. and Simon, S. A., 1986b. Area per molecules and distribution of water in fully hydrated dilaurylphosphatidylethanolamine bilayers. *Biochemistry* 25, 4948-4952.

[38] McIntosh, T. J., Magid, A. D. and Simon, S. A., 1987. Steric repulsion between phosphatidylcholine bilayers. *Biochemistry* 26, 7325-7332.

[39] McIntosh, T. J. and Simon, S. A., 1993. Contributions of hydration and steric (entropic) pressure to the interactions between phosphatidylcholine bilayers: Experiments with the subgel phase. *Biochemistry* 32, 8374-8384.

[40] Nagle, J. F. 1973. Theory of biomembrane phase transitions. *J. Chem. Phys.* 58, 252-264.

[41] Nagle, J. F. and Wilkinson, D. A., 1978. Lecithin bilayers. Density measuements and molecular interactions. *Biophys. J.* 23, 159-175.

[42] Nagle, J. F. and Wiener, M. C., 1988. Structure of fully hydrated dispersions. *Biochim. Biophys. Acta* 942, 1-10.

[43] Nagle, J. F. and Wiener, M. C., 1989. Relations for lipid bilayers: Connections of electron density profiles to other structural quantities. *Mol. Cryst. Liq. Cryst.* 144, 235-255.

[44] Nagle, J. F., 1993. Area/lipid of bilayers from NMR. *Biophys. J.* 64, 1476-1481.

[45] Nagle, J. F., Zhang, R., Tristram-Nagle, S., Sun, W.-J., Petrache, H. I., and Suter, R. M., 1996. X-ray structure determination of fully hydrated L_α phase dipalmitoylphosphatidylcholine bilayers. *Biophys. J.* 70, 1419-1431.

[46] Parsegian, V. A., and Ninham, B. W., 1971. Toward the correct calculation of van der Waals interactions between lyophobic colloids in an aqueous medium. *J. Coll. Int. Sci.,* 37, 332-341.

[47] Parsegian, V. A., Fuller N., and Rand, R. P., 1979. Measured work of deformation and repulsion of lecithin bilayers. *Proc. Natl. Acad. Sci.* 76, 2750-2754.

[48] Parsegian, V. A. and Rand, P., 1991. On molecular protrusion as the source of hydration forces. *Langmuir* 7, 1299-1301. (Commented by Israelachvili, J., *Langmuir* 8, 1501.)

[49] Parsegian, V. A., 1993. Reconciliation of van der Waals force measurements between phosphatidylcholine bilayers in water and between bilayer-coated mica surfaces. *Langmuir* 9, 3625-3628.

[50] Pearson, R. H. and Pascher, I., 1979. The molecular structure of lecithin dihydrate. *Nature* 281, 499-501.

[51] Perera, L., Essmann, U. and Berkowitz, M. L., 1997. The role of water in the hydration force - molecular dynamics simulations. *Progr. Colloid Polym. Sci.* 103, 107-115.

[52] Petrache, H. I., Feller, S. E. and Nagle, J. F., 1997. Determination of component volumes of lipid bilayers from simulations. *Biophys. J.* 70, 2237-2242.

[53] Podgornik, R. and Parsegian, V. A., 1992. Thermal-mechanical fluctuations of fluid membranes in confined geometries: The case of soft confinement. *Langmuir* 8, 557-562.

[54] Podgornik, R. and Parsegian, V. A., 1997. On a possible microscopic mechanism underlying the vapor pressure paradox. *Biophys. J.* 72, 942-952.

[55] Rand, P. R. and Parsegian, V. A., 1989. Hydration forces between phospholipid bilayers. *Biochim. Biophys. Acta* 988, 351-376.

[56] Roux, D. and Safinya, C. R., 1988. A synchrotron X-ray study of competing undulation and electrostatic interlayer interactions in fluid membrane lyotropic phases. *J. Phys. France* 49, 307-318.

[57] Safinya, C. R., Sirota, E. B., Roux, D., and Smith, G. S., 1989. Universality in interacting membranes: the effect of cosurfactants on the interfacial rigidity. *Phys. Rev. Lett.* 62, 1134-1137.

[58] Shipley, G. G., 1973. Recent x-ray diffraction studies of biological membranes and membrane components. From Biological Membranes (Academic Press, London) eds. D. Chapman and D. F. H. Wallach, Vol. 2, pp 1-88.

[59] Simon, S. A., Advani, S. and McIntosh, T. J., 1995. Temperature dependence of the repulsive pressure between phosphatidylcholine bilayers. *Biophys. J.* 69, 1473-1483.

[60] Small, D.M., 1986. The physical chemistry of lipids, handbook of lipid research. *Plenum Press, New York.*

[61] Smith, G. S., Safinya, C. R., Roux, D., and Clark, N. A., 1987. X-ray study of freely suspended films of a multilamellar lipid system. *Mol. Cryst. Liq. Cryst.* 144, 235-255.

[62] Sornette, D. and Ostrowsky, N., 1986. Importance of membrane fluidity on bilayer interactions. *J. Chem. Phys.* 84, 4062-4067.

[63] Sun, W.-J., Suter, R. M., Knewtson, M. A., Worthington, C. R., Tristram-Nagle, S., Zhang R., and Nagle, J., F., 1994. Order and disorder in fully hydrated unoriented bilayers of gel phase dipalmitoylphosphatidylcholine. *Phys. Rev. E* 49, 4665-4676.

[64] Sun, W.-J., Tristram-Nagle, S., Suter, R. M., and Nagle, J. F., 1996. Structure of gel phase saturated lecithin bilayers: Temperature and chain length dependence. *Biophys. J.* 71, 885-891.

[65] Strey, H. H., Parsegian, V. A., and Podgornik, R., 1997. Equation of state for DNA liquid crystals: Fluctuation enhanced electrostatic repulsion. *Phys. Rev. Lett.* 78, 895-898.

[66] Tristram-Nagle, S., Zhang, R., Suter, R. M., Worthington, C. R., Sun, W.-J., and Nagle, J. F., 1993. Measurement of chain tilt angle in fully hydrated bilayers of gel phase lecithins. *Biophys. J.* 64, 1097-1109.

[67] Tristram-Nagle, S., Petrache, H. I., Suter, R. M., and Nagle, J. F., 1998a. Effect of substrate roughness on D spacing supports theoretical resolution of vapor pressure paradox. *Biophys. J.* 74, 1421-1427.

[68] Tristram-Nagle, S., Petrache, H. I. and Nagle, J. F., 1998b. Structure and interactions of fully hydrated dioleoylphospatidylcholine bilayers. *Biophys. J.* in press.

[69] Tieleman, D. P., Marrink, S. J. and Berendsen, H. J. C., 1997. A computer perspective of membranes: Molecular dynamics studies of lipid bilayer systems. *Biochim. Biophys. Acta* 1331, 235-270.

[70] Tobias, D. J., Tu, K. and Klein, M. L., 1997. Atomic-scale molecular dynamics simulations of lipid membranes. *Current Opinion in Colloid and Interface Science* 2, 15-26.

[71] Torbet, J. and Wilkins, W. H. F., 1976. X-ray diffraction studies of lecithin bilayers. *J. Theor. Biol.* 62, 447-458.

[72] Tu, K., Tobias, D. J., and Klein, M. L., 1995. Constant pressure and temperature molecular dynamics simulation of a fully hydrated liquid crystal phase dipalmitoylphosphatidylcholine bilayer. *Biophys. J.* 69, 2558-2562.

[73] Ulrich, A.S., Sami, M., and Watts, A., 1994. Hydration of DOPC bilayers by differential scanning calorimetry. *Biochim. Biophys. Acta* 1191, 225-230.

[74] Voet, D. and Voet, J. G., 1990. Biochemistry. *John Wiley & Sons Inc., New-York.*

[75] Wack, D. C. and Webb, W. W., 1989. Measurement by X-ray diffraction methods of the layer compressional elastic constant B in the lyotropic smectic-A (L_α) phase of lecithin-water system. *Phys. Rev. A* 40, 1627-1636.

[76] Wiener, M. C., Tristram-Nagle, S., Wilkinson, D. A., Campbell, L. E., and Nagle, J. F., 1988. Specific volumes of lipids in fully hydrated bilayer dispersions. *Biochim. Biophys. Acta* 938, 135-142.

[77] Wiener, M. C., Suter, R. M., and Nagle, J. F., 1989. Structure of fully hydrated gel phase of dipalmitoylphosphatidylcholine. *Biophys. J.* 55, 315-325.

[78] Wiener, M. C. and White, S. H., 1992. Structure of a fluid dioleoylphosphatidylcholine bilayer determined by joint refinement of x-ray and netron diffraction data. II. Distribution and packing of terminal methyl groups in a fluid lipid biayer. *Biophys. J.* 61, 428-433.

[79] White, S. H., Jacobs, R. E. and King, G. I., 1987. Partial specific volumes of lipid and water in mixtures of egg lecithin and water. *Biophys. J.* 52, 663-665.

[80] Worthington, C. R., 1969. The interpretation of low-angle X-ray data from planar and concentric multilayered structures. *Biophys. J.* 9, 222-234.

[81] Worthington, C. R., King, G. I., and McIntosh, T. J., 1973. Direct structure determination of multilayered membrane-type systems which contain fluid layers. *Biophys. J.* 13, 480-494.

[82] Zhang, R., Suter, R. M., and Nagle, J. F., 1994. Theory of the structure factor of lipid bilayers. *Phys. Rev. E* 50, 5047-5060.

[83] Zhang, R., 1995. Lecithin bilayers in fluid phase: effect of fluctuations on X-ray determination of structure. *Ph. D. Thesis*, Carnegie Mellon University.

[84] Zhang, R., Tristram-Nagle, S., Sun, W.-J., Headrick, R. L., Irving, T. C., Suter, R. M., and Nagle, J. F., 1996. Small-angle X-ray scattering from lipid bilayers is well described by modified Caillé theory but not by paracrystalline theory. *Biophys. J.* 70, 349-357.